ENERGY LANDSCAPE AND ELECTRIC FIELD MEDIATED INTERFACIAL COLLOIDAL ASSEMBLY

A Dissertation

by

PRADIPKUMAR BAHUKUDUMBI

Submitted to the Office of Graduate Studies of
Texas A&M University
in partial fulfillment of the requirements for the degree of

DOCTOR OF PHILOSOPHY

May 2006

Major Subject: Mechanical Engineering

ENERGY LANDSCAPE AND ELECTRIC FIELD MEDIATED INTERFACIAL COLLOIDAL ASSEMBLY

A Dissertation

by

PRADIPKUMAR BAHUKUDUMBI

Submitted to the Office of Graduate Studies of
Texas A&M University
in partial fulfillment of the requirements for the degree of

DOCTOR OF PHILOSOPHY

Approved by:

Co-Chairs of Committee,	Ali Beskok
	Malcolm Andrews
Committee Members,	Michael A. Bevan
	Zhengdong Cheng
Head of Department,	Dennis O'Neal

May 2007

Major Subject: Mechanical Engineering

ABSTRACT

Energy Landscape and Electric Field Mediated

Interfacial Colloidal Assembly. (May 2007)

Pradipkumar Bahukudumbi, B.E., University of Madras;

M.S., Texas A&M University

Co-Chairs of Advisory Committee: Dr. Ali Beskok
Dr. Malcolm Andrews

Chemically and physically patterned surfaces can be used as templates to guide nano- and micro- scale particle assembly, but the design is often limited by an inability to sufficiently characterize how pattern features influence local particle-surface interactions on the order of thermal energy, *kT*. The research outlined in this dissertation describes comprehensive optical microscopy (i.e. evanescent wave, video) measurements and analyses of many-body and multi-dimensional interactions, dynamics and structure in inhomogeneous colloidal fluid systems. In particular, I demonstrate how non-intrusive observation of an ensemble of particles diffusing past each other and over a physically patterned surface topography can be used to obtain sensitive images of energy landscape features. I also link diffusing colloidal probe dynamics to energy landscape features, which is important for understanding the temporal imaging process and self-assembly kinetics. A complementary effort in this dissertation investigated the use of external AC electric fields to reversibly tune colloidal interactions to produce metastable ordered configurations. In addition, the electrical impedance spectra

associated with colloidal assemblies formed between interfacial microelectrode gaps was measured and consistently modelled using representative equivalent circuits.

Significant results from this dissertation include the synergistic use of the very same colloids as both imaging probes and building blocks in feedback controlled self-assembly on patterns. Cycling the AC field frequencies was found to be an effective way to anneal equilibrium colloidal configurations. Quantitative predictions of dominant transport mechanisms as a function of AC electric field amplitude and frequency were able to consistently explain the steady-state colloidal microstructures formed within electrode gaps observed using video microscopy. A functional electrical switch using gold nanoparticles was realized by reversibly forming and breaking colloidal wires between electrode gaps. Extension of the concepts developed in this dissertation suggest a general strategy to engineer the assembly of colloidal particles into ordered materials and controllable devices that provide the basis for numerous emerging technologies (e.g. photonic crystals, nanowires, reconfigurable antennas, biomimetic materials).

To my parents and grandparents

ACKNOWLEDGMENTS

There are several people who significantly influenced this dissertation – in ways direct and indirect – and I would like to thank them here. My advisor, Ali Beskok provided me the academic freedom to pursue research problems that truly interested me, and for that I am very grateful. His enthusiasm, genuine interest in my progress and good humor have been largely responsible for making my life as a Ph. D student exciting and stress-free. Mike Bevan's colloids class served as direct inspiration for the research work described in this dissertation. I would like to thank him for allowing me to be a part of his research group. The scientific content of this dissertation would have been significantly reduced were it not for his constant input of ideas during our individual meetings and attention to detail.

I thank Malcolm Andrews for providing valuable counsel and feedback on the microencapsulation project and for educating me on organizational skills and work ethics. David Ford introduced me to statistical mechanics and molecular modeling through his classes and has always been accessible to answer questions related to my research. I would also like to thank him for providing me with an opportunity to work on a molecular modeling project related to membrane separation and for his help in preparing the manuscript. Greg Huff helped me understand the basics of reconfigurable antennas and impedance measurements. Thanks also to Zhengdong Cheng for taking time to serve on my dissertation committee.

I have been lucky to work with an incredible group of students in the Bevan Lab, and it has been a joy to socialize, talk with and learn from Sam, Wu, Greg, Neil, Richard and Shannon. I have benefited greatly from numerous discussions/arguments with Sam on hydrodynamics and statistical mechanics. I am clearly indebted to Neil for all his help with microfabrication and AFM, and to Wu for his help with Fortran codes and image analysis. Thanks are also due to: Greg, for his help with experiments, many competitive games of racquetball, and for introducing me to anime among other things; Richard, for his engaging commentaries on the housing bubble, religion and the investment holy grail; Shannon for her entertaining early-morning rants. Thank you all for putting up with me and making the lab a fun place to work.

Many people in the secretarial and support staff in mechanical and chemical engineering – among them Gina Haddick, Teresa Philips, Nellie Dickens, Charlotte Simms, Missy Cornett, Missy Newton, Towanna Hubacek, Sarah Allen and Valerie Green – have helped me on numerous occasions with travel reimbursements, reservations, departmental letters and computer accounts, making life around here a lot easier.

I am grateful for financial support I received for my graduate studies from the Texas Institute for Intelligent Bio-Nano Materials and Structures for Aerospace Vehicles, funded by NASA Cooperative Agreement No. NCC-1-02038 and DARPA (W911NF-06-1-0050, FA9550-07-C-0002).

Finally, I would like to thank my mom, dad and brother for being a constant source of support and comfort in times of need. My parents encouraged me to develop

my scientific interests from an early age and continue to inspire me to achieve greater success. If not for my mom’s constant reminders to graduate, this dissertation would still be incomplete.

TABLE OF CONTENTS

Page

Page

Page

LIST OF FIGURES

FIGURE Page

FIGURE Page

FIGURE Page

FIGURE Page

FIGURE Page

FIGURE Page

LIST OF TABLES

1. INTRODUCTION

1.1. Background

Templated colloidal self-assembly[1] refers to processes in which colloids autonomously and reversibly organize themselves on energetic surface patterns[2]. While many processes are often claimed as "templated colloidal self-assembly", it is the rare exception when colloids are actually assembled on any surface without the assistance of external control involving manipulation with fields such as shear, electric, magnetic, optical, etc. Although macroscopic intuition, and frustration with random Brownian motion, provides the understandable motivation for implementing processes that involve assembly by human intervention extended into the microscopic world via external fields, nanoscale self-assembly requires a paradigm shift to embrace Brownian motion, not only

---

This dissertation follows the style of The Journal of Chemical Physics.

as a source of disorder, but also as the natural motion essential to dynamic self-assembly processes in systems described by statistical mechanics (interplay of potential energy and entropy - free energy).

Beyond the limited number of studies investigating colloidal assembly processes without external intervention, reports of truly thermodynamically reversible colloidal self-assembly are even less common. Reversible colloidal self-assembly requires that initially disorganized collections of colloids can be repeatedly assembled into organized structures and completely disassembled ad infinitum by simply tuning a thermodynamic variable (changing a macroscopic intensive variable without appreciable gradients on the length scale of the thermodynamic system, e.g. temperature). For example, the most common type of templated colloid assembly employs strong attractive interactions (e.g. convective forces due to evaporation, oppositely charged surfaces) to cause irreversible deposition of colloids on surfaces [3,4], but such an approach is clearly not reversible and generally gives rise to disordered aggregates or gels rather than organized structures such as crystals. Because uncontrolled drying of monodisperse colloids easily produces polycrystalline structures, many studies have attempted to maximize crystalline domain size using controlled drying approaches[5,6]. Despite initial promising results, colloidal crystals prepared with drying techniques are too disordered for practical use.

In general, approaches to interfacial colloidal assembly can be categorized as (1) equilibrium "self assembly" processes where particle configurations are a direct consequence of interparticle forces only, (2) non-equilibrium "driven assembly" processes where metastable structures exist solely due to external forces, or (3) a

combination of these two cases. Equilibrium methods to create thermodynamic colloidal assembly include manipulating colloidal forces,[7] interactions with templates,[1,3,8-10] or thermodynamic gradients.[11] Examples of non-equilibrium methods to generate metastable ordered colloidal structures include applying electric,[12,13] magnetic,[14] optical,[15-17] and flow[18,19] fields, or manipulating sample orientation relative to gravity[20]. Although the concept of using strong attraction to place a building block in a specified location follows again from macroscopic intuition (i.e. how we assemble macroscopic objects or functional devices), such an approach is inherently unsuccessful at the microscale because it dominates/suppresses the weak interactions that are essential to autonomous and reversible self-assembly processes.

Using these approaches independently is ineffective as reliable colloidal assembly schemes because equilibrium methods tend to form dynamically arrested structures, and non-equilibrium methods produce inherently metastable configurations. To design robust processes for interfacial colloidal assembly, the complex interplay of thermodynamic and kinetic factors must be explicitly considered and optimized in a single process; an intelligently designed process must specify *both a thermodynamically favored structure and a suitable kinetic pathway*. The primary limitation to implementing such reversible assembly processes is a lack of basic knowledge connecting colloid interactions to the thermodynamics and kinetics of interfacial colloidal assembly.

One of the major fundamental difficulties with understanding colloidal self-assembly on energy landscapes (templates) is the ability to know all relevant interactions

between colloids and surface regions and to understand how their precise balance produces a given equilibrium colloidal configuration/structure on a patterned surface. Although statistical mechanics has been applied with success to understand equilibrium phase behavior and structures of some of the most basic, model, bulk, homogeneous, single component materials (such as argon) as well as more complex molecules besides noble gases (such as water for instance), the application of these methods to inhomogeneous colloidal fluids and phase transitions of such fluids next to patterned surfaces is still in its infancy.

To avoid misinterpretation, it is important to clarify the meaning and significance of certain keywords used repeatedly throughout this dissertation. As a matter of terminology, colloidal particles above patterned substrates that modulate equilibrium density distributions are referred to as inhomogeneous colloidal fluids. A physically varying topography patterned on a glass substrate is referred to as an energy landscape. This jargon is intended to convey a literal gravitational potential energy surface, very much like the potential energy changes associated with climbing over a hilly terrain on the earth's surface. However, in contrast to sampling the earth's energy landscape by doing work (e.g. using engine, muscles), the colloids make excursions (and configurational changes) to sample positions on the potential energy landscape as the result of thermal energy fluctuations.

Here, we also note the relevance and differences of our measurements of colloidal fluids on very real and literal potential and free energy landscapes with the energy landscapes used in the glasses and protein folding literature. Energy landscapes

in general are a theoretical construct used to understand glass formation and protein folding, where configurations having different free energies navigate between intermediate configurations by overcoming free energy barriers. The timescale associated with overcoming these energy barriers determines the self-diffusion processes. Simple liquids at high temperatures have no free energy barriers and so different configurations can form quite easily and rapidly. If a liquid configuration gets trapped in a local minimum with high free energy barriers all around it, the configuration is said to be a glass (kinetically arrested) because it cannot surmount the free energy barriers and rearrange on experimental timescales (a folding protein can also get stuck in such a trapped configuration; as another trivial example, a perfect bi-crystal cannot be converted into a perfect single crystal without first melting it). So energy landscapes, although abstract, determine the free energy barriers between different configurations, their lifetimes, and colloid self diffusion coefficients.

1.2. Objectives and Significance

This dissertation aims to contribute to the understanding of how to design, control, and optimize both thermodynamic and kinetic aspects of 2D interfacial colloidal assembly on homogeneous, patterned and electrode surfaces. The overall approach is to use advanced optical microscopy techniques (i.e. total internal reflection (TIRM)[21] and video (VM)[22] microscopies) to measure interactions, dynamics, and structure in interfacial colloidal processes, and then use appropriate theoretical tools (i.e. Monte Carlo (MC) [23,24]) to interpret and predict such observations. The goal is to understand interfacial colloidal assembly on energy landscapes as a fundamental phenomenon

important to complex fluid technologies and emerging advanced material applications. Central questions related to attaining these objectives are:

- How do particle-particle, particle-surface, and particle-field interactions on the order of kT control equilibrium colloidal assembly[7] on homogeneous and patterned surfaces?
- How can equilibrium properties and dynamics of 2D inhomogeneous colloidal fluids be connected to patterned surface topographies via measured free energy and potential energy landscapes?
- How can colloidal particle configurations and dynamics be manipulated with electric fields to navigate free energy landscapes to avoid kinetically trapped microstructures?[25-27]

The strategy adopted in this dissertation to address these issues consists of a systematic series of experiments to understand how energy landscapes and external electric fields independently, and in combination, influence equilibrium colloidal assembly and the kinetic pathways in 2D crystallization. The overarching objective of this research, therefore, is to extend and develop methods that exploit the use of diffusing colloidal probes to directly measure colloidal interactions in order to understand and control both equilibrium and non-equilibrium colloidal assembly processes on substrates. The specific objectives of this research work are summarized below:

- Quantitatively analyze concentrated diffusing colloidal probes on energy

landscape features as a basis to predict how colloidal particles self-assemble on patterned surfaces as well as a new paradigm/modality for imaging surfaces. The latter concept is also related to understanding both equilibrium and dynamic aspects of how colloids sample energy landscapes, which is a simplified, illustrative model problem related to configurational/conformational rearrangements of generic importance to statistical mechanics with applications such as glass transitions and protein-folding.

- Employ external electric fields to reversibly tune interactions between colloidal particles and facilitate assembly of ordered metastable structures.
- Manipulate colloidal assemblies between interfacial microelectrode gaps using electrokinetic transport mechanisms and simultaneously measure the associated electrical impedance spectra. Consistently model the electrical properties using representative equivalent circuits that can be directly integrated into reconfigurable devices in the future to reversibly tune interfacial AC electromagnetic properties.
- Engineer devices and multifunctional materials using ordered colloidal structures (e.g. nanowires) and encapsulated microspheres as functional components.

The significance of the dissertation work derives from the prevalence of colloidal sized components (1 nm – 10 μm) in numerous industrial complex fluids including emulsions, ceramics,[28,29] pastes,[30] coatings,[31] composites,[32] foods, minerals, and

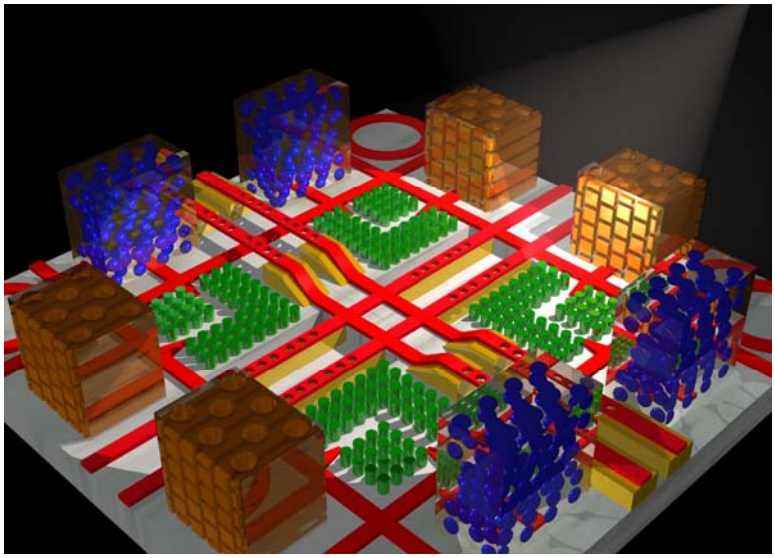

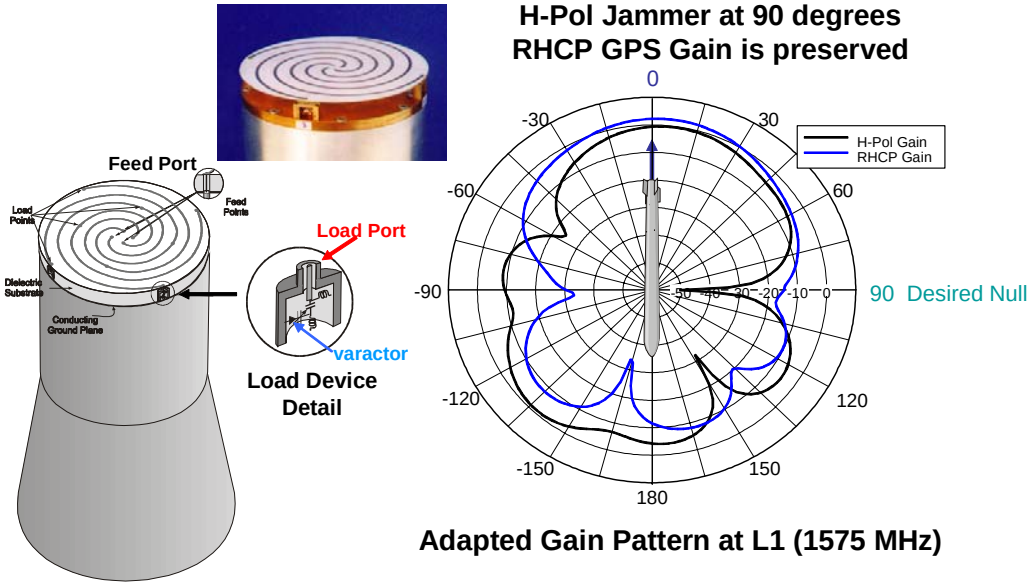

Figure 1.1. (top) Computer rendering of an all-optical integrated circuit based computer using photonic band gap materials engineered using colloidal particles. (bottom) Solids-state/MEMS based jamming device being redesigned with colloidal microfluidic networks to realize new range of dynamically reconfigurable surface electromagnetic properties and response to radio frequency signals.

pharmaceuticals,[33] but also as essential building blocks in emerging technologies based on nanostructured materials such as protein crystals,[34] magnetic storage devices,[14] chemical & biological sensors,[35] optical switches,[36] and photonics.[5] To demonstrate the importance of developing fundamental measurements and models to solve problems involving manipulating colloidal structure, we provide examples of a material (photonic crystal) and device (reconfigurable antennas) of the future in Fig. 1.1. The importance of photonic band gap (PBG) materials can be understood via their analogy to electronic band gap materials (semiconductors) used in computers that trap electrons in low and high energy states to generate 0s and 1s in the binary computer language. The PBG materials[37] are intended to accomplish the same thing with photons to create computers based on optical integrated circuits, which has numerous potential advantages over this generation computers (higher speed, lower power requirement and higher information density). In the other example, electronically reconfigurable antennas (ERA) that employ embedded microwave circuits containing devices with controllable impedance characteristics to adaptively tune (radio frequencies) surface properties have been reported in the literature (Fig. 1.1). An ERA can provide new capabilities for military and commercial vehicles, such as enhanced communication links, while reducing observable signatures and power requirements.

While these two examples may seem unrelated, we identify a common ground in this dissertation by using assembled colloidal structures as functional units in both applications. For instance, a basic requirement of PBG materials is a periodic structure on length scales comparable to the wavelength of light, which can be realized by

assembling micron-sized colloidal particles into three-dimensional crystals. On the other hand, integrated microfluidic/microelectronic networks containing metallic particles that provide the ability to tune local interfacial AC electromagnetic properties (via the formation of colloidal nanowires for example) can be used to produce unique ERA device responses that cannot currently be realized via static, solid-state materials (due to limited reconfigurability) or MEMS systems (due to scalability).

1.3. Dissertation Outline

This dissertation is organized as follows: Section 2 briefly reviews the characteristic interaction potentials in systems containing spherical colloidal particles immersed in an aqueous solution. In addition, the theoretical aspects concerning optical microscopy techniques used to measure colloidal interactions and Monte Carlo simulations are discussed. Section 3 provides details of the colloidal systems and optical microscopy experiments including protocols for fabricating physical and chemical patterns on glass substrates. Sections 4-7 contain the results from this research work. Detailed video microscopy measurements and an inverse Monte Carlo analysis of diffusing colloidal probes as a means to image three dimensional free energy and potential energy landscapes due to patterned surfaces are described in Section 4. The use of external electric fields to sensitively tune interactions between colloidal particles to form ordered structures is demonstrated in Section 5. Section 6 reports *in situ* measurements of the reversible, directed assembly of metallic nanoparticle microstructures and their associated impedance properties on surfaces between interfacial gold film microelectrodes. Bovine-Serum-Albumin (BSA) based

encapsulated colloidal particles are synthesized in Section 7 with the intention of being manipulated using external fields to engineer self-healing materials in the future. A summary of the findings of this dissertation is provided in Section 8. Finally, current and future work not presented as part of this dissertation is summarized in Section 9.

2. THEORY

2.1 Synopsis

In the following, we briefly review the characteristic interactions active in systems containing spherical colloidal particles immersed in an aqueous solution. The primary points to be made are the ability of theory to predict at least semi-quantitatively these interaction forces, and the rapidly growing ability to measure them directly via the surface forces apparatus, atomic force microscopy, optical tweezers, and other microscopy techniques. Here, we focus exclusively on the theoretical aspects concerning optical microscopy techniques used in this dissertation to sensitively measure colloidal interactions on the order of kT. This includes Ensemble Total Internal Microscopy (ETIRM) used to measure particle-wall interactions, and a technique using concentrated Diffusing Colloidal Probes (DCP) to quantitatively image patterned energy landscapes (see Section 4).

2.2 Colloidal and Surface Forces

To gain fundamental insights into the stability of colloidal dispersions and their equilibrium microstructures, it is important to understand the forces acting upon and among particles, which include viscous forces that originate in response to particle motion, Brownian forces due to the thermal energy of molecules in the solvent, and physico-chemical forces controlled by the chemical composition of the solvent, solutes, and the particles[20]. In a colloidal dispersion pair-wise additive potentials or potentials of

mean force are used to account for the effect of both the solvent and any solutes on the interactions between particles. Hydrodynamic and Brownian forces are dissipative in nature, and do not appear in the interaction potential as a consequence of the fluctuation dissipation theorem. Here, we simply consider the dispersion to be a pseudo-one component system that is fully characterized by the interaction potential *u(r, h)*, the number density, and the temperature. A wide variety of forces contribute to *u(r, h)* and their magnitudes can be sensitively tuned by adjusting the physical chemistry of the dispersion.

It is useful to distinguish the colloidal particle-wall interactions from the particle-particle interactions. The total potential energy profile for a single colloidal particle levitated above a charged wall can be calculated by summing the surface and body forces acting on the particle. For experiments presented in this dissertation, important interactions include electrostatic, van der Waals, and gravitational forces. The net separation dependent potential energy profile is given by the superposition of these relevant interactions as,

$$u(h) = u_{edl}(h) + u_{grav}(h) + u_{vdw}(h) \tag{2.1}$$

where h is the separations between particle surfaces and the substrate surface, $u_{edl}(h)$ is the interaction between overlapping electrostatic double layers on the particle and wall, $u_{grav}(h)$ is the gravitational potential energy due to the buoyant weight of the particle, and $u_{vdw}(h)$ is the continuum van der Waals attraction between the particle and wall mediated by the aqueous electrolyte medium.

For an ensemble of colloidal particles next to a planar surface confined by gravity, the effective inter-particle potential is calculated by summing the surface forces and can be represented as:

$$u(r) = u_{edl}(r) + u_{vdw}(r) \tag{2.2}$$

where r is the separation between two colloidal particle centers. Now we will briefly review the three most common colloidal interactions, electrostatic repulsion, van der Waals (vdW) or dispersion attraction, and depletant-induced interaction, in the following sub-sections.

2.2.1 Electrostatic interactions

In aqueous solutions, ionic functional groups on surfaces can dissociate or partition into the solution, thereby generating a net charge on the surface and an effective electric field in the solution. The Debye length κ^{-1}, which varies from 0.3 nm in a 1 M salt solution to 30 nm in 0.1 mM, represents the length scale over which the surface potential decays to zero. In other words, the Debye length represents the screening length over which the ions attracted to a charged surface from the bulk neutralize the surface charge[20]. For thin electrical double layers where the Debye length is smaller than particle-wall surface separations (κh>1) and much smaller than the sphere radius (κa>1), the electrostatic interactions between particles and wall surfaces, $u_{edl}(h)$, is accurately described using non-linear superposition and the Derjaguin approximation. For the specific case of 1:1 electrolyte, the interaction is given as,[21]

$$u_{edl}(h) = B_{pw} \exp(-\kappa h) \tag{2.3}$$

$$B_{pw} = 64\pi\varepsilon a \left(\frac{kT}{e}\right)^2 \tanh\left(\frac{e\Psi_p}{4kT}\right) \tanh\left(\frac{e\Psi_w}{4kT}\right) \tag{2.4}$$

$$\kappa = \left(\frac{2CN_A e^2}{\varepsilon kT}\right)^{0.5} \tag{2.5}$$

where a is particle radius, ε is the dielectric permittivity of water, k is Boltzmann's constant, T is absolute temperature, e is the elemental charge, ψ_p and ψ_w are the Stern potentials of the particle and the wall, κ^{-1} is the Debye length, C is the bulk electrolyte concentration, and N_A is Avagadro's number. Eq. (2.4) is based on the interactions between a particle with radius a and an infinite wall. According to the Derjaguin geometric correction, the electrostatic interactions between identical particles is half the interaction between particles and infinite plates and is given by:

$$u_{edl}(r - 2a) = B_{pp} \exp(-\kappa(r - 2a)) \tag{2.6}$$

$$B_{pp} = 32\pi\varepsilon a \left(\frac{kT}{e}\right)^2 \tanh\left(\frac{e\Psi_p}{4kT}\right) \tanh\left(\frac{e\Psi_w}{4kT}\right) \tag{2.7}$$

where r is the center-to-center vector between particles. The repulsive potential near particle contact is generally large relative to the thermal energy kT. In experiments described in this dissertation carried out at moderate to low ionic strengths, electrostatic repulsions are generally sufficient to stabilize the colloidal particles against dispersion attractions.

2.2.2 Gravitational interactions

The gravitational potential energy is the buoyant particle weight, *G*, multiplied by its height, *h*, above the wall. The buoyant particle weight is the product of gravitational acceleration, *g*, and the buoyant particle mass, *m*, which depends on particle volume and density difference between the particle and the fluid. The gravitational potential energy is given by,

$$u_{grav}(h) = Gh = mgh = (4/3)\pi a^3(\rho_p - \rho_f)gh \tag{2.8}$$

where ρ_p and ρ_f are the particle and fluid densities, and g is the acceleration due to gravity.

2.2.3 van der Waals interactions

Attractive van der Waals (vdW) potentials arises from electromagnetic fluctuations due to a mismatch in the particle and medium dielectric properties, and can be determined by first computing the Hamaker "function", $A_{132}(l)$, between two half-spaces, composed of materials #1 and #2, separated by distance l of medium #3 as,[38,39]

$$A_{132}(l) = -\frac{3}{2}kT\sum_{n=0}^{\infty}{}'\int_{r_n}^{\infty} x\left\{\ln\left[1-\Delta_{13}\Delta_{23}e^{-x}\right]+\ln\left[1-\bar{\Delta}_{13}\bar{\Delta}_{23}e^{-x}\right]\right\}dx \tag{2.9}$$

$$\Delta_{jk} = \frac{\varepsilon_j s_k - \varepsilon_k s_j}{\varepsilon_j s_k + \varepsilon_k s_j} \qquad \bar{\Delta}_{jk} = \frac{s_k - s_j}{s_k + s_j} \qquad s_k^2 = x^2 + \left(\frac{2\xi_n l}{c}\right)^2(\varepsilon_k - \varepsilon_2)$$

$$r_n = \frac{2l\xi_n\sqrt{\varepsilon_2}}{c} \qquad \varepsilon_k = \varepsilon_k(i\xi_n) \qquad \xi_n = \frac{nk_BT}{\hbar}$$

where $i=(-1)^{0.5}$, $\hbar$ is Planck's constant divided by 2π, c is the speed of light *in vacuum*, k is Boltzmann's constant, T is absolute temperature, and $\varepsilon_k(\omega)$ is the dielectric spectrum of material k. The prime (') next to the summation indicates that the first term (n=0) is multiplied by $\frac{1}{2}(1+2\kappa l)\exp(-2\kappa l)$ where κ^{-1} is the Debye screening length. The Hamaker function is computed as an infinite summation over regularly spaced frequencies and accurately captures the effect of the intervening medium on the electromagnetic interaction between the colloidal particles. The dielectric spectra for water and silica was reported by Bevan and Prieve[40] and the dielectric spectra of gold was reported by Parsegian and Weiss[41]. The van der Waals interaction between a sphere and a half space is accurately described using Derjaguin approximation as,[40,42]

$$u_{vdw}(h) = -\frac{a}{6}\int_{h}^{\infty}\frac{A_{132}(l)}{l^2}dl \tag{2.10}$$

The vdW attraction increases smoothly from the rapidly decaying far-field limit to values that are large relative to kT at small separations. For convenience, the particle-particle and particle-wall vdW interactions in this dissertation are represented by non-integer power-law decay fits to the continuum Lifshitz theory given by[40]

$$\begin{aligned} u_{vdw}^{pp}(r) &= -aA(r-2a)^{-p} \\ u_{vdw}^{pw}(h) &= -2aA(h-a)^{-p} \end{aligned} \tag{2.11}$$

where a is the particle radius and A and p are fitting parameters. The vdW attraction between silica colloids and chemical patterns (gold tiles patterned on a glass substrate) was calculated using Eq. (2.12) in Sections 4 and 9.

2.2.4 Depletion potentials between colloids & surfaces

The attractive depletion potential between colloids and surfaces in the presence of unadsorbing macromolecules, nanoparticles or micelles can be computed by using the Asakura-Oosawa (AO) model.[43] For all geometries, the AO potential is a function of the volume from which unadsorbed species are excluded, V_{ex}, and the osmotic pressure, Π, of the depletant as,[20]

$$u(r) = V_{ex}(r)\Pi \tag{2.13}$$

It can be easily demonstrated that the mean force is identically equal to the osmotic pressure exerted by the depletant on a surface enclosing the particle plus the depletion region. When the depleted regions around the colloidal particles overlap, the depletant is excluded from the gap and the osmotic pressure generates a net attraction proportional to the projected area of overlap between the spherical volumes enclosing the two particles[20]. For the particle-particle geometry, the AO depletion potential can be expressed as,[44]

$$u_{AO}^{pp}(r) = -\frac{4\pi}{3}\left(a_{ij}+L\right)^3\left(1-\frac{3r}{4\left(a_{ij}+L\right)}+\frac{r^3}{16\left(a_{ij}+L\right)^3}\right)\Pi \tag{2.14}$$

where L is the radius of the depletant, and a_{ij} is the arithmetic mean of the interacting particle radii. For the particle-surface geometry, the AO depletion potential can be expressed as,[45]

$$u_{AO}^{ps}(h) = -\pi\left[4L^2\left(\frac{L}{3}+a\right)-4Lah+\left(a-L\right)h^2+\frac{h^3}{3}\right]\Pi \tag{2.15}$$

Depletion interactions using micellar depletants were used in this dissertation to assemble attractive colloidal crystals. The range of interaction and the depth of the potential energy well in the experimental systems were calculated using Eq. (2.16) and (2.17) as a function of particle size and depletant concentration.

2.3 Total Internal Reflection Microscopy (TIRM)

Ensemble Total Internal Reflection Microscopy (ETIRM)[46] is a method for measuring the potential energy of interaction between many single colloidal particles and a planar charged surface. This technique was originally developed by Prieve, Lau and Lanni[47] for measuring single-particle interactions and has seen continued development over the last decade (see review article by Prieve[21] for a history of development of this technique). ETIRM uses integrated evanescent wave scattering and video microscopy techniques to monitor the three-dimensional trajectories of colloids near planar surfaces. Such measurements can be analyzed to yield many single-colloid surface potential energy profiles as well as an ensemble average colloid-surface potential energy profile by averaging over all colloids and surface regions sampled by the laterally diffusing colloids.

Evanescent waves generated by total internal reflections are scattered by colloidal particles levitated above a surface. In the ETIRM experiment, the scattering intensity of a single levitated colloid in an evanescent wave can be used to determine the instantaneous particle-wall separation, h, above a wall using the following expression,[21,48]

$$I(h) = I_0 \exp(-\alpha h) \tag{2.18}$$

where I is the scattered intensity, I_0 is the intensity at particle-wall contact or zero separation, $h=0$, and α^{-1} is the evanescent wave decay length given by,

$$\alpha = \frac{4\pi}{\lambda}\sqrt{(n_1 \sin\theta_1)^2 - n_2^2} \tag{2.19}$$

where n_1 and n_2 are the refractive indices of the incident and transmitted media, and θ_1 is the incident angle. Using Eq (2.18), measurements of scattering intensity from single levitated particles can be used to monitor their height fluctuations due to Brownian excursions normal to the wall. The probability of sampling each height above the surface is related to the potential energy at that elevation by Boltzmann's equation,[21]

$$p(h) = A \exp\left[-\frac{u(h)}{kT}\right] \tag{2.20}$$

where $p(h)$ is the probability density of heights sampled by a single particle, $u(h)$ is the particle-wall potential energy profile, and A is a normalization constant related to the total number of height observations. It is worth noting that the equilibrium Boltzmann distribution, exp(-u(h)/kT), is the stationary, i.e., time-independent solution of the Smoluchowski diffusion equation, and the system asymptotically approaches this solution under equilibrium. By measuring the number of times a particle samples each height during the course of an experiment, a particle height histogram, $n(h)$, can be measured from time dependent height fluctuations. With a large number of observations to ensure sufficient statistical sampling, $n(h)$ can be considered a good approximation of

the probability density of heights, *p(h)*. The potential energy relative to a reference state can determined by measuring *n(h)*, substituting for *p(h)* in Eq. (2.20), and then rearranging as[46],

$$\frac{u(h)-u(h_{ref})}{kT}=\ln\left[\frac{n(h_{ref})}{n(h)}\right] \tag{2.21}$$

where h_{ref} is often chosen as h_m, which is the most probable height sampled in *n(h)*. This relative separation scale is generally referenced to particle-wall contact at *h=0*, which is most commonly determined by measuring I_0 in Eq (2.18).[21] The measured potential energy profile is only due to the conservative forces and is unaffected by dissipative hydrodynamic forces.

2.4 Energy Landscapes from 2D Colloid Distributions

Consider a quasi two-dimensional system, with *N* colloidal particles of radius, *a*. The average area fraction of particles in the system is $\phi=\rho_{avg}\pi a^2$, where ρ_{avg} is the average number density. For sub-monolayer colloidal fluids confined by gravity above a uniform surface, the density is homogeneous in the 2D plane parallel to the wall containing the colloids. For a similar fluid adjacent to a chemically or physically patterned substrate, interactions of colloidal particles with the underlying wall surface will cause lateral density variations. Such density variations can be described in 2D colloidal fluids approaching infinite dilution by Boltzmann's equation as,

$$\frac{u(x,y)-u_{ref}(x,y)}{kT}=-\ln\left[\rho(x,y)/\rho_{ref}(x,y)\right] \tag{2.22}$$

where $u(x,y)$ is the local dependent interaction potential between single colloids and the underlying substrate, which can be referred to as a potential energy landscape, and $\rho(x,y)$ is the time averaged 2D colloidal density. In other words $\rho(x,y)$ is the probability of finding a colloidal particle in a given x, y position. We assume that the inhomogeneous fluid can be treated as quasi 2D since the height variations are less than the colloid radius and the coverage is sub-monolayer. In the experiments with physical patterns reported in Section 4, the surface is clearly 3D, but colloids are confined to a thin region that is small compared to the radius. As the concentration of colloidal particles increases, multi-particle packing effects and many-body interactions become important and the Boltzmann inversion of concentrated $\rho(x, y)$ will yield a position dependent potential of mean force, $w(x, y)$, which we refer to as a free energy landscape in this dissertation. This effectively captures the average interaction between a single colloid and each surface location as mediated by all nearby and intervening colloids.

An "inverse" statistical mechanical analysis is the formal method for working backward from the measured inhomogeneous fluid microstructure captured by $\rho(x, y)$. The goal is to extract the interaction of single colloids with the underlying physically patterned surface, which we refer to as a potential energy landscape, $u(x, y)$. To accurately recover $u(x, y)$ by accounting for many-particle effects, we have developed an inverse Monte Carlo (MC) simulation method. Monte Carlo (MC) simulations are traditionally used in a "forward" fashion to predict $\rho(x,y)$ for a given $u(x,y)$. Conversely, the inverse MC algorithm employs iterative forward canonical MC simulations with different guesses for $u(x, y)$ until a simulated $\rho_S(x, y)$ is obtained in agreement with the

measured $\rho(x, y)$. To ensure rapid convergence to a unique solution, revised estimates for energy landscapes are obtained in an iterative fashion using,

$$u(x,y)_{i+1} = u(x,y)_i + \alpha kT\left[\left(\rho_s(\mathrm{x,\,y})_\mathrm{i} - \rho(\mathrm{x,\,y})_\mathrm{i}\right)/\rho_s(\mathrm{x,\,y})_\mathrm{i}\right] \tag{2.23}$$

where α is a damping parameter often empirically adjusted between 0 and 1 to optimize convergence. The value of $\alpha = 0.5$ worked well for all cases we have examined. An advantage in using this potential perturbation routine is that no numerical problems arise when $\rho_s(x,y)=0$.

The free energy landscape, $u(x, y)_0=w(x, y)=\ln[\rho(x, y)]$ is used to initialize the inverse MC algorithm. The algorithm in Eq. (2.23) is sufficiently robust that convergence to a unique global solution is still obtained if $u(x, y)_0=0$. This procedure is repeated until convergence is obtained as determined by some tolerance in the root mean square (rms) error averaged over all surface positions between $\rho_s(x,y)$ and the specified inhomogeneous fluid distribution $\rho(x,y)$ as,

$$\chi_i = \left(\frac{1}{XY}\sum_{j=1}^{X}\sum_{k=1}^{Y}\left(\rho_s\left(x_j, y_k\right)_i - \rho\left(x_j, y_k\right)\right)^2\right)^{0.5} \tag{2.24}$$

where χ_i is the rms error for a given iteration. With convergence of $\rho_s(x,y)$ to $\rho(x,y)$, a unique solution is obtained for the potential energy landscape provided that more than one $u(x,y)$ does not satisfy Eq. (2.23) within the specified tolerance. The simulation was stopped if the solution diverged (rms error increases) or if the convergence was oscillatory. The evolution of the R-square correlation, a parameter that quantifies the

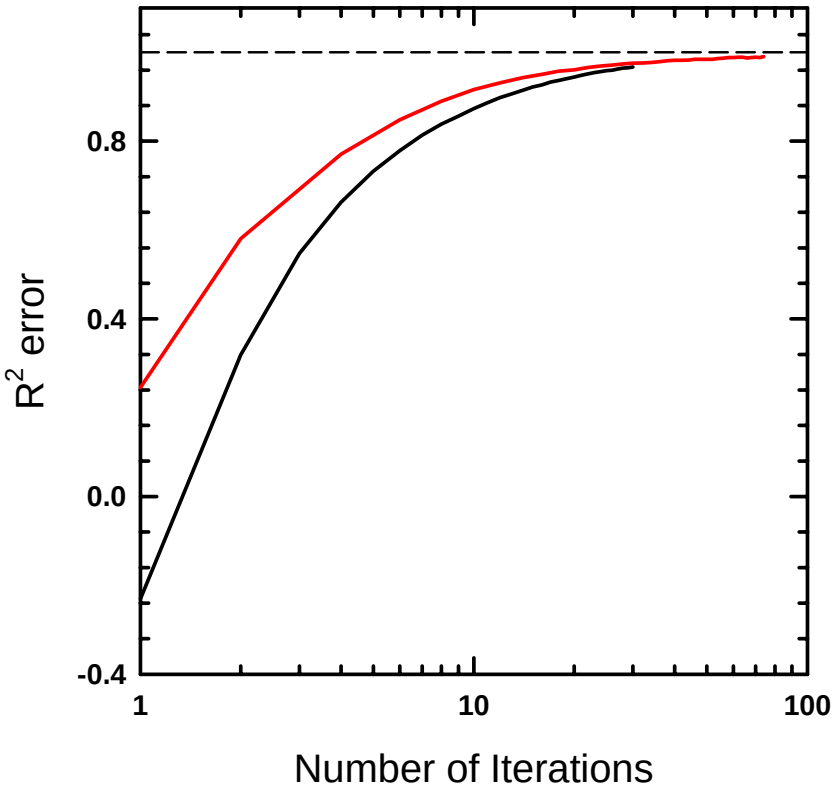

Figure 2.1. The R-square error between the simulated and measured density distribution functions plotted as a function of the number of iMC iterations. The convergence characteristics correspond to diffusing colloidal probe microscopy experiments described in Section 4 for two particle concentrations, ϕ_{eff}=0.14 (red) and ϕ_{eff}=0.28 (black).

variation of the simulated distribution function $\rho_s(x,y)$ from the measured $\rho(x,y)$, is

shown in Fig. 2.1 for two iMC simulations described later in Section 4. The R-square value is a fraction of the variance in the data and approaches unity as the regression approaches a perfect fit. Figure 2.1 is included in this section to illustrate the fact that the iMC simulation algorithm uniformly converges to a unique solution in typically less than 100 iterations.

Another important issue concerning convergence of iMC algorithms is the statistical quality of measured distribution functions. However, there are no available criteria to independently assess if the statistical quality of the experimental data collected is good enough for the iMC method. It is possible that a very noisy experimental target function can introduce additional local minima, and impede convergence by allowing the possibility for the optimization routine in the iMC method to be stuck in one of the local minima while scanning for the global minimum. While more elaborate algorithms that facilitate escape from any local minima in the solution space can improve the ability to obtain a unique $u(x,y)$ in the presence of significant experimental noise, this was not considered in this work and reserved for future study. The details of the inverse Monte Carlo algorithm are represented as a flowchart in Fig. 2.2.

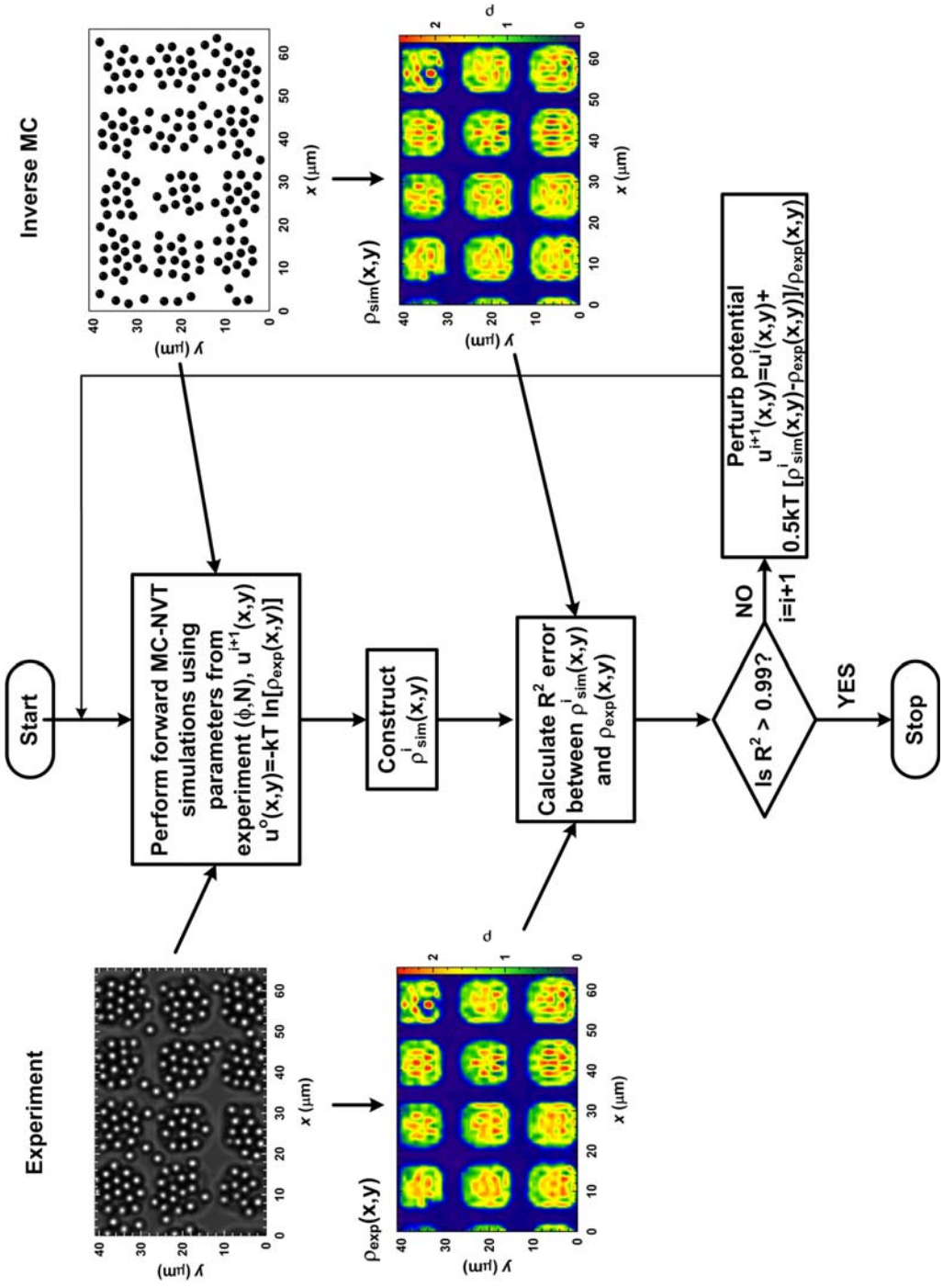

Figure 2.2. Flowchart detailing the inverse Monte Carlo algorithm used to obtain two-dimensional energy landscapes, $u(x,y)$, from measured equilibrium distribution functions $\rho_{exp}(x,y)$.

3. EXPERIMENTAL METHODS

3.1 Materials

3.1.1 Colloidal particles

A variety of colloidal particles (types and sizes) supplied by different vendors were used in this dissertation without further purification. Nominal 2.34 μm silica colloids purchased from Bangs Laboratories (Fishers, IN) were used as diffusing colloidal probes to image energy landscapes in Section 4. Colloidal assembly experiments with electric fields were conducted using both dielectric and metallic particles. In Section 5, 3 μm silica colloids purchased from Bangs Laboratories (Fishers, IN), and Polystyrene microspheres (4 μm and 4.9 μm) purchased from Interfacial Dynamics Corporation (Portland, OR) were used in experiments with normal electric fields due to homogeneous and patterned electrode surfaces. Polydisperse metallic gold nanoparticles (Alfa Aesar, Ward Hills, MA) with an average diameter of 800nm were used in experiments with the interdigitated planar microelectrodes in Section 6. The manufacturer reported particle densities were ρ_{SiO2}=1.96 g/ml, ρ_{PS}=1.05 g/ml, and ρ_{Au}=19,000 g/ml. In each experiment, particles were diluted in aqueous electrolyte solutions to obtain bulk particle concentrations that produced desired interfacial concentrations after sedimentation equilibrium was attained.

3.1.2 Ionic solution

The water used in these studies was deionized (DI) water from an in-house purification system. It typically had a conductivity of around 1 μS cm^{-1}. Electrolyte

solutions were prepared using analytical grade $NaHCO_3$ (Sigma), NaCl (Aldrich) and KOH (Fisher) without further purification. Typically 0.15 or 1.0 mM $NaHCO_3$ or KOH was used in the colloidal assembly experiments with external electric fields in Sections 5 and 6. All experiments in Section 4 were performed using DI water. The pH of the electrolyte solutions was maintained well above the isoelectric point of the colloidal particles to ensure a negative surface charge.

3.1.3 Glass substrates and electrodes

Microscope glass slides from Corning (Corning, NY) were used as substrates in all experiments reported in this work. For the experiments with electric fields, two types of electrodes were used: gold, a conductor; and tin-doped indium oxide (ITO), a semiconductor. Optically transparent Indium-Tin-Oxide (ITO) electrodes were supplied by Delta Technologies and consisted of a 150nm thick layer of ITO deposited on a 1.1 mm thick glass slide. The sheet resistance was reported by the manufacturer to be 10 Ω/sq. Interdigitated gold microelectrodes were patterned on glass substrates using standard photolithography techniques described later in this section. To check for the quality of electrodes and the presence of a good conducting film, the resistance of the electrodes was measured prior to use. Electrical connections to the ITO electrode were made using conductive silver epoxy, while the gold electrodes allowed connecting wires to be soldered onto the contact pads in the microelectrode geometry.

3.1.4 Cleaning procedures and cell preparation

Glass surfaces were cleaned with piranha solution (3:1 mixture of 99% H_2SO_4 to 35% H_2O_2) for 1 hr to remove organic contaminants and increase the surface charge. The ITO and gold electrodes were cleaned using sequential washes with 200 proof ethanol and deionized water. It is important to avoid using acetone to clean ITO electrodes as ketones deposit a film residue on the surface thereby passivating the electrode. Laboratory grade ethanol also contains ketone as a denaturant, making it necessary to use absolute ethanol for cleaning the ITO electrodes. After washing the substrates with deionized water (DI) and drying with high purity nitrogen prior to use, polydimethylsiloxane (PDMS) or Viton O-ring (10mm ID x 12 mm OD, McMaster Carr, Los Angeles, CA) spacers were attached to the glass surface to produce a small batch sedimentation cell. Viton O-rings were attached to the glass slides with quick setting epoxy or vacuum grease; PDMS spacers could be sealed to clean glass surface without adhesives due to low-density chemical bonding between the free silanol groups in the PDMS and oxide on the glass surface. The density of chemical bonding can be increased substantially by exposing the PDMS to oxygen plasma before attachment.

3.1.5 Material characterization

The size of the colloidal particles was characterized using 1) dynamic light scattering (DLS) (ZetaPALS instrument, Brookhaven Instrument Corp., Holtsville, NY), 2) ensemble averaged Total Internal Reflection Microscopy (ETIRM) measurements of particle-wall interaction potential, 3) pair distribution functions of colloids dried on a microscope slide, and 4) Confocal Laser Scanning Microscopy (CLSM) (LSM 5

PASCAL, Zeiss, Germany). In DLS measurements, the colloidal particles were dispersed in a 1mM NaCl solution, and approximate size distributions were obtained using standard procedures applying cumulate analysis provided in the DLS software. The average colloidal particle diameter can also be extracted from the ETIRM measured gravitational potential energy, as explained in Section 2. The position of the first peak in the radial distribution function constructed for colloidal ensembles dried on a microscope slide can also provide an estimate of the particle size. In CLSM measurements, colloidal particles were first dispersed in DI water to obtain bulk particle concentrations that produced monolayer concentrations after sedimentation. The colloidal dispersion was then allowed to sediment in a batch sedimentation cell for a couple of hours after which ~0.05% (weight) Rhodamine 6G (Aldrich, Milwaukee, WI) and 1 M NaCl solution was injected into the cell to generate a fluorescent medium. A 100X oil immersion objective (N.A. = 1.4) was used to capture images in the fluorescent mode. 92μm x 92μm images were obtained with 2048 x 2048 resolution to produce ~45nm pixels, which allowed centroid location to within ~20nm using typical particle tracking algorithms. An image processing algorithm using fast Fourier transform (not described in this dissertation) was used to find the center and diameter from the cross section of the particle. Figure 3.1 illustrates the use of methods 1 and 3 detailed above to determine the size of silica colloids used as diffusing colloidal probes in Section 4. Figure 3.2 illustrates the use of confocal microscopy (method 4) to characterize the size distribution of 4 μm PS colloids used in Section 5.

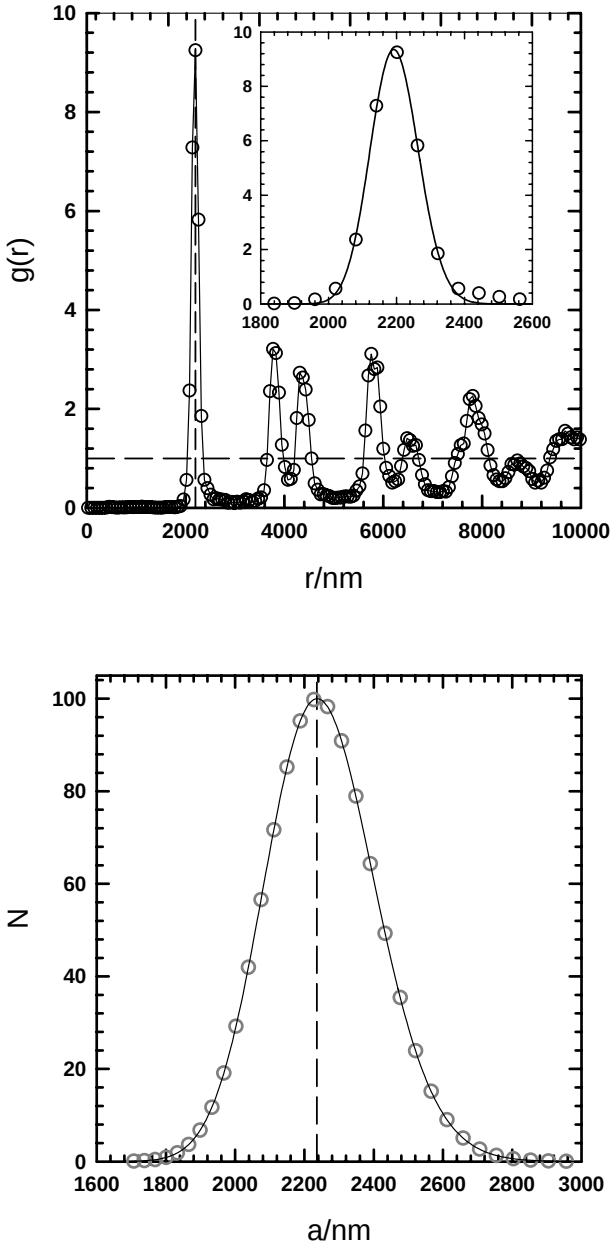

Figure 3.1. (a) Radial distribution function for nominal 2.34 μm silica colloids dried on a microscope slide with first peak at r = 2a = 2.20 μm. Inset shows the first peak magnified and the solid line (—) is a log-normal fit. (b) Dynamic light scattering data measured log-normal distribution of nominal 2.34 μm silica colloids with most probable size of 2a = 2.23 μm and a polydispersity of 7 %.

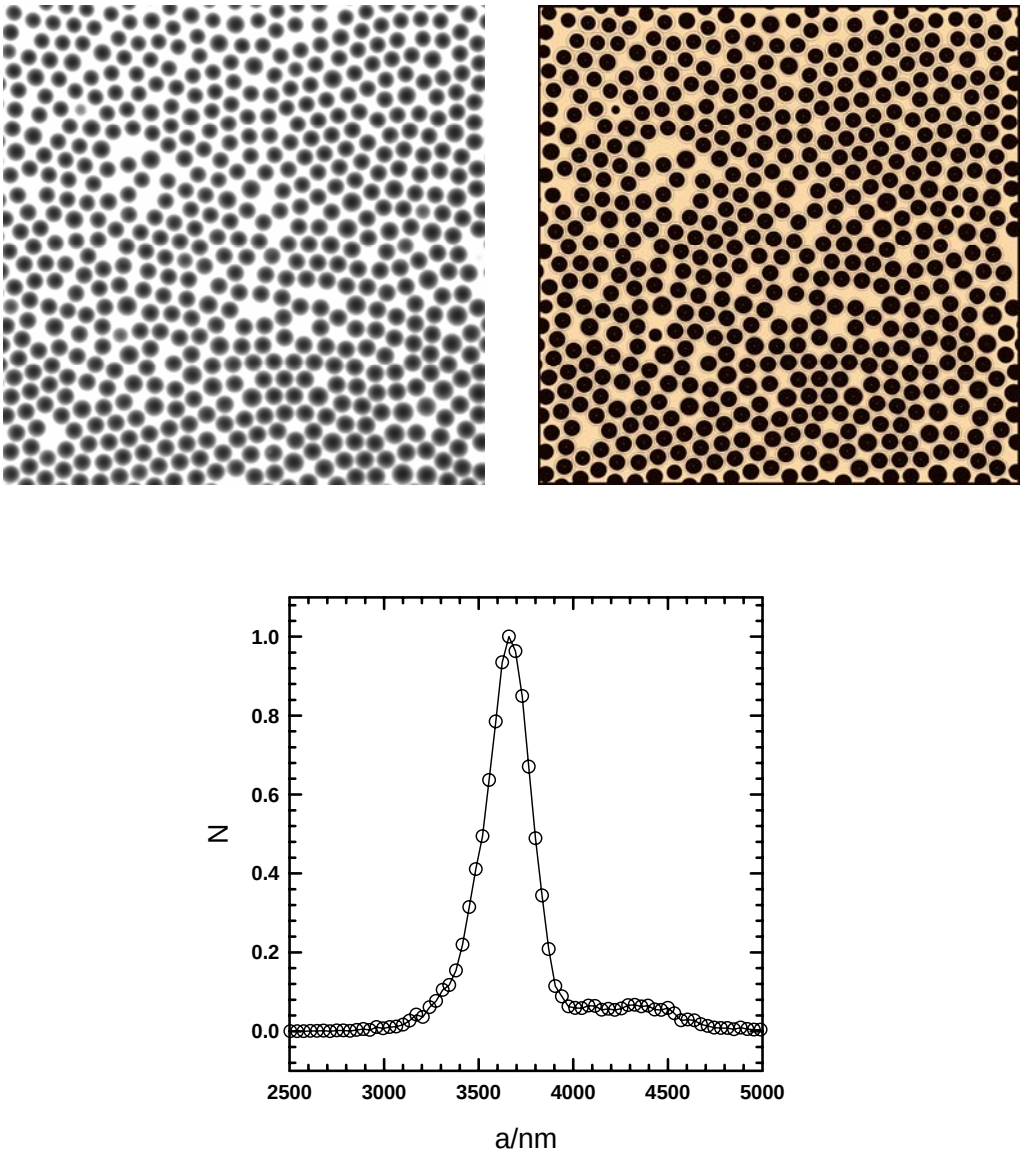

Figure 3.2. (a) Confocal image of nominal 4 μm PS particles, (b) Processed image indicating the center and circumference of individual colloidal particles, and (c) Size distribution of nominal 4 μm PS particles with most probable size of 2a=3.66 μm, constructed from processed images.

The zeta potential of the colloids as a function of pH and ionic strength was measured using dynamic light scattering and phase analysis light scattering measurements (ZetaPALS, Brookhaven Instrument Corporation, Holtsville, NY). The ionic strength and pH of the ionic solution was determined by pH and conductivity measurements (Accumet® research, AR20, Fisher Scientific).

3.1.6 Power supply and impedance analyzer

A Kepco Power supply unit (ATE 55-10DM, 0-55 V, 0-10 A) was used in the colloidal assembly experiments with DC fields in Section 5. The potential drop and current across the electrodes was measured using a Fluke 187 digital multimeter. An Agilent 33120A function generator was used to apply an alternating potential (ω=10 Hz – 1 MHz, voltage=0.5 V – 2.5 V peak to peak) to the electrodes. A Tektronix TDS210 two channel oscilloscope was used to monitor the applied AC signal. Reversing the electrical connections to the electrodes from the function generator produced no change in the measured behavior, which means there was zero DC bias in the electronics.

A Hewlett-Packard HP 4194A impedance analyzer tested and calibrated using an open/short circuit compensation routine recommended by the manufacturer, was connected in series with the function generator and the electrodes to make impedance measurements. The analyzer was interfaced to a laboratory PC using a LAB-VIEW 8.0 program (National Instruments) to collect raw data (impedance magnitude, $|Z|$, and the phase angle, δ), as a function of frequency from 100 Hz to 1 MHz. All the impedance measurements were made at a nominal oscillator voltage level of 0.25 V.

3.2 Microscopy Techniques

3.2.1 Ensemble total internal reflection microscopy (ETIRM)

Fig 3.3 shows a schematic representation of an optical microscope (Axioplan 2, Zeiss, Germany) and CCD camera setup for dynamically tracking and monitoring evanescent wave scattering from levitated colloidal particle ensembles (see inset). An O-ring/cover glass batch sedimentation cell (or a flow cell) is optically coupled to a 68° dovetail prism (Reynard Corp., CA) using index matching oil (n=1.515). The prism is then mounted on a three point leveling stage. In particle-wall potential energy measurements, a 40X objective (NA=0.65) and 1.6X magnifying lens were used in conjunction with a 12 bit CCD camera (ORCA-ER, Hamamatsu, Japan) operated at 4x binning (128μm x 97μm images were obtained with 336 x 256 resolution to produce ~379nm pixels). Images were recorded at 27 frames/sec with a total observation time of 37 minutes to produce images stacks of 6.0×10^4 frames. A 15 mW, 632.8 nm Helium-Neon laser (Melles Griot, Carlsbad, CA) provided photons for the generation of an evanescent wave with a decay length of 236 nm (n_g=1.515, n_w=1.333). While large penetration depths allow particle heights to be measured over a larger range (needed for experiments with DI water), small penetration depths lead to greater sensitivity.

To track each particle's three dimensional trajectory, we use typical image analysis algorithms[22] coded in Fortran to locate x,y center coordinates (~10 nm) on each scattering pattern, and integrate each particle's scattering intensity to obtain the center

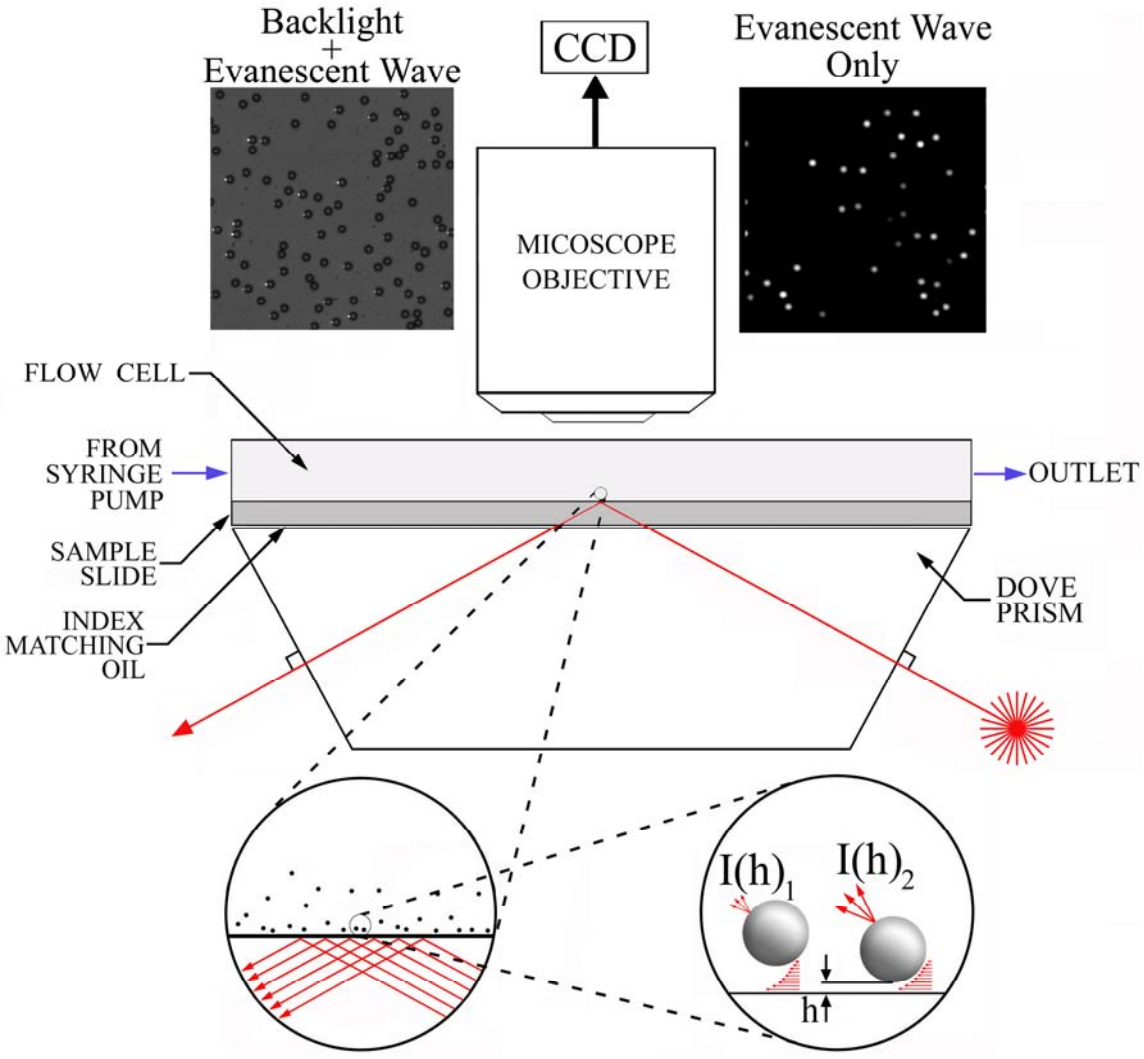

Figure 3.3. Schematic illustration of the ETIRM apparatus with HeNe laser, prism, batch cell, microscope, CCD camera, and data acquisition PC. Insets shows schematic representation of levitated particle scattering evanescent wave with intensity, *I(h)*, as a function of particle-wall surface separation, *h*. CCD image from top view of levitated particles scattering evanescent wave (white spots) with transmitted light illuminating particles (dark rings) is also shown.

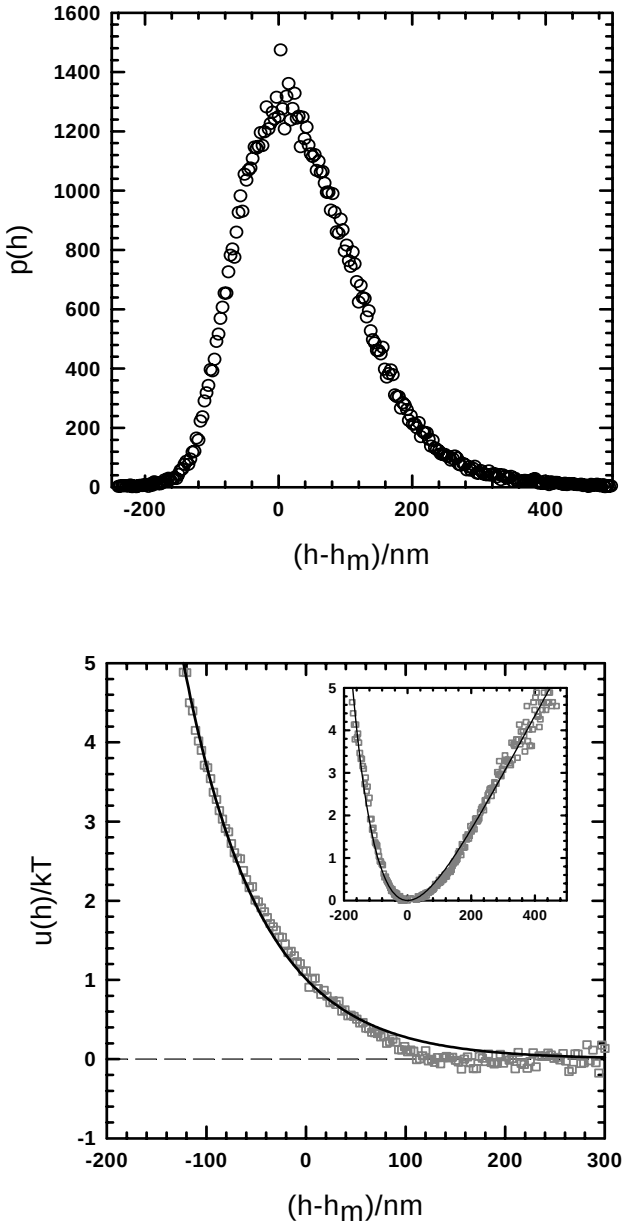

Figure 3.4. TIRM measurements of particle-wall interaction potential between 2.34 μm silica colloids in DI water interacting with a glass substrate. (a) Ensemble averaged particle-wall distribution function. (b) Ensemble averaged particle-wall potentials determined from the probability density function in (a) using Boltzmann's equation (Eq. (2.1)). Solid lines (—) are theoretical DLVO fits to the measured potential.

height above the bottom surface, z (~1 nm) (see Section 2 and Fig. 3.3). Figure 3.4 shows representative results from a typical ETIRM experiment that measured the ensemble particle-wall interaction potential between 2.34 μm silica colloids in DI water interacting with a glass substrate. An average particle size of 2.27 μm and a Debye screening length of κ^{-1}=89nm, was obtained from the theoretical fits to the measured potential energy profile. These measurements provide essential information important to the experiments described in Section 4.

3.2.2 Video microscopy (VM)

Diffusing colloidal probe tracking measurements were conducted using an inverted microscope (Axiovert 100A, Zeiss). The sedimentation batch cells were placed on a three point levelling stage and adjusted for particle migration prior to the experiment. Bright field digital images were obtained using a 63X objective (NA=0.75, Zeiss) and a 1.6X magnifying lens in conjunction with a 12 bit CCD camera (ORCA-ER, Hamamatsu) operated with 2x binning. A sequence file of equilibrium particle configurations was recorded at 18 Hz, with total observation times depending on the nature of the experiment. 66μm x 41μm images were obtained with 608 x 404 resolution to produce ~100nm pixels, which allowed centroid location to within ~50nm using typical particle tracking algorithms.[22] The details of the image analysis algorithm used are not repeated in this dissertation for the sake of redundancy. All image analysis was performed using single-processor PC's and multi-page TIFF files containing up to 10^5 608 x 404 separate images.

3.2.3 Atomic force microscopy

The physical landscapes microfabricated on glass substrates were imaged using Atomic Force Microscopy (AFM) amplitude and height images. AFM images were acquired in air under ambient conditions using a Nanoscope IIIa multimode scanning probe (Veeco Digital Instruments, Santa Barbara, CA) operated in tapping mode (scan rate = 0.15 Hz). Silicon nitride cantilever tips with a spring constant of 0.06 N/cm, and a tip radius of curvature of <10 nm were used. When operated in tapping mode, the cantilever assembly is oscillated at a frequency just below the resonant frequency (≈300 kHz) using a piezoelectric crystal. The depth and periodicity of the physical features to be imaged would require a much slower scan speed if the AFM was to be operated in contact mode. The height information from the high resolution topographical scan (512 x 512 pixels) was exported from the AFM software and re-binned at a lower resolution (pixel=1.6μm) for direct comparison with diffusing colloidal probe generated images having an identical resolution as described in Section 4.

3.3 Microfabrication

3.3.1 Patterning physical patterns on glass substrates

Conventional photolithographic techniques (Fig 3.5) were used to create the patterned glass substrates used in this study, and all microfabrication steps were conducted in a class 1000 clean room. To begin, microscope slides (pre-cleaned Gold Seal® micro slides, Gold Seal® Products, Portsmouth, New Hampshire) were immersed in piranha solution (3:1 mixture of H_2SO_4 to 30% H_2O_2; *caution: dangerous oxidizing*

agent) for 1 hour to remove organic contaminants. Slides were then rinsed thoroughly with DI water and dried with a stream of compressed air, and further baked at 200 ºC for 5 minutes in a contact hotplate to dehydrate the surface.

A SU-8 2002 (MicroChem, Newton, MA) photoresist layer, ~ 1 μm thick, was applied to the slides by dispensing 1 ml of photoresist onto the glass substrate and spinning it at 4000 rpm for 30 seconds. Physical patterns were created with negative photoresist (SU-8 2002) instead of positive resist, because of the reduced susceptibility to etching with the crosslinked mask. The photoresist was soft baked on a hotplate at 95 ºC for 2 minutes and exposed to ultraviolet (UV) light through a patterned mask for 20 seconds. Following exposure, a two-step post expose bake was performed 1) 1 minute at 65 ºC, and 2) 1 minute at 95 ºC, to selectively cross-link the exposed portions of the photoresist film. The substrate was then immersed in MicroChem's SU-8 developer for 60 seconds. Following development, the photoresist pattern was placed in a reactive ion etcher (CS-1701, March Plasma Systems, CA) and exposed to oxygen plasma for 30 s at 200 W and with an O_2 flow rate of 0.3 cm^3/s to remove any photoresist and developer residue on the glass regions.

Physical landscapes on glass (Fig 3.6) were microfabricated by using 50% hydrofluoric acid to isotropically etch the glass within the exposed SU-8 pattern. The etch process was halted after ~3 s by thoroughly rinsing the substrate in DI water to dilute the etchant. A uniform oxide layer was formed over the entire surface by treating the patterned glass in piranha solution (3:1 of H2SO4:H2O2) for 1 hr prior to conducting surface imaging experiments using colloidal particles.

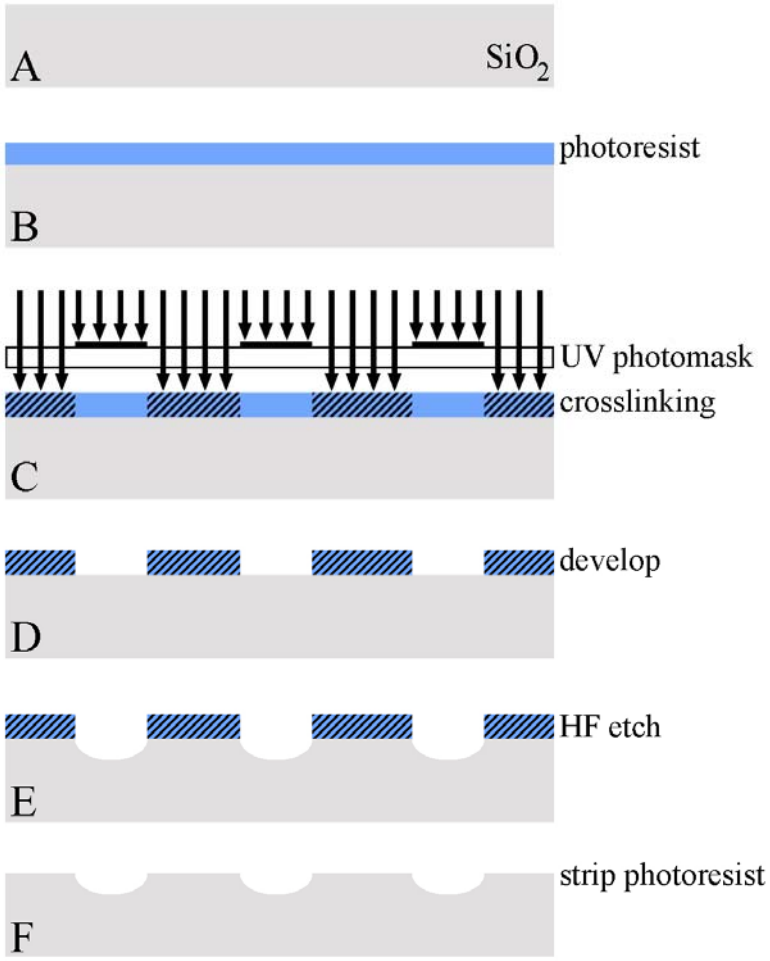

Figure 3.5. Schematic representation of the general microfabrication steps used to pattern physical features on a glass substrate.

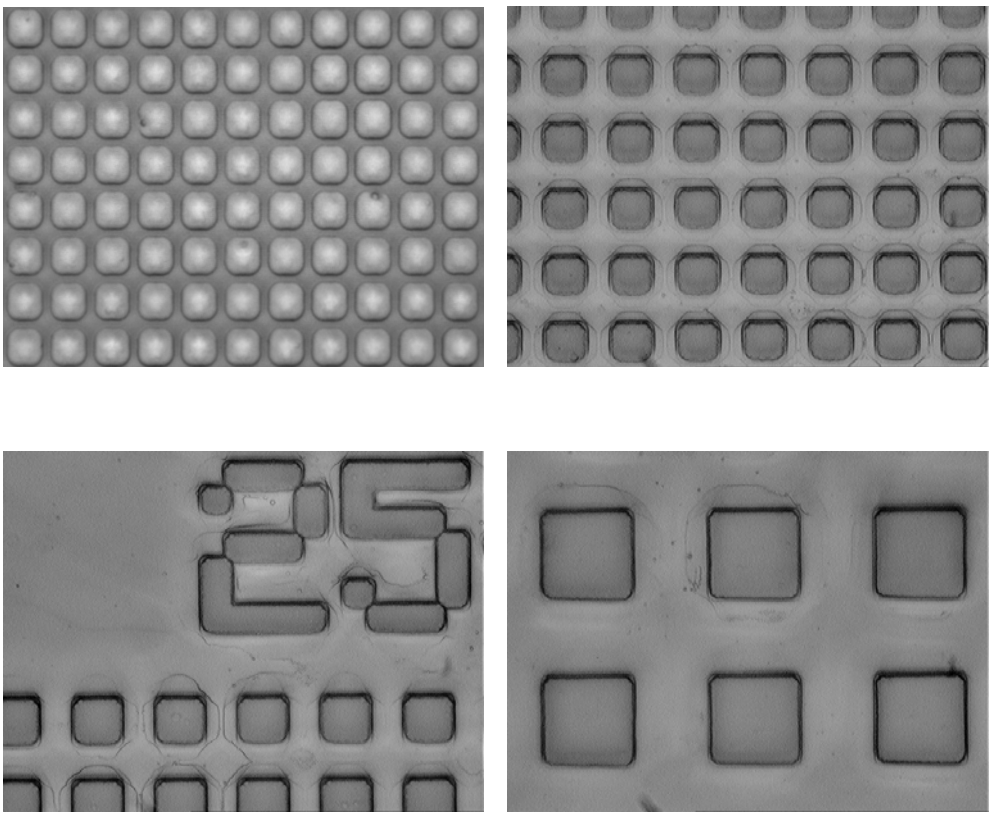

Figure 3.6. (top-bottom, left-right) CCD images of physically patterned glass substrates containing square arrays of varying sizes (a) 8 μm x 8 μm, (b) 20 μm x 20 μm, (c) 25 μm x 20 μm, and (d) 50 μm x 50 μm.

3.3.2 Patterning chemical patterns on glass substrates

Chemical micropatterns were fabricated using conventional photolithographic techniques in a class 1000 clean room (Figs 3.7 and 3.8). Microscope slides were first immersed in piranha solution (3:1 mixture of 99% H_2SO_4 to 35% H_2O_2) for 1 hr to remove organic contaminants. Slides were then rinsed thoroughly with DI water and blown dry with air. An S1813 photoresist layer (~1.5 μm thick) was applied to the slides by dispensing 1 ml of photoresist onto the preheated (115 ºC) glass substrates and spinning at 3000 rpm for 30 s. The photoresist was soft baked on a hotplate for 60 s at 90 ºC and then exposed to ultraviolet (UV) light through a patterned chrome mask for 4 s. Before being immersed in MF 319 developer for 60 s, the UV-exposed photoresist film was post baked for 120 s at 115 ºC. Following development, the photoresist pattern was placed in a reactive ion etcher (CS-1701, March Plasma Systems, CA) and exposed to oxygen plasma for 30 s at 200 W with an O_2 flow rate of 0.3 cm^3/s to remove any photoresist and developer residue on the glass regions. Slides with patterned photoresist were placed in a metal evaporator chamber (Edwards, BOC 306) and a 3 nm-thick layer of Cr was deposited at 1 Å/s followed by the Au layer at the same rate. Au thicknesses ranged from 3 to 15 nm, depending on the experiment conducted.

An alternative method to fabricate patterned Au films on glass microscope slides without using any photoresist is by metal evaporation using TEM grids as masks. Glass slides are re-cleaned prior to metal deposition by soaking in piranha solution (3:1 H_2SO_4:H_2O_2) for 1hr and then rinsing with DI water. TEM grids are placed in top of glass slide surfaces in a metal evaporation chamber. A 2-3 nm Cr layer is initially

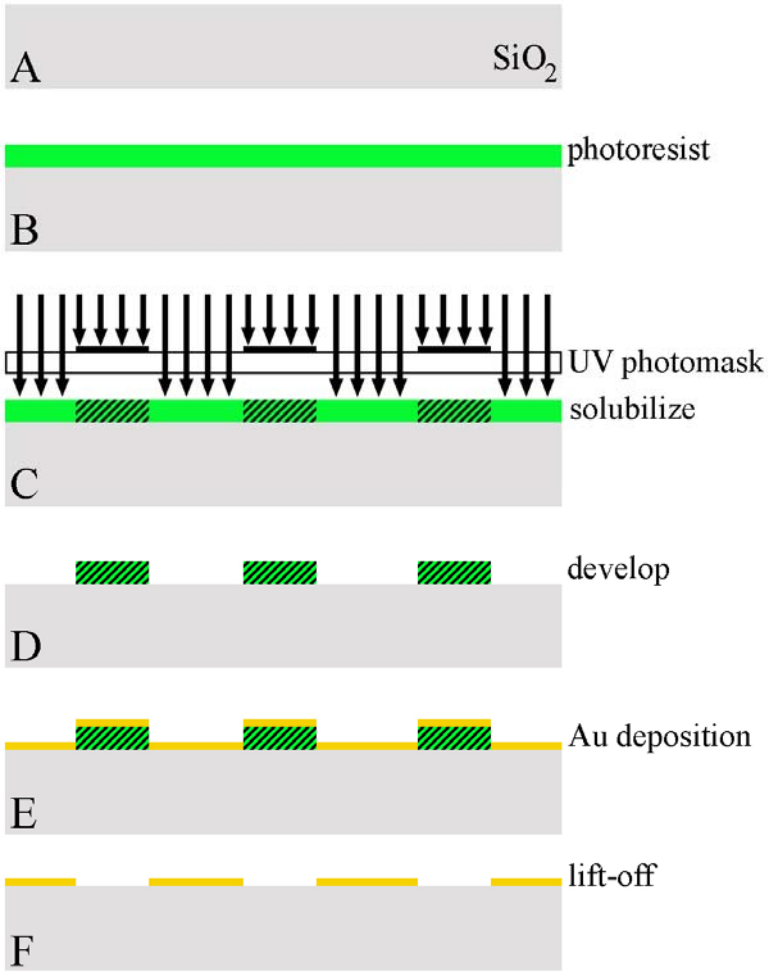

Figure 3.7. Schematic representation of the general microfabrication steps used to create chemical patterns on a glass substrate.

deposited at 0.15 nm/s to improve Au film adhesion and then 2-15 nm Au films are deposited at 0.15 nm/s.

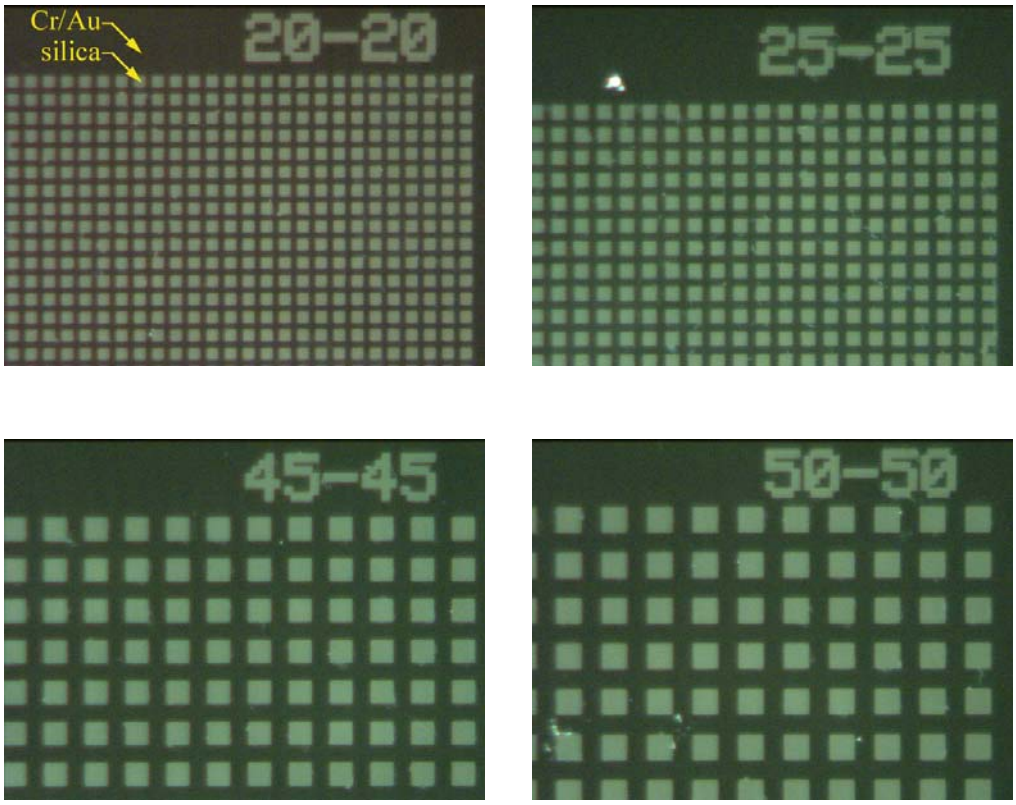

Figure 3.8. (top-bottom, left-right) CCD images of chemically patterned substrates containing square arrays of varying sizes (a) 20 μm x 20 μm, (b) 25 μm x 25 μm, (c) 45 μm x 45 μm, and (d) 50 μm x 50 μm. The darker regions correspond to a 10 nm Au film vapor deposited onto a glass surface through a photoresist mask.

4. IMAGING ENERGY LANDSCAPES WITH CONCENTRATED DIFFUSING COLLOIDAL PROBES

4.1. Synopsis

The ability to locally interrogate interactions between particles and energetically patterned surfaces provides essential information to design, control, and optimize template directed self-assembly processes. Although numerous techniques are capable of characterizing local physicochemical surface properties, no current method resolves interactions between colloids and patterned surfaces on the order of the thermal energy kT, which is the inherent energy scale of equilibrium self-assembly processes. Here, we describe video microscopy measurements and an inverse Monte Carlo analysis of diffusing colloidal probes as a means to image three dimensional free energy and potential energy landscapes due to physically patterned surfaces. In addition, we also develop a consistent analysis of self-diffusion in inhomogeneous fluids of concentrated diffusing probes on energy landscapes, which is important to the temporal imaging process and to self-assembly kinetics. Extension of the concepts developed in this work suggest a general strategy to image multi-dimensional and multi-scale physical, chemical, and biological surfaces using a variety of diffusing probes (i.e. molecules, macromolecules, nanoparticles, colloids).

4.2. Introduction

The ability of microscopic components to autonomously and reversibly self-assemble on energetic templates is broadly considered as an enabling process to numerous emerging technologies.[1,2,8] As a result, there is intense interest in understanding how thermal motion, particle interactions, template features, and potential fields can be optimally coupled to elicit desired material and device responses. One fundamental hurdle to specifying design rules and control parameters in self-assembly processes arises from current limitations on directly interrogating multi-body and multi-dimensional kT-scale interactions that influence equilibrium and dynamic structures on energetic templates. Although statistical mechanics has been applied with success to understand equilibrium phase behavior and structures of some of the most basic, model, bulk, homogeneous, single component materials, the application of these methods to inhomogeneous fluids and phase transitions of such fluids next to patterned surfaces is still in its infancy.

To robustly design and control such templated colloidal self-assembly processes in an informed manner, it is essential to be to able to directly and quantitatively measure, interpret, and predict the connections between equilibrium structure formation and the weak forces operating between colloids and surface pattern features. In other words, to render the design of such assembly processes as anything other than an art form, it is necessary to gain fundamental understanding such that *a priori* principles can be used to intelligently specify the range and magnitude of colloidal and patterned surface potentials and the minimum number of thermodynamic variables to specify the system

(i.e. Gibb's phase rule). Likewise, to apply standard feedback loop control to templated colloidal self-assembly processes, it is necessary to know how to tune a controllable variable to elicit the desired response in some process variable, which is basically structure in this case. For example, if a desired structure is not forming in a given assembly process, the ideal way to control the process is to know how to tune some thermodynamic variable based on a first principles model of how the structure should respond to such a change to bring the process variable into agreement with the set variable (the alternative to a first principles model is the learned behavior of a given process, which is fine for an already known process over a relatively narrow range of conditions, but does not guide the initial design of processes from an infinitely available variable phase space).

Scanning probe techniques represent the state-of-the-art for "imaging" physical,[49-51] chemical,[52,53] and biomolecular,[54,55] patterned surfaces by monitoring mechanical deflections of cantilevers at different positions relative to surfaces. However, such methods cannot resolve interactions too weak to produce measurable cantilever deflections. From another perspective, active probe manipulation that enables scanning inherently requires forces stronger than those involved in autonomous self-assembly processes that do not allow any external manipulation. As a result, scanning probes perturb any system equilibrated via characteristic interactions weaker than probe forces exerted in the measurement process.[56]

Here, we demonstrate how non-intrusive observation of an ensemble of colloids diffusing past each other and over physical pattern features can be used to sensitively

image surface topographies. In particular, we analyze how different interfacial concentrations of Diffusing Colloidal Probes (DCP) sample pattern features using an Inverse Monte Carlo (IMC) algorithm, which we exploit to interrogate free energy and potential energy landscapes on the order of the thermal energy kT. Because consideration of many-colloid packing effects in addition to the potential energy landscape presents a non-trivial analytical theoretical problem (that might be tackled via Density Functional Theory (DFT) for example), in practice we use inverse Monte Carlo simulations to determine the potential energy landscape from the measured inhomogeneous fluid structure. In addition, we also develop a simple expression for self-diffusion of DCP on landscape features by capturing the combined effects of multi-body hydrodynamic interactions, particle escape rates from free energy wells, and cooperative rearrangements associated with particles moving through their coordination shell.

Complexity is minimized in this initial study by using colloids having purely electrostatic repulsive interactions with each other and the underlying patterned surface. As will be discussed in further detail, the physical variation of the surface topography is small compared to the colloid dimensions and the gravitational length scale is much less than the colloid dimension (~ 0.1) so that such systems can be considered as quasi two dimensional (2D). The phase behavior of such quasi 2D colloidal fluids can be modeled with a single thermodynamic variable, the effective hard disk area fraction, to produce only a single fluid phase at concentrations short of fluid-solid co-existence (and generally only a single hexagonal close packed solid phase). Although such fluids are

laterally homogeneous when observed next to a physically and chemically uniform surface, the introduction of a physically pattern underneath an effective hard disk fluids produces density variations as the result of the potential energy landscape that is mediated by gravitational interactions only. However, because many-colloid packing effects also modulate the colloidal fluid structure in combination with the underlying potential energy landscape, there exists a free energy landscape that is required to connect all energetic and entropic contributions.

By passively monitoring DCP, our method exploits stochastic thermal motion as a natural gauge of *kT*-scale energy landscape features rather than avoiding it as an undesirable complication of microscopic systems. Our approach is ultimately intended to provide an opportunity to synergistically employ the very same colloids as both imaging probes and building blocks in feedback controlled self-assembly on patterns.

4.3. Experimental Section

Nominal 2.2μm SiO_2 colloids (Bangs Labs) with a reported density of ρ_{SiO2}=1.96 gram/ml were used as DCP. They were diluted in aqueous de-ionized water to obtain desired interfacial concentrations after sedimentation onto the patterned surface. Two average DCP concentrations were investigated with effective area fractions of ϕ_{eff}=0.14 and ϕ_{eff}=0.28, where $\phi_{\text{eff}}=\rho_{\text{avg}}\pi a_{\text{eff}}^2$, ρ_{avg} is the average number density, and a_{eff} is the effective colloid radius from the first peak in the projected 2D radial distribution function, $g(2a_{\text{eff}})$.[57] Measurements of $g(2a_{\text{eff}})$ and the most probable colloid-wall separation, $p(h_{\text{m}})$, over the homogeneous glass surface[57] indicated a uniform distance of

closest approach between colloids and the surface of ~500 nm due to electrostatic repulsion.

DCP tracking measurements were conducted using an inverted microscope (Axiovert 100A, Zeiss). Bright field digital images were obtained using a 63X objective (NA=0.75, Zeiss) in conjunction with a 12 bit CCD camera (ORCA-ER, Hamamatsu). For interfacial DCP concentrations of ϕ_{eff}=0.14 and ϕ_{eff}=0.28, images were recorded at 18 frames/sec with total observation times of 83 and 134 minutes to produce image stacks of $9.0x10^4$ frames and $1.5x10^5$ frames. 66μm x 41μm images were obtained with 608 x 404 resolution to produce ~100nm pixels, which allowed centroid location to within ~50nm using typical particle tracking algorithms.[22]

4.4. Results and Discussion

4.4.1 Concentrated diffusing colloidal probes on patterned surfaces

To investigate the use of DCP to image energy landscapes, we first microfabricated a model surface pattern consisting of an array of nearly harmonic potential wells. Quick HF exposure of a photomask on a glass slide yielded an array of nominal 13μm x 13μm x 800nm features with 3μm separation over a 1mm x 0.5mm area. The physically varying topography was characterized via AFM (Nanoscope III, Veeco Digital Instruments) amplitude and height images (Figs. 4.1 A, B). The AFM amplitude image reveals fine microstructure due to the etching procedure, whereas the height image is rendered at a lower resolution (~1μm^2 pixels) for comparison with surface topographies imaged using DCP.

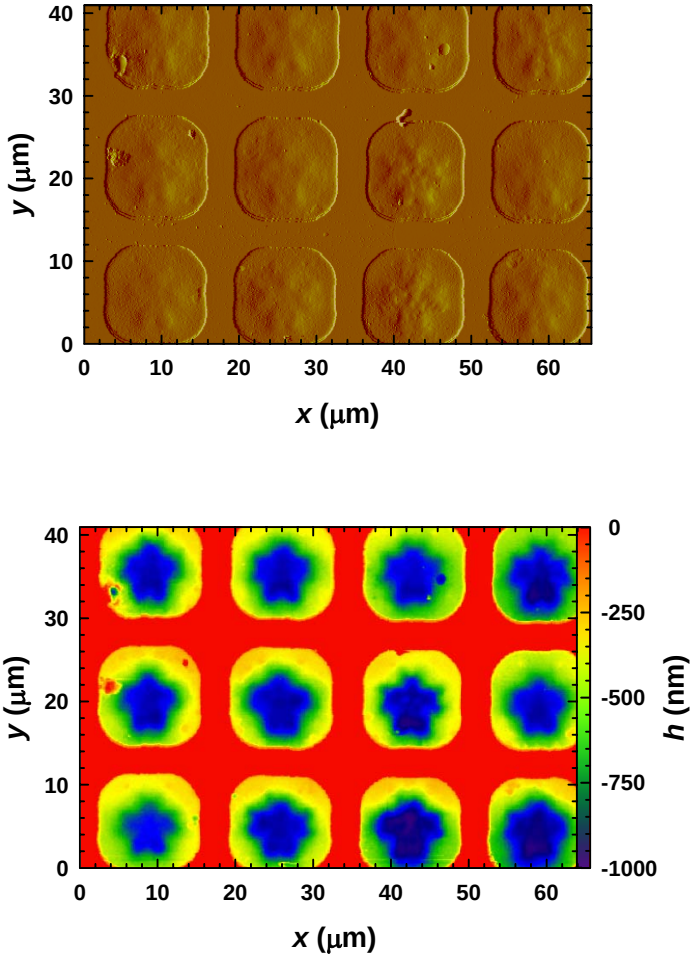

Figure 4.1. AFM (**A**) amplitude and (**B**) height images of a physically patterned glass microscope slide.

We then tracked the centers of concentrated 2.2μm SiO_2 colloids diffusing over the patterned surface topography (Fig. 4.1). The DCP are confined as sub-monolayer colloidal fluids on the patterned surface by gravity, but remain levitated above the surface and stable against aggregation by repulsive electrostatic interactions in de-ionized water. Static images show instantaneous DCP configurations for two average

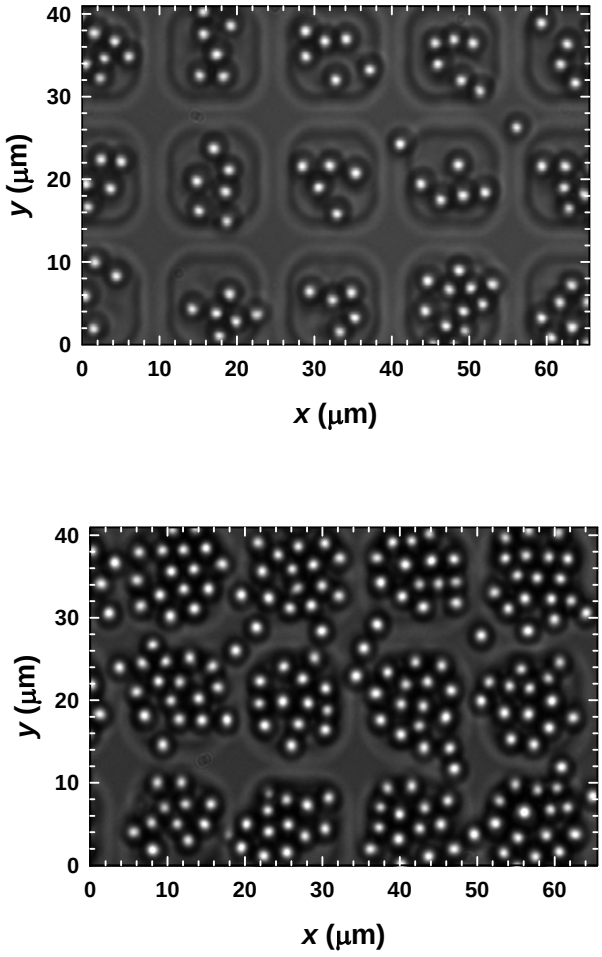

Figure 4.2. Optical microscopy images of equilibrium configurations of levitated 2.2μm SiO_2 colloids on the patterned surface with concentrations of (A) ϕ_{eff}=0.14 and (**B**) ϕ_{eff}=0.28.

surface concentrations with effective area fractions of ϕ_{eff}=0.14 and ϕ_{eff}=0.28 (Figs. 4.2 A, B). These images clearly illustrate how the local DCP concentration is modulated by the underlying 3D surface topography. To avoid misconceptions from the static images in Figs. 4.2 A, B, it should be noted that DCP are not irreversibly deposited or completely localized within pattern features but continuously diffuse over the entire surface in dynamic equilibrium.

We then characterized the time-averaged equilibrium distributions of DCP on the patterned surface topography (Figs. 4.2 A, B) as 2D density profiles, $\rho(x, y)$ (Figs. 4.3 A, B). Such 2D $\rho(x, y)$ sufficiently capture the equilibrium DCP sampling of the surface with the assumption that DCP are distributed as quasi-2D inhomogeneous fluids. This assumption is based on the fact that both the variations in $h(x, y)$ and the DCP excursions normal to the surface are small compared to the colloid diameter (~2.2μm). Measured $\rho(x, y)$ were constructed by (1) locating DCP *x, y* center coordinates to within ~50nm in $\sim 10^5$ images, (2) creating 2D population histograms on a grid of ~1μm^2 pixels, and (3) normalizing by the average number density, ρ_{avg}, in each case. The pixel dimensions, observation period, and number of frames were optimized based on DCP self-diffusion timescales and as a compromise between lateral resolution and statistical noise in the measured $\rho(x, y)$.

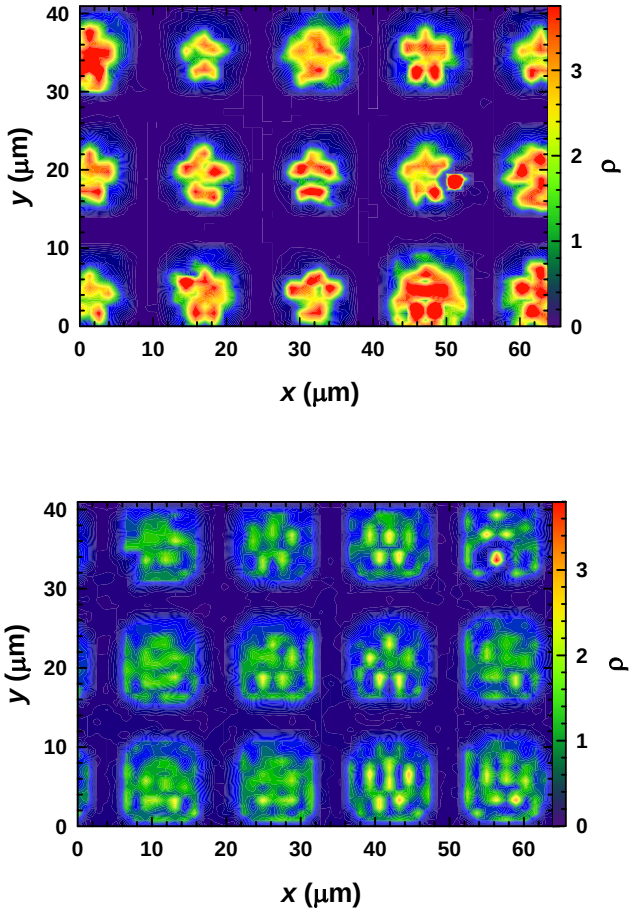

Figure 4.3. Time averaged 2D colloid density, $\rho(x, y)$, from colloid centers located in the (A) low and (B) high concentration cases in Figs. 4.2 A, B.

4.4.2 Free energy and potential energy landscapes

We then set out to interpret measured $\rho(x, y)$ (Figs. 4.3 A, B) as images of the underlying energy landscape by understanding how DCP sample the physical surface topography in the presence of gravity and multi-particle packing effects. Our approach

was to determine the position dependent interaction of a single DCP with the underlying surface, which we refer to as a potential energy landscape, $u(x, y)$. To obtain the underlying surface topography, $h(x, y)$, from measured $u(x, y)$, the relative height can be related to the relative gravitational potential energy of DCP at different surface positions as,

$$h(x,y) = u(x,y)/G = u(x,y)/\left[(4/3)\pi a^3 \Delta\rho g\right] \tag{4.1}$$

where $\Delta\rho$ is the colloid and medium density difference, and g is acceleration due to gravity. As a result, it is only necessary to obtain $u(x, y)$ from DCP measured $\rho(x, y)$ to image the physical surface topography in Figs. 4.1 A, B.

To understand the role of multi-particle packing effects in these experiments, we first review the straightforward analysis of a single 2.2μm SiO_2 DCP within a single feature (Fig. 4.4). Although Boltzmann's equation, $u(x, y)=-\ln[\rho(x, y)]$, provides a simple and direct method for relating $u(x, y)$ to $\rho(x, y)$, it is only applicable in the limit of infinitely dilute DCP surface concentrations. Naively using the Boltzmann inversion to analyze $\rho(x, y)$ obtained using concentrated DCP as in Figs. 4.3 A, B produces energy landscapes (Figs. 4.5, 4.6) that display obvious differences with the AFM measured surface (Fig. 4.1 B) when transformed into $h(x, y)$ using Eq (4.1). These differences are expected since a Boltzmann inversion of concentrated $\rho(x, y)$ does not distinguish multi-particle packing effects, but instead yields the interaction of single colloids with the underlying potential energy landscape *in the presence of nearby colloids*. This interaction is the position dependent potential of mean force, $w(x, y)$, which we refer to

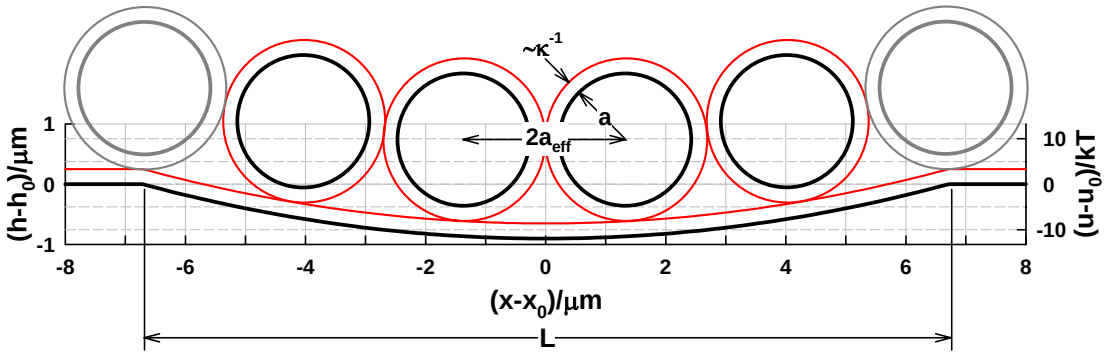

Figure 4.4. Scaled cross sectional view of 2.2μm SiO_2 colloids confined (black) and escaping (gray) from a harmonic potential energy well fit to a single AFM measured feature (Fig. 4.1 B). Red lines indicate the electrostatic double layer thickness, $\sim 3\kappa^{-1}$=250nm, that produces ~500 nm offset between colloids and the surface. Gravitational potential energy scale corresponding to physical surface topography is also shown.

as a free energy landscape.

Images of $w(x, y)$ (Figs. 4.5, 4.6) show the importance of multi-particle packing effects in how DCP sample energy landscapes with implications for colloidal self-assembly on patterns. A single colloid within a ~800nm pattern feature must escape a $12kT$ potential energy well to diffuse over the entire surface (Fig. 4.4), but colloids only need to escape $5kT$ and $2kT$ free energy wells (Figs. 4.6 A,B) for the two concentrated cases in Figs. 4.2. Free energy well depths decrease with increasing ρ_{avg} because the presence of more colloids within each well elevates some colloids closer to the well periphery to more easily overcome the smaller remaining energy difference (Fig. 4.4). This process also ensures a uniform equilibrium distribution of colloids on the pattern as too many colloids in one feature will be corrected by colloids near the edge escaping and

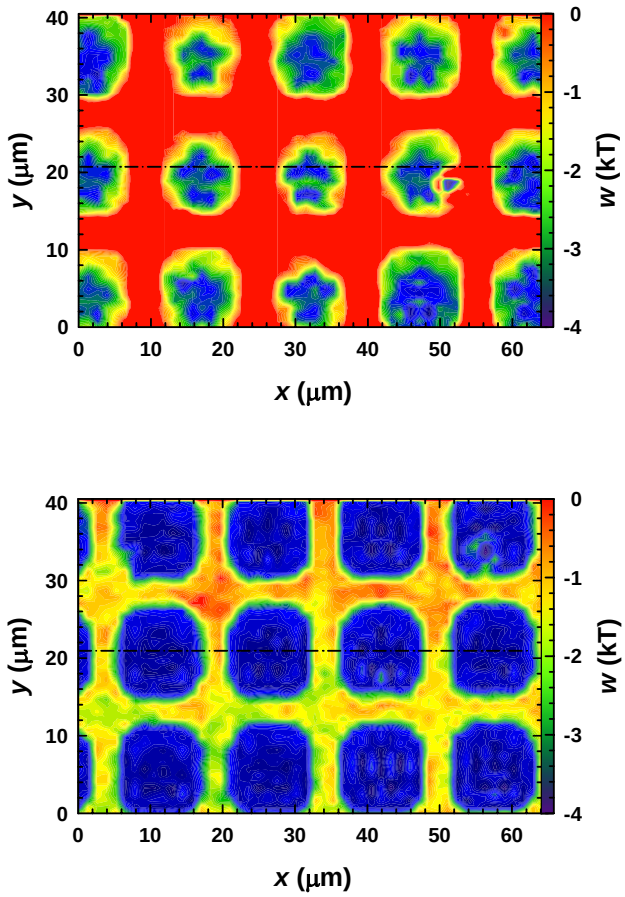

Figure 4.5. Free energy landscapes, $w(x, y)$, obtained from a Boltzmann inversion of $\rho(x, y)$ for the (**A**) low and (**B**) high concentrations in Figs. 4.3 A, B.

falling into nearby depleted features.

To obtain accounts for multi-particle packing effects in the analysis of DCP measured $\rho(x, y)$ (Figs. 4.3), we have developed a 2D IMC simulation method. The IMC algorithm employs iterative forward canonical MC simulations[24] with different

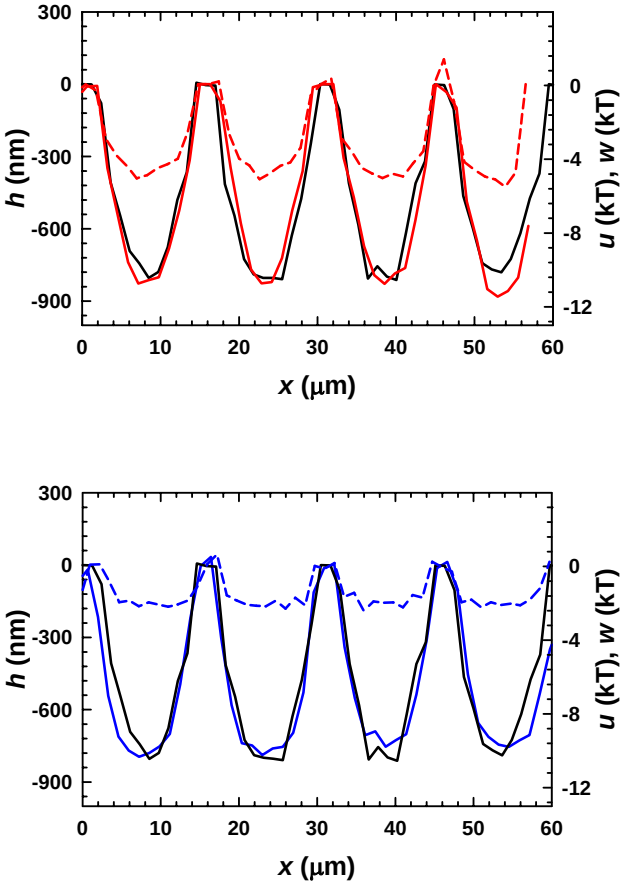

Figure 4.6. Energy landscape cross sections from (**A**) Figs. 4.1 B (solid black), 4.5 A (dashed red), 4.7 A (solid red) and (**B**) Figs. 4.1 B (solid black), 4.5 B (dashed blue), 4.7 B (solid blue).

guesses for $u(x, y)$ until a simulated $\rho_S(x, y)$ is obtained in agreement with a measured $\rho(x, y)$. MC simulations were performed using (1) the AFM pixel size in Fig. 4.1 B, (2) the ρ_{avg} in Figs. 4.2 A. B, (3) the measured pair potential,[57] and (4) $w(x, y)$ as an initial guess ($u(x, y)_0$=-ln[$\rho(x, y)$]).

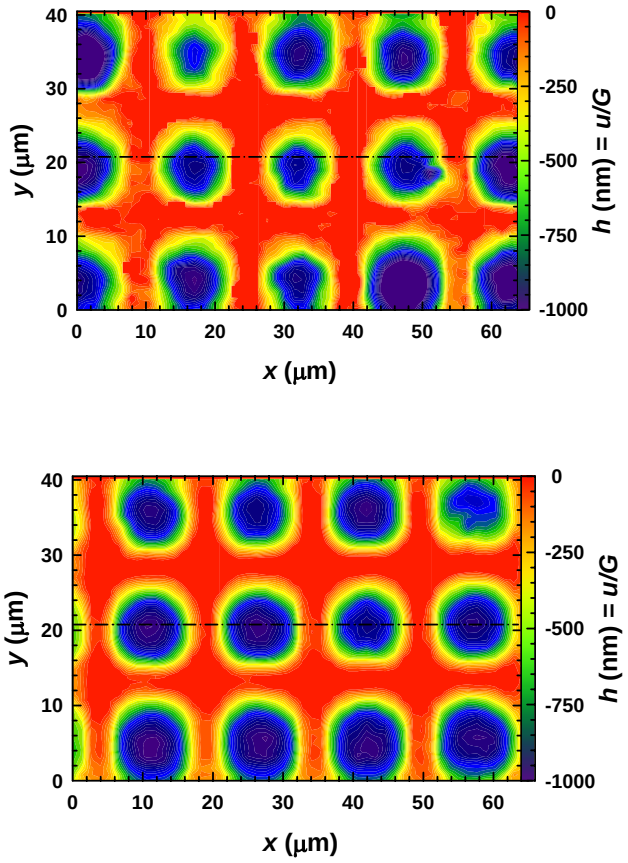

Figure 4.7. Potential energy landscapes, $u(x, y)$, and topographical surfaces, $h(x, y)$, obtained using the IMC algorithm and $\rho(x, y)$ for the (**top**) low and (**bottom**) high concentrations in Figs. 4.3 A, B.

To ensure rapid convergence to a unique solution, an algorithm was used to generate updated guesses for $u(x, y)_{i+1}$ after each iteration using,

$$u(x,y)_{i+1} = u(x,y)_i + 0.5\left[\rho_s(x,y)_i / \rho(x,y) - 1\right] \tag{4.2}$$

until the root-mean-square (rms) error, χ, was minimized using,

$$\chi = (XY)^{-1} \sum \left[\left(\rho_s (x,y)_i - \rho (x,y) \right)^2 \right]^{0.5} \tag{4.3}$$

Upon convergence, $u(x, y)$ were transformed to $h(x, y)$ (Figs. 4.7 A, B) based on their simple proportional dependence given by Eq (4.1). Convergence was achieved in ~24 and ~10 hours in the low and high concentration cases on a single computer processor.

The resulting DCP generated topographical surfaces (Figs. 4.7 A, B) are remarkably similar to the AFM measured surface in Fig. 4.1 B. After aligning the DCP and AFM generated $h(x, y)$ via a rms minimization (as a sort of pattern recognition algorithm), global differences between measured $h(x, y)$ are characterized by rms errors of 63nm and 45nm in the low and high concentration cases. Such differences can be attributed to optical limitations,[58] geometric issues (e.g. probe radius, quasi-2D assumption), and non-uniformities (e.g. polydispersity,[59] charge heterogeneity). In any case, the rms errors are 5-8% of the ~800nm feature depth indicating the relatively good accuracy of the DCP measured $h(x, y)$ (Figs. 4.7 A, B) compared to the AFM measured surface topography (Fig. 4.1 B).

4.4.3 Concentrated diffusing colloidal probe dynamics on energy landscapes

As part of understanding the dynamic imaging process (and template directed self-assembly kinetics), the energy landscapes in Figs. 4.5, 4.6 and 4.7 can be quantitatively linked to DCP self-diffusion and density fluctuations on the patterned surface. DCP trajectories from the low and high concentration experiments (Figs. 4.2 A, B) are only shown for a portion of the total observation time in Figs. 4.8 A, B to allow for visualization of the underlying pattern, although the less confined colloids in the

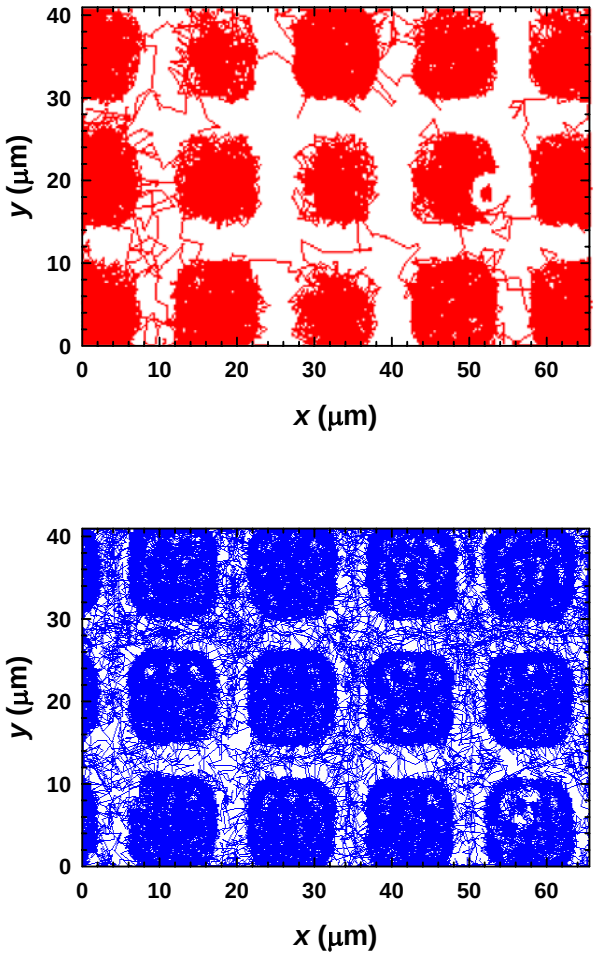

Figure 4.8. DCP trajectories for the (**A**) low (red) and (**B**) high (blue) concentrations in Figs. 1E, F over 35 min.

higher concentration case sample the window to a greater extent during this period. A single temporarily deposited colloid in Fig. 4.8 A (x≈52μm, y≈22μm) probably results from either colloid or surface non-uniformities but produces minimal net effect on the final inverted energy landscapes Figs. 4.5 A, 4.6 A and 4.7 A.

Analysis of mean square displacements (MSD) reveals the combined effects of

multi-body hydrodynamic interactions and free energy landscapes on self-diffusion (Fig. 4.9). Short-time self-diffusivities, D_S^S, are about half the Stokes-Einstein value ($D_0=kT/6\pi\mu a$) due to multi-body hydrodynamic interactions.[60] D_S^S is smaller in the higher concentration case due to the greater number of nearby colloids within the pattern features (Fig. 4.2 B). Long-time self-diffusivities, D_S^L, are much smaller in both cases than both D_0 and D_S^S as DCP must jostle past neighbours via cooperative multi-particle configurational rearrangement processes[61] and escape from crowded free energy wells.

The greater D_S^L in the high concentration case is qualitatively different from the monotonically decreasing trend expected for homogeneous, repulsive colloidal fluids. In the long-time limit, the tendency for colloids to more frequently escape pattern features and more slowly move past nearby particles at higher concentrations can be modelled as parallel resistive mechanisms using,

$$D_S^L = D_S^S \left[\exp\left(\Delta w/kT\right) + 2\phi g\left(2a_{eff}\right) \right]^{-1} \tag{4.4}$$

where D_S^S captures the role of multi-body hydrodynamic interactions, $exp(\Delta w/kT)$ accounts for free energy changes associated with escaping pattern features against gravitational forces normal to the surface,[62] and $2\phi g(2a_{\text{eff}})$ accounts for particles moving through their coordination shell within the quasi-2D fluid parallel to the surface.[61] By using $\Delta w=5kT$ and $\Delta w=2kT$ directly from measured $w(x, y)$ (Figs. 4.5, 4.6) and computing $g(2a_{\text{eff}})$ for effective hard disks using,[63]

$$g\left(2a_{eff}\right) = \left(1 - 0.436\phi_{eff}\right)\left(1 - \phi_{eff}\right)^{-2} \tag{4.5}$$

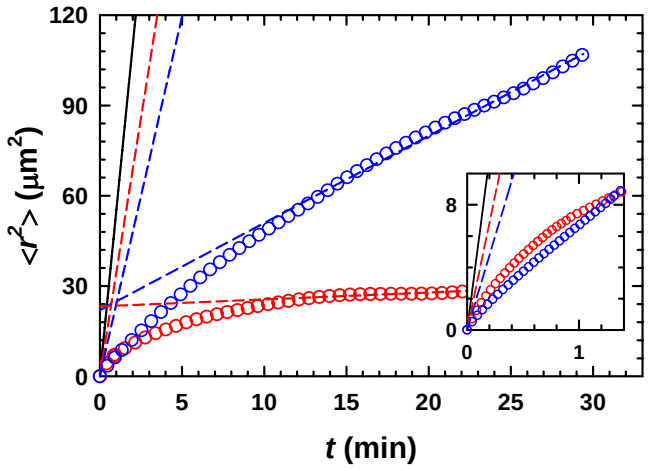

Figure 4.9. 1D mean square displacements, $\langle r^2 \rangle$, vs. time, t, (circles) averaged over x and y directions and multiple time origins with short-time (inset) and long-time (main) plots. Dashed lines show predicted Stokes-Einstein diffusion (black), curve-fits to short-time diffusion data, and predicted long-time diffusion using Eq (4.4)

the expression in Eq (4.4) accurately describes the long-time MSD data (Fig. 4.9). The expression for D_S^L is also accurate for limiting cases including infinite dilution on patterned surfaces and all sub-monolayer fluid concentrations on homogeneous surfaces.[60]

As a result, self-diffusion of DCP over pattern features (Figs. 4.8, 4.9) are consistent with the "imaged" $w(x, y)$ (Figs. 4.5 A, B) in terms of the Δw associated with escaping pattern features in the presence of multi-particle packing effects (Fig. 4.4). The concentration dependence of D_S^L via Δw also indicates that infinitely dilute DCP will

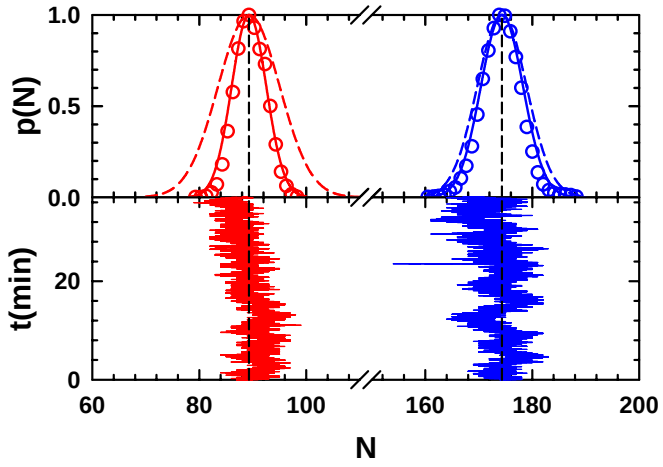

Figure 4.10. Measured number fluctuations, N, vs. time, t, (bottom) and histograms (top, circles) with GCMC simulated fluctuations on measured $u(x, y)$ (Figs. 4.7 A, B) (top, solid) and on homogeneous surfaces (top, dashed).

take orders of magnitude longer to image the surface due to an exponentially slower escape rate from $12kT$ potential energy wells compared to $2kT$ or $5kT$ free energy wells (Figs. 4.6 A, B). Although it may appear desirable to use a single DCP to image $u(x, y)$ since multi-particle packing effects are unimportant in the analysis, the observation time required for a single DCP to statistically sample an entire landscape is prohibitively long.

DCP dynamics were also characterized by comparing measured density fluctuations with 2D grand canonical Monte Carlo (GCMC) simulations[24] using the measured $u(x, y)$ (Fig. 4.10). Although our IMC algorithm uses a canonical ensemble based on its simplicity and minimal system size and ensemble related errors ($O(1/N)$ in

$\rho_S(x, y)$), GCMC simulations are required to accurately capture fluctuations in the finite, open systems investigated here (Figs. 4.2 A, B).[64] The measured and simulated density fluctuations are in excellent agreement in the low (σ_{exp}=2.8, σ_{sim}=3.2) and high (σ_{exp}=3.5, σ_{sim}=4.0) concentration cases. As expected, the measured inhomogeneous 2D fluid fluctuations are also less than GCMC simulated fluctuations in homogeneous 2D fluids with the same average concentrations (σ_{sim}=5.8 and σ_{sim}=4.6 in the low and high concentration cases). Excellent agreement between GCMC simulated fluctuations on the inverted $u(x, y)$ and direct measurements (Fig. 4.10) further demonstrates a consistent analysis of how energy landscapes modulate DCP dynamics.

4.5. Conclusions

Our results demonstrate the ability to analyze DCP on energy landscapes as a new surface imaging paradigm, which provides essential information to design, control, and optimize colloidal self-assembly on patterns. We have connected the equilibrium properties of quasi-2D inhomogeneous fluids of DCP at different concentrations to a patterned surface topography via direct measurements and analyses of free energy and potential energy landscapes. Our results also indicate connections between DCP dynamics and energetic pattern features, which is important to the temporal imaging process and to self-assembly kinetics.

Our findings suggest a number of extensions of the concepts introduced in this work. Diffusing probe imaging of *kT*-scale interactions could be adapted to access

various length scales using different sized probes (e.g. macromolecules, nanoparticles). Use of diffusing probes could also be generalized to interrogate diverse materials (e.g. biological, geochemical) and multi-dimensional problems using different probe tracking technologies (e.g. confocal microscopy). Because colloidal assembly on patterns is susceptible to dynamic arrest, analyses could also be implemented to detect and interpret non-equilibrium distributions of DCP on patterned surfaces. Finally, manipulation of colloids with external fields (e.g. electric, magnetic, optical) could allow them to be actively manipulated as "scanning" probes or passively monitored as "diffusing" probes to access a broader range of energy scales important to both driven- and self- assembly.

5. DIRECTED COLLOIDAL ASSEMBLY ON HOMOGENEOUS AND PATTERNED ELECTRODES

5.1. Synopsis

Assembly of colloidal particles into ordered structures near an electrode surface has been widely reported in the literature [12,65-69]. The lateral aggregation of colloidal particles has made the precise assembly of two and three dimensional colloidal crystals possible. In this section, we demonstrate the use of external electric fields to sensitively tune the interactions between colloidal particles to form ordered structures. The directed assembly of colloidal particles on patterned electrode surfaces is also investigated as a means of building three-dimensional nanostructures.

5.2. Introduction

The self-assembly of atoms and molecules is a continuous and spontaneous process in nature; for example the self-assembly of cells to form the lipid bilayer membrane. However, due to the larger size of colloidal particles and presence of hydrodynamic interactions and polydispersity in colloidal systems, their self-assembly into ordered structures is very challenging. Also, in the absence of any external forces, the colloidal particle motion is dominated by Brownian diffusion. Thermal energy (kT) is the characteristic energy associated with random thermal motion of particles at a given temperature that opposes organized self-assembly and instead favors disorder. These interactions are non directional, lack specificity and are difficult to control.

Consequently, the assembly time-scales are too slow for use in practical technologies. It is therefore essential to use external fields to provide directionality to the assembly process and thus facilitate faster colloidal assembly.

The arrangement of colloidal particles in a crystalline array has a variety of potential applications. Immediate realizable avenues include production of photonic band-gap materials, biological and chemical sensors by functionalizing the surfaces of the colloidal particles, micro-chip reactors and high density storage devices. The assembly of colloidal crystals above a substrate can be achieved by dispersing monodisperse colloids into a solvent and then controlling, and sensitively tuning particle-particle and particle-wall interaction forces or entropic effects.

The particle-particle interactions can be governed by gravity, capillary forces, electric and magnetic fields. The assembly of colloidal particles into ordered structures (above a charged surface) by the application of an electric field was first reported by Richetti et al.[65]. More recently conducted experiments on electrophoretic deposition also confirmed the lateral transport of colloidal particles towards each other over very large distances (even greater than five particle diameters) to form highly ordered two-dimensional structures in the presence of a DC electric field [12,66,67]. When particles are driven by electric fields onto an electrodes surface (simple Coulombic interactions), long-range in-plane attractions strong enough to induce two-dimensional crystallization are developed. This phenomenon is unexpected from pure electrostatic considerations as we expect like-charged particles to repel each other. Consequently, the attractive interaction between particles must be strong enough to overcome electrostatic repulsion

to facilitate the assembly. This lateral motion of colloidal particles towards each other stems from electrohydrodynamic [12,67] or electroosmotic [70-72] effects.

In this work, we use external AC/DC electric fields, to enhance the rate and manipulate the kinetics of interfacial colloidal assembly. The foundation of this approach is to use electric fields in conjunction with gravitational effects (patterned electrodes) to control inherent competitive transport mechanisms to produce ordered colloidal structures. The response of colloidal particle motion to external electric fields and the effects of electric field strength, AC frequency and electrolyte on interfacial colloidal assembly were investigated. We also measure pseudo-potentials between colloidal particles and the electrodes that capture the effects of the applied electric field using optical microscopy techniques

5.3. Experimental Section

Nominal 3 μm silica colloids were purchased from Bangs Laboratories (Fishers, IN), and the Polystyrene microspheres (4 μm and 4.9 μm) were purchased from Interfacial Dynamics Corporation (Portland, OR) and used without further purification. The manufacturer reported particle density is ρ_{SiO2}=1.96 g/ml, and ρ_{PS}=1.05 g/ml. All the particles used in this work were negatively charged. In each experiment, particles were diluted in 0.15 mM $NaHCO_3$ or KOH made with double deionized water to obtain bulk particle concentrations that produced desired interfacial concentrations after sedimentation equilibrium was attained.

Optically transparent Indium-Tin-Oxide (ITO) electrodes were supplied by Delta

Technologies and consisted of a 150nm thick layer of ITO deposited on a 1.1 mm thick glass slide. The sheet resistance was reported by the manufacturer to be 10 Ω per square. These electrodes were used in all experiments reported in this work. The electrode surfaces were cleaned thoroughly in 200% proof ethyl alcohol before use. A 2mm thick polydimethylsiloxane (PDMS, DC 184, Dow Corning) spacer was used to produce a small sedimentation batch cell. To prevent evaporation during the course of experiments, cells were sealed using water insoluble vacuum grease.

An optical microscope (Axioplan 2, Zeiss, Germany) and CCD camera were used to dynamically track and monitor particle trajectories of ensembles of levitated colloidal particles above the electrode surface. Visualization of the self and directed assembly processes on homogenous and patterned electrode surfaces were carried out using a 40X objective (NA=0.65) used in conjunction with a 12 bit CCD camera (ORCA-ER, Hamamatsu, Japan) operated with 4x binning to produce a capture rate of 28 frames/sec with 336x256 resolution (pixel size=607nm).

In each experiment, the sedimentation cell was first filled with the ionic solution containing colloidal particles at the desired concentration and then sealed with vacuum grease. External electric fields were applied only after the colloidal particles sedimented onto a two-dimensional plane above the electrode surface where they stay confined by gravity. The sedimentation time is a strong function of the particle concentration; at the same particle concentration, PS particles settle slower than the silica colloids because of the difference in specific gravities.

5.4. Results and Discussion

5.4.1 Colloidal assembly on homogenous electrodes – DC fields

In this section, we discuss colloidal particle assembly on homogeneous electrodes under steady DC fields. Figure 5.1a shows a schematic of the experimental set up used. The ITO electrodes were separated by a 2 mm thick insulating PDMS spacer and the cavity was filled with the colloidal dispersion. Electrical connections to the electrode were made using conductive silver epoxy.

The colloidal suspension of 4.9-micron PS particles in 0.15 mM KOH solution was introduced between the electrode surfaces and video microscopy was used to track the motion of particles. In the absence of external electric fields, the colloidal particles are randomly distributed and undergo Brownian excursions above the electrode surface (Fig. 5.1b). At low field strengths, the colloidal particles were seen to move towards one another across the electrode surface, to form metastable crystalline structures (Fig. 5.1c). The particles diffuse away, breaking up the crystalline structure, when the field is turned off or when the polarity is reversed (Fig. 5.1d). The metastable colloidal structure can then be fixated onto the substrate by applying a high voltage, and the ionic solution can be removed without disturbing the deposited layer[66]. This is consistent with the observations made by Bohmer [66] and Trau et al. [67]. As the particles and clusters were seen to interact over long ranges, Bohmer [66] suggested hydrodynamic effects resulting from electrokinetic flow around each particle were responsible for particle aggregation..

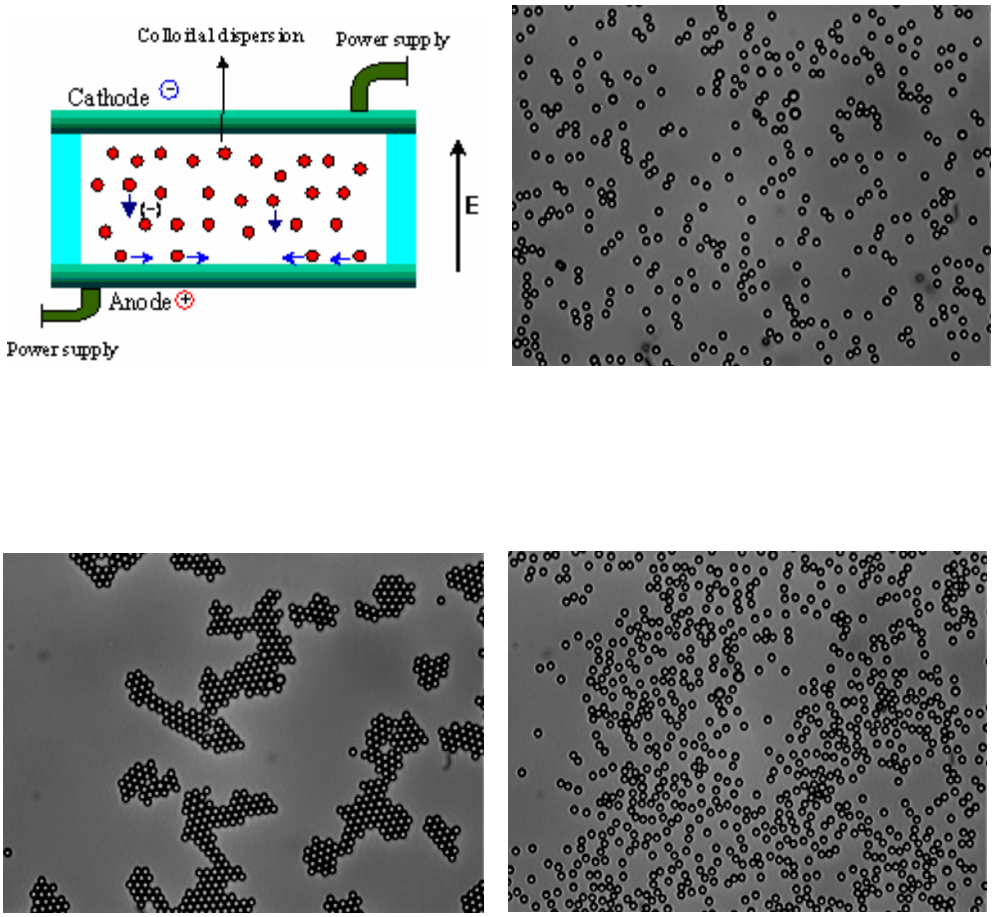

Figure 5.1. (a) Schematic of the experimental set-up. Lateral aggregation of 4.9 μm PS particles in 0.15 mM KOH in response to a 0.16 V/mm DC field (b) t=0 sec, (c) t=240 sec, (d) colloidal clusters breaking up, t=60 sec after field is turned off

This also ruled out the contribution of short ranged colloidal forces to particle aggregation. As described by Solomentsev et al.[71], the motion of particles above an electrode surface is governed by the relative interplay of electrokinetics, electrohydrodynamics and Brownian diffusion, with Brownian diffusion tending to randomize the distribution [71].

The use of DC fields also limits the maximum voltage that can be used during the assembly process: strong electrochemical reactions occur at the electrode surfaces at higher voltages. It is important to maintain the pH of the ionic solution during the course of the experiment as well. The electrochemical reactions at the electrode surfaces may result in pH fluctuations during the experiment. Also, as the surface charge on the ITO surface is a function of the pH (zeta potential~-60 mV at pH > 10, ~-20 mV at pH = 8-9), it is recommended that the pH of the ionic solution be maintained at around 10 to observe particle aggregation in the time scales reported in Fig. 5.1.

5.4.2 Colloidal assembly on homogenous electrodes – AC fields

The behavior of colloidal particles in AC electric fields is more interesting. Although DC fields can produce 2D colloidal crystals, AC fields will be used to (1) avoid electrochemical reactions, (2) enhance the rate of colloidal particle crystallization (ordering), (3) produce effective repulsion and attraction for different frequencies and electrolytes[72], and (4) anneal via oscillatory forces. At low field strengths that do no produce dipolar interactions, AC electrophoretic deposition has been shown to form metastable 2D crystals at electrode surfaces (Fig 5.2c) as the result of electrohydrodynamic flows [71-74] which are ideal precursors for nucleating and growing

interfacial colloidal crystals. It is important to note that the interaction potential between particles used in these experiments is purely repulsive; as a consequence, the colloidal crystal melts and loses order when the external electric field is turned off.

The effective interactions between the particles can be tuned from attraction to repulsion by varying the frequency of the AC electric field. At very high frequencies (ω > 1 kHz), the colloidal particles are essentially Brownian as the particle does not have time to respond to the fast changing electric field; interactions between the particles are repulsive, and no ordered structures are formed. At lower frequencies, the colloidal particle motion was deterministic and a strong function of the amplitude of the applied AC field; interactions between the particles are attractive resulting in the formation of ordered colloidal structures (Fig 5.2c) from the random configuration in Fig. 5.2b.

In addition to the amplitude and operating frequency of the electric field, we found that the choice of the electrolyte influenced the nature of particle-particle interactions. In contrast to the attraction seen between PS particles in 0.15 mM KOH in dc fields (Fig. 5.1), lateral repulsion is observed at all frequencies in AC electric fields (Fig. 5.2d). The inter-particle spacing in the colloidal array shown in Fig. 5.2d is almost uniform. This is contrary to the observations of Nadal et al. [68], where lateral aggregation of particles is seen at 100 Hz in 0.1 mM NaOH (see Fagan et al. [72] for more details). However, assembly of colloidal particles is found in the case of PS particles in 0.15 mM sodium bicarbonate ($NaHCO_3$) (Fig. 5.2c). Also, the crystalline structures formed faster in AC fields when compared to DC fields. The strength of electric field, time of application of the electric field and the electrolyte are all controllable parameters that can

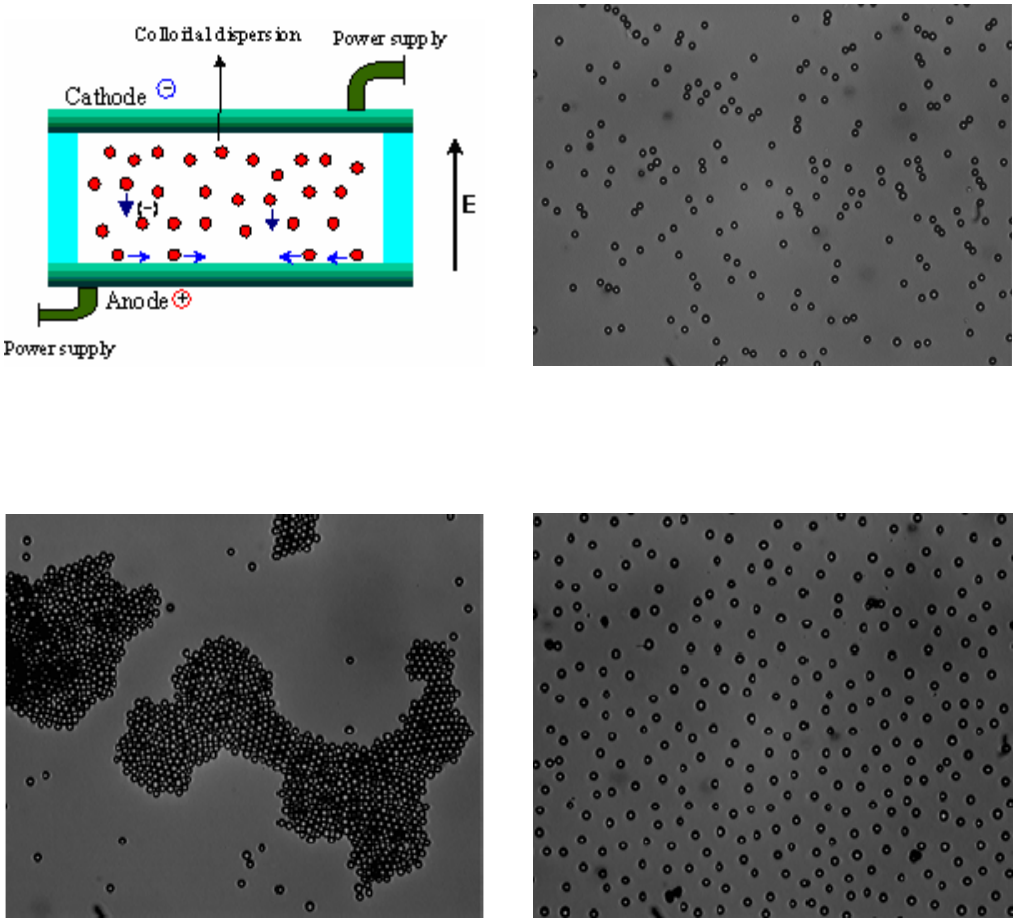

Figure 5.2. (a) Schematic of the experimental set-up. Response of 4 μm PS particles to external AC electric fields (b) random colloidal configuration at t=0 sec, (c) attractive crystals for 30V/cm-30Hz AC in $NaHCO_3$, and (d) repulsive ordered fluid for 30V/cm-100Hz AC in KOH.

be used to tune colloidal particle interactions to make desired structures of colloidal arrays.

With a change in electrolyte from $NaHCO_3$ to KOH, an opposite behavior was observed in the equilibrium elevation (height above the electrode) of the particle in a recent study [72]. In KOH, the net flow is downward over the particle (pushing it closer to the electrode) and the streamlines extend outward close to the electrode surface. Entrainment in this outward flow would cause neighboring particles close to the electrode surface to move away from each other [72]. In $NaHCO_3$, the direction of the streamlines are reversed, causing the particle to be pushed away from the electrode and consequently the neighboring particles aggregate together.

We also measured the particle-wall effective potentials in the presence of AC electric fields using the ETIRM technique described in Section 2 and 3. Figure 5.3 shows the ensemble averaged particle-wall pseudo-potential energy profiles between 4.9 μm polystyrene (PS) particles suspended in a 0.15 mM $NaHCO_3$ ionic solution, and an Indium-Tin-Oxide (ITO) electrode surface. In the absence of electric fields, the nature of interaction between the PS particles and the ITO surface is purely repulsive (Fig. 5.3). In Fig. 5.3a, we fix the frequency of the AC electric field at ω=800 Hz, and increase the amplitude of the AC signal (sine wave). The interaction potential changes from pure repulsion in the absence of electric field to increasing amounts of attraction as the amplitude of the electric field is increased. A similar trend was observed when the amplitude was held constant and the frequency was increased to ω=100 Hz, as shown in Fig. 5.3b. Note that the potential energy profiles in Fig. 5.3 are plotted without the

gravitational potential. These results are included here to demonstrate that tunable long-range interactions exist between colloidal particles and surfaces under the influence of AC fields. These effective or pseudo potentials can be sensitively measured using the ETIRM technique. For a more extensive set of single-particle TIRM measurements on a similar system, the reader is referred to Fagan et al.[72]. These ensemble measurements of particle-surface interactions are critical to understanding of how various interfacial structures are formed in concentrated systems as a function of electric field amplitude and frequency.[72,75]

We have demonstrated that interfacial electro-hydrodynamic flows around charged colloids near homogeneous electrodes (transparent ITO)[71] can be used to form crystallites from quasi 2D colloidal fluids (Figs. 5.1, 5.2). Crystallites form as the result of a balance of conservative forces due to particle, surface, and gravitational potentials and dissipative forces due to electro-hydrodynamic flows. Because the crystallites in Fig 5.2 reach a pseudo equilibrium structure, 2D inverse MC analyses (originally designed to analyze equilibrium fluids) can be used to determine effective pseudo potentials[74] between particles from ETIRM/VM measured distribution functions. These effective-pseudo potentials will help to understand how conservative and dissipative forces contribute to AC electric field mediated interfacial assembly processes. Although the single particle work[72] has suggested important microscopic mechanisms, it has not yet been directly connected to the processes involved with forming macroscopic 3D interfacial crystals. Inverse MC simulations are required since inverse analyses based on

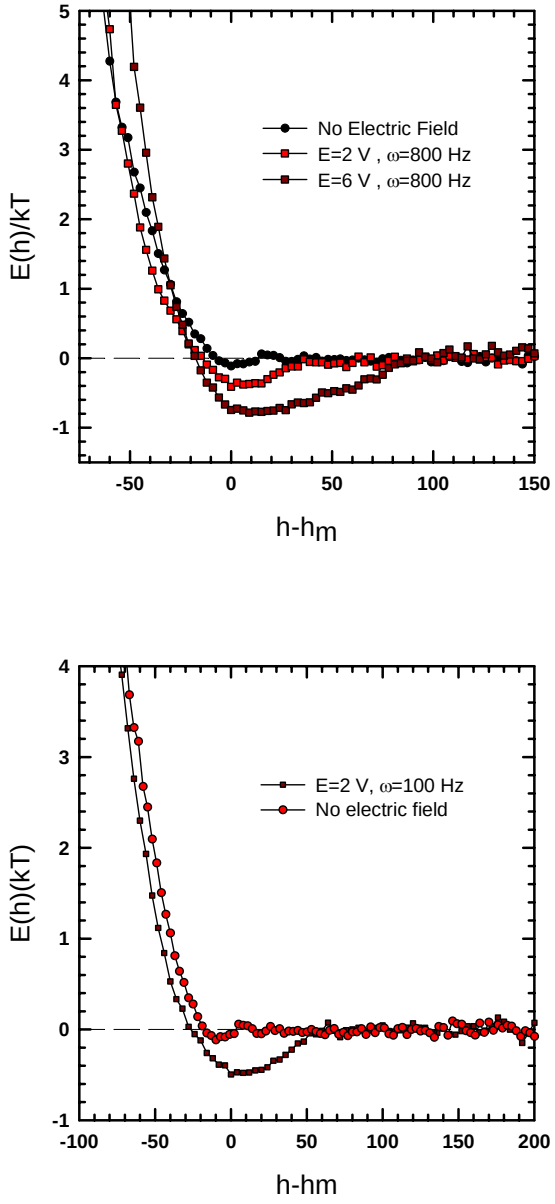

Figure 5.3. Effective particle-wall interactions between 4.9 μm polystyrene particles and an Indium-Tin oxide electrode (a) 0.15 mM $NaHCO_3$, frequency of AC electric field held constant at ω=800 *Hz*, while field amplitude is increased, (b) 0.15 mM $NaHCO_3$, amplitude of AC field is held constant at 2 V peak to peak, ω=100 *Hz*. The effective particle-wall potential changes from pure repulsion in the absence of electric field to attraction when field is turned on. The amount of attraction can be tuned by varying the frequency and amplitude of the electric field.

liquid structure theory is not amenable to the study of crystal structures. This is part of on-going work and the results from this effort are not included in this dissertation.

5.4.3 Self and directed assembly on patterned electrodes

Standard photolithography techniques described in Section 3 were used to fabricate arrays of different size physical features on an Indium-Tin-Oxide (ITO) electrode surface. The pattern comprised of alternating regions of conductive (ITO) and dielectric (photoresist) surfaces. In preliminary experiments, we studied the self-assembly and packing of colloidal particles in features of varying sizes in the absence of external fields. Because gravity is a steady field that cannot be avoided (on earth), the foundation of this approach is based on properly considering the role of sedimentation in interfacial assembly processes.[76,77] With this understanding, the primary goal is to use AC electric fields in conjunction with gravitational effects and patterned electrodes to control competitive transport mechanisms either before or after thermodynamic assembly processes are initiated.

The particles sediment onto the templated substrate and the resulting equilibrium colloidal configuration is a direct consequence of the particle-wall and particle-particle interactions. Figure 5.4a shows an optical micrograph of 3 μm silica particles confined in an array of 5 micron features. The particles are still Brownian and sample the gravitational potential energy surface landscape as explained in Section 4. The colloids were seen to pack in a similar fashion in other size features, subject to geometric constraints. Again, the time scales associated with the self assembly process to reach equilibrium colloidal configurations is slow.

Next, we studied the use of external AC electric fields to guide the assembly of colloidal particles on patterned electrodes. The colloidal suspension of 3 μm silica particles in 0.1 mM $NaHCO_3$ solution was introduced between the two ITO electrode surfaces (anode: templated ITO, cathode: plain ITO surface), separated by a 2 mm PDMS spacer. The features on the electrode create a current density gradient on the electrode surface and draw the colloidal particles into the features. The inhomogenous electrode distorts the electric field lines and facilitates faster colloidal assembly inside the patterns. Cycling the frequency of the AC electric field was found to be an effective way to anneal equilibrium thermodynamic configurations. Once a closed pack colloidal configuration is formed in two dimensions, it is possible to grow structures in three-dimensions by using it as a template.

This last approach is distinctly different from the thermodynamic approaches used for homogeneous and patterned surfaces and provides an alternative or complementary method to modulate reversible interfacial crystallization. Collectively, these results demonstrate how synergistic approaches using energy landscapes and electric fields together might be used to control interfacial crystallization of colloidal particles. A general consideration to optimally couple self- and directed- assembly methods is that the magnitudes of transport rates and driving forces associated with directed-assembly not exceed those associated with self-assembly (or external forces will destroy self-assembled structures).

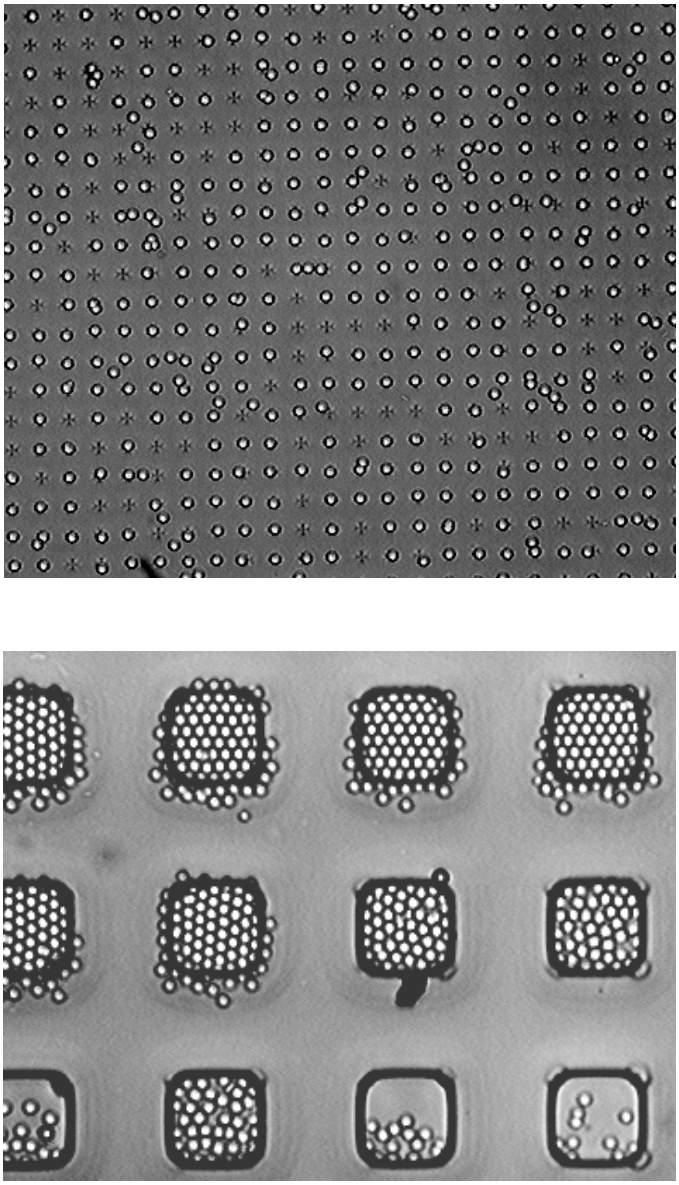

Figure 5.4. (top) 3 μm silica colloids in an array of 5 micron features in the absence of external fields (b) crystallite precursors formed on a patterned ITO electrode surface when a 5 Vpp, 30 Hz AC field is applied. The size of the patterned features was 25x25 μm.

5.5. Conclusions

In this work, we have demonstrated the use of external electric fields to tune the interactions between the colloidal particles and control its assembly. The nature of the colloidal interactions was found to be sensitive to the strength, frequency of the AC field and the electrolyte used. Cycling the AC field frequencies was found to be an effective way to anneal equilibrium colloidal configurations. We also observed the preferential assembly of colloidal particles in gravitational energy landscape features made on the electrode surface when an AC field was applied. The results from this work suggest a general strategy to integrate self- and directed- assembly methods to successfully navigate free energy landscapes as a means to control nano- and micro- particle structure formation.

6. COLLOIDAL STRUCTURE, TRANSPORT, AND IMPEDANCE PROPERTIES BETWEEN INTERFACIAL MICROELECTRODES

6.1. Synopsis

We report *in situ* measurements of the reversible, directed assembly of colloidal gold microstructures and their associated impedance properties on surfaces between planar gold film microelectrodes. Video optical microscopy is used to monitor formation of locally concentrated configurations with variable capacitances as well as the assembly of wires with variable resistances. A scaling analysis of dominant electrokinetic transport mechanisms at different electric field amplitudes and frequencies is consistent with the observed steady-state microstructures. Finally, impedance spectra are fit to equivalent circuits with elements directly connected to physical characteristics of the micro- electronic/fluidic device components and different particle microstructures.

6.2. Introduction

Numerous studies have investigated colloidal dispersions in electric fields as a means to characterize particle size and surface charge,[78] create electrorheological fluids,[79] separate biocolloids[80] and carbon nanotubes,[81] control display devices,[82] understand fundamental phase behavior,[83] and assemble irreversible nanowires.[84] Such studies are often restricted to a range of applied field voltages and frequencies dictated by the dominance of a particular transport mechanism in a specific application. For

example, studies of the dielectrophoretic assembly of metal colloids into nanowires are naturally limited to high fields where dipolar chain formation occurs.[84] In contrast, studies aimed at characterizing particle properties via their electrophoretic transport are necessarily performed at low fields.[78] However, intermediate to these limiting regimes, a comprehensive description of the connections between microstructural transitions, transport mechanisms, and AC electrical properties is lacking, particularly in the case of interfacial and confined geometries important to integrated micro- fluidic/electronic devices.

In this work, we use *in situ* optical microscopy and impedance measurements to systematically measure microstructures and AC electrical properties of metal nanoparticles between planar gold electrodes over a broad range of applied electric field amplitudes and frequency. Specifically, we demonstrate the ability to change the impedance characteristics in a microelectronic device via electric field mediated assembly of different nanoparticle microstructures. In addition, the reversible nature of such colloidal based devices are shown to exhibit unique impedance responses, tunability, and scalability not easily obtained from existing solid-state materials or microelectromechanical system based devices. From a more fundamental perspective, we gain new insights into the connections between microstructure, transport mechanisms, and impedance properties that provide essential information to intelligently design and control nanoparticle based integrated micro- fluidic and electronic devices.

6.3. Experimental Section

The experimental arrangement (Fig 6.1) consists of nominal 800 nm diameter gold colloids (Alfa Aesar) levitated by electrostatic repulsion above lithographically patterned gold electrodes on microscope slides.[85] The patterned gold electrodes have a uniform thickness of 50nm and an interdigitated configuration with lateral spacing of 30μm and a finger width of 500μm. Gold nanoparticles were dispersed in aqueous 0.1 mM $NaHCO_3$ and confined within a small volume (1mm high x 5mm diameter) on the patterned electrode surface by a polydimethylsiloxane batch cell.

A function generator (Agilent 33120A) and impedance analyzer (Hewlett-Packard HP4194A) were connected in series to the interdigitated electrodes to simultaneously tune nanoparticle assembly and acquire the raw impedance magnitude, $|Z|$, and phase angle, δ. The impedance analyzer was tested and calibrated using an open/short circuit compensation routine recommended by the manufacturer and was interfaced to a laboratory PC using a LAB-VIEW 8.0 program (National Instruments). All the impedance measurements were made at a nominal oscillator voltage level of 0.25 V. The precision of the analyzer was checked with standard 10Ω, 100Ω resistances and a standard 30μF capacitor, and in all cases was better than 1%. Lead inductance effects were minimized by placing the cell assembly on an optical table close to the impedance analyzer. CCD camera (Hamamatsu) images of steady state colloidal configurations in Fig 1 were obtained using an inverted microscope (Zeiss) with a 40X objective.

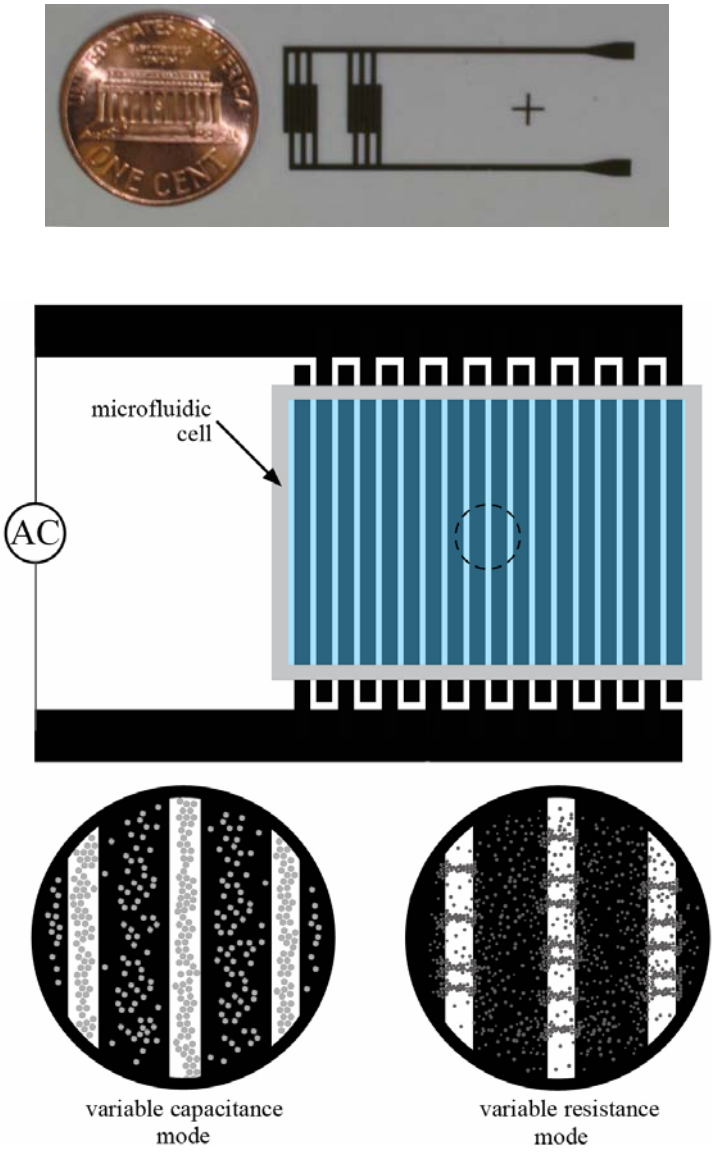

Figure 6.1. (a) Photograph of the interdigitating gold electrode patterned on a glass substrate using standard photolithography, (b) Schematic representation of the microfluidic cell used in experiments. The two "zoomed-in" views represent the phenomena of capacitive changes brought about by assembly within the center of the gap that varies the dielectric permittivity of the spanning fluid (left) and the variable resistance and switch behavior of metal particles assembling into wires that span the electrode gap in the presence of an AC field (right)

6.4. Results and Discussion

6.4.1 Manipulating nanoparticle microstructures using external AC fields

In the absence of any applied fields, the gold colloids are randomly distributed and diffuse laterally above the glass and electrode surfaces via Brownian motion. The colloids remain confined within a quasi-2D layer (~100nm) due to gravity and particle-surface electrostatic repulsion. In the presence of electric fields, Fig 6.2 shows a matrix of steady-state microstructures assembled in between and above a single electrode pair gap as a function of AC voltage (0.5-2.5V) and frequency (10Hz-1MHz). All colloidal microstructures in Fig. 6.2 were assembled in a completely reversible fashion as the result of ~100nm electrostatic repulsion (the Debye length is κ^{-1}=30nm) preventing intimate contact and irreversible adhesion between colloids and surfaces via van der Waals[40] and dipolar attraction.[86] This reversibility allows dynamic reconfigurability between all of the steady-state microstructures in Fig 6.2 by tuning the AC field amplitude and frequency, although the rate of dynamic transition depends on the initial and final configurations (e.g. wires form more quickly from random configurations than an empty gap).

The results in Fig. 6.2 can be organized based on three distinct steady-state microstructures that emerge based primarily upon AC field frequency regimes and a lesser dependence on AC field amplitude. For ω≈1-100Hz, colloids are concentrated and centrally oscillate within the electrode gap while tracking the AC field, whereas colloids above the electrodes experience lateral aggregation. For ω≈1-100kHz, colloids

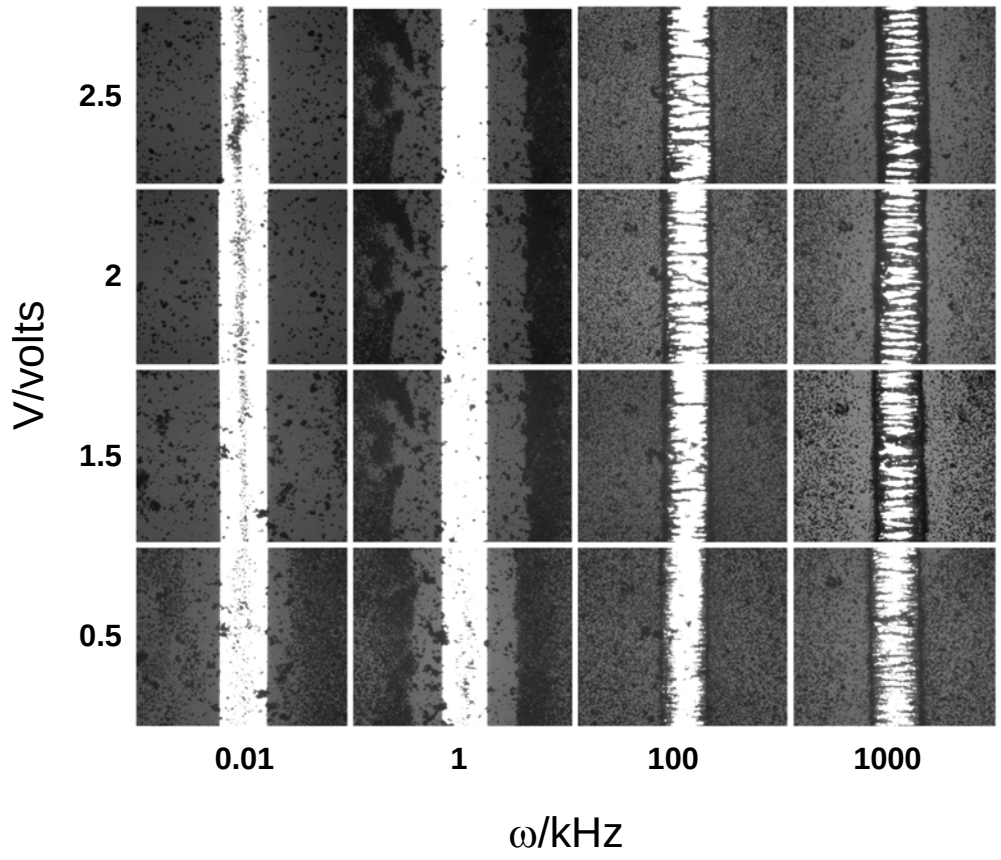

Figure 6.2. Equilibrium steady-state configurations of 800-nm gold colloidal particles at various electric field strengths and frequencies. At low forcing frequencies (1~100 Hz) quasi-steady electrophoretic response is observed, exhibiting increasing capacitance with increased field amplitude. At moderate forcing frequencies (~1 kHz) a 3-D flow is induced, which removes particles from the electrode gap. At higher frequencies, DP overwhelms colloidal motion, and the colloidal circuit exhibits variable resistor behavior. Colloidal response time to reach the 2.5 V, 1-MHz equilibrium condition from a randomly distributed Brownian configuration was under 4 seconds. All equilibrium configurations were reversible and repeatable.

are expelled from the electrode gap and concentrate on top of the electrodes with a depleted zone near the electrode edges (circulation visible during initial transient but not at steady-state). For ω>100kHz, colloids assemble into wires bridging the electrodes and align with the expected field lines in the gap. In addition, a systematic increase in the number of chains and their cross sections (or the degree of lateral chain bundling) is observed in Fig 6.2 with increasing AC field amplitude and frequency for the conditions investigated. For each of the three steady-state microstructures observed in Fig. 6.2, greater AC field amplitudes do not alter the microstructure type in each frequency regime but primarily enhance the assembly time-scale and the structural fidelity (e.g. particles become more concentrated within the gap for ω≈1-100Hz or laterally bundle into denser wires for ω >100kHz).

Figure 6.3 shows reversible Au nanowire network formation with DEP in non-uniform electric fields at 5 V peak-to-peak and 1 MHz. The non-uniform electric fields were induced by a pointed electrode next to a flat conducting surface in Fig. 6.3 a,b, and conducting islands between planar electrodes in Figs. 6.3 b,d. When the AC signal was changed to ω=10 Hz, the colloidal wires melt in Fig. 6.3 b, but shows an interesting response in Fig. 6.3 d, where a single looping colloidal wire connecting the intermediate gold bridges evolves from the configuration in Fig. 6.3 c in less than 30 seconds. This could potentially be useful in engineering colloidal configurations with anisotropic electrical properties. Further electrical property measurements are necessary to assess

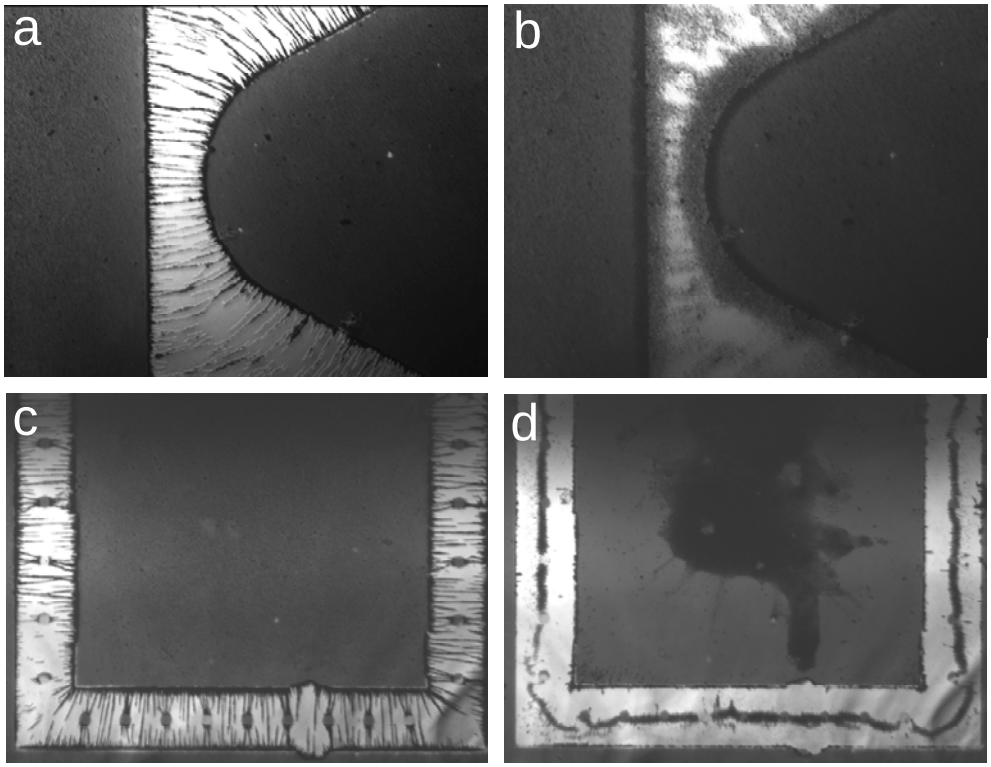

Figure 6.3. Reversible Au nanowire network formation with DEP in non-uniform electric fields (induced by a pointed electrode next to a planar conducting surface (a), and conducting islands between planar electrodes (c)) at 5 V peak-to-peak and 1 MHz . When the AC signal is changed to ω=10 Hz, the colloidal wires melt in (b), but shows an interesting response in (d) where a looping single wire connecting the intermediate gold bridges evolves from the configuration in (c).

the utility of non-uniform electric fields in improving the electrical properties otherwise obtained with uniform electric fields.

6.4.2 Dominant transport mechanisms

In the following, we present an analysis of colloidal particle dynamics and summarize the type of fluid flow observed in a simplified system consisting of two co-planar parallel gold electrode strips. The experimental results discussed in the previous sub-section are put in perspective using a general understanding of scaling laws governing this simple system. Preliminary scaling arguments presented here are intended to provide some intuition and predictive capabilities for the frequency and amplitude dependent behavior of colloidal microstructures and their associated electromagnetic properties, and within limits, can be extended to more complicated microelectrode shapes. In addition, these scaling arguments suggest opportunities (and limits) for tuning device characteristics over a broad range based on available colloidal fluid characteristics (e.g. particle size, shape, dielectric properties; fluid viscosity, dielectric properties; other parameters - temperature, micro-channel dimensions, etc.).

A schematic diagram of the microelectrode system used in this work with the electric field lines is shown in Fig. 6.4. As the spacing between the electrodes is small compared to the length and width of the electrodes, the system is essentially two-dimensional. This simplified set-up serves as an ideal test case to explore the relative magnitudes of different forces in play, and the validity of assumptions made in the

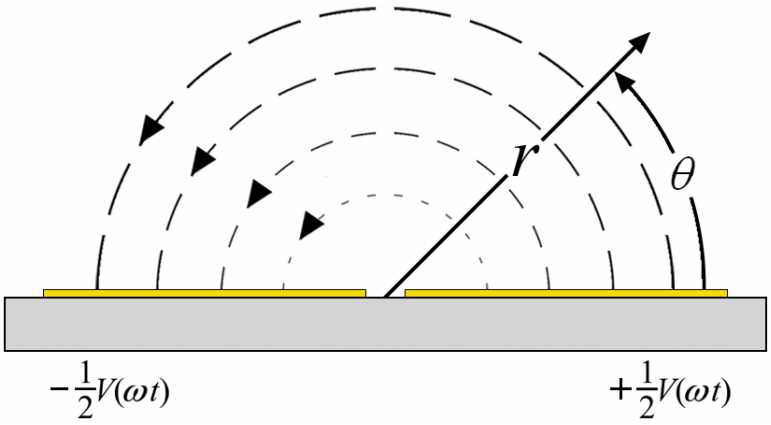

Figure 6.4. Schematic of a simplified co-planar gold electrode system showing the electric field lines. The electric field in this arrangement is a function of r and θ.

scaling analysis. This systematic study is potentially important as we try to extend the results to experimentally more complex electrode arrangements.

The steady-state structures in Figs 6.2 and 6.3 and their transient assembly can be explained in terms of a competition between sedimentation, self-diffusion, and several AC electric field mediated transport mechanisms including electrophoresis (EP), AC electro-osmosis (EO), and dielectrophoresis (DP).[87] In all cases, sedimentation concentrates particles onto the interdigitated electrode surface, and Brownian motion tends to produce laterally homogeneous, random configurations. To assemble the microstructures in Fig 6.2, AC electric field mediated colloidal transport must be comparable to, or exceed, the characteristic transport rates associated with sedimentation and self-diffusion (Peclet numbers greater than one).

To understand the relative contributions of these different transport mechanisms, Fig 6.5 indicates the magnitude of the dominant transport mechanism for the AC field voltage and frequency conditions investigated in Fig 6.2. Specifically, particle velocity due to EP, EO, and DP are computed using single-particle predictions,[87] and the maximum velocity (for the three competing mechanisms) is represented as a phase plot in Fig 6.5 to produce three distinct regimes. Other mechanisms such as transport due to Joule heating and electrothermal effects are considered to be negligible due to the relatively small fields used in this work. It is useful to realize that particle velocities are directly related to mobilities that are commonplace in electrokinetic transport, and consequently forces.

Understanding how each of these transport processes depend on relevant nanoparticle and device parameters provides a basis to design, control, and optimize the assembly of the microstructures observe in Figs 6.2 and 6.3. For the thin electrical double layers investigated in the present study ($\kappa a >> 1$), the single-particle, DC electrophoretic mobility is given by the Smoluchowski equation as,[88]

$$u_{EP} = \left(\varepsilon\zeta/\mu\right)\left(\pi r\right)^{-1} V \tag{6.1}$$

where ε is the medium permittivity, μ is the dynamic viscosity, ζ is the particle zeta potential, r is the electrode spacing, and V is the applied voltage (which is approximately related to the electric field as $E=V/\pi r$). For AC electric fields, the particle mobility is oscillatory and tracks the field with a frequency dependent phase lag until minimal net displacements occur above a threshold frequency. The maximum velocity associated

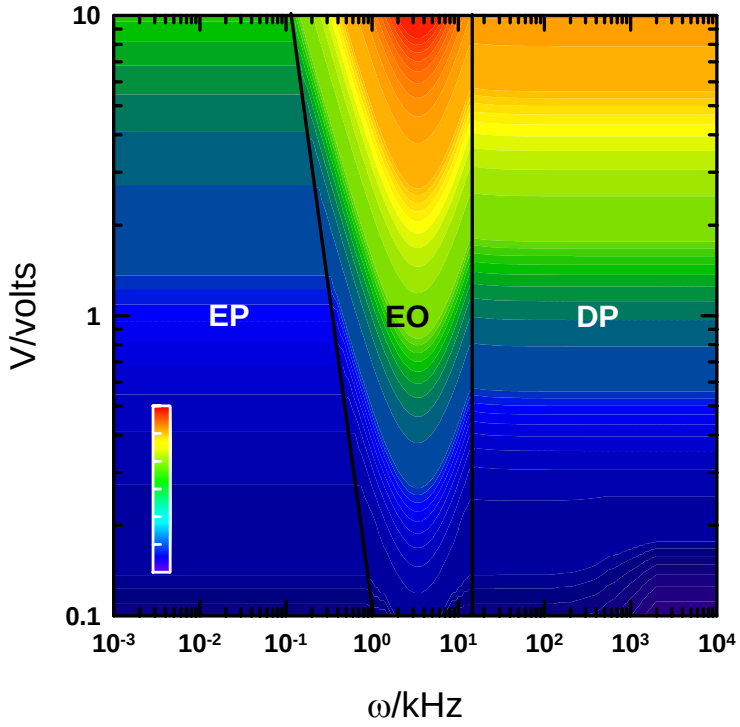

Figure 6.5. Voltage vs. frequency diagram indicating magnitudes of dominant transport mechanisms for single colloids in the coplanar electrode device shown in Fig 6.2. Quasi-steady electrophoresis (EP) is the dominant transport mechanism at low frequencies (ω<100 Hz), while AC electroosmosis (AC-EO) is active at moderate frequencies (100 Hz<ω<100 kHz) and dielectrophoresis dominates at higher frequencies (ω>100 kHz). Velocity contours are defined by the logarithmic spectrum scale shown in the inset with red=2000μm/s and violet=0.01μm/s.

with dynamic EP in the presence of external AC fields can be determined from the equation of motion for a charged particle to be,[89]

$$u_{EP} = \left(\alpha\varepsilon\zeta/\pi\mu mr\right)\left[\left(\alpha/m\right)^2 + \omega^2\right]^{-0.5} V \tag{6.2}$$

where ω is the applied field frequency, $m=\rho_p(4/3)\pi a^3$ is the mass of the colloidal particle and, $\alpha=6\pi\eta a$ is the friction factor of the particle in the fluid. The dynamic electrophoretic mobility is complex-valued and is expressed in terms of its modulus in Eq. (6.2). The argument of the complex mobility can be used to determine if the particle velocity lags behind or leads the applied electric field. It is important to note that inertial effects will become important when the characteristic momentum relaxation time scale, $\tau=\alpha/m$, is comparable to the frequency of the applied AC field. Interaction of the tangential electric field with exposed glass and gold electrode surfaces produces a characteristic fluid velocity due to AC EO, also corresponding to the transport rate of entrained particles as,[87]

$$u_{EO} = \left(\Lambda\varepsilon/8\mu r\right)\Omega^2\left(1+\Omega^2\right)^{-2} V^2 \tag{6.3}$$

where $\Lambda=C_S/(C_S+C_D)$, C_S is the Stern layer capacitance, C_D is the diffuse layer capacitance, $\Omega=(\Lambda\omega\varepsilon\kappa\pi r/2\sigma)$, and σ is the medium conductivity ($\Lambda\approx0.2$ for gold film electrodes with $C_D=\varepsilon\kappa$ and $C_S=0.007\text{F/m}^2$ as discussed in Ref. [87]). Dielectrophoretic nanoparticle transport arises from the interaction of electric fields with electric field induced particle dipoles with a characteristic rate given as,

$$u_{DP} = \left(a^2 \varepsilon / \pi^2 3\mu r^3\right) f_{CM} V^2 \Omega^2 \left(1+\Omega^2\right)^{-1} \tag{6.4}$$

where f_{CM}=Re[($\tilde{\varepsilon}_p$-$\tilde{\varepsilon}$)/($\tilde{\varepsilon}_p$+2$\tilde{\varepsilon}$)] is the real part of the Clausius-Mossotti factor (f_{CM}=1 for gold colloids as they are completely polarizable), $\tilde{\varepsilon}$ is the complex permittivity given as $\tilde{\varepsilon}$=ε-iσ/ω (subscript "p" refers to particle). In the presence of other particles, the induced dipoles interact not only with the external field but also with corresponding dipoles on neighboring particles. Using an expression for the chaining force between two adjacent conducting particles (that is more relevant to this experimental study), The rate of colloidal transport and assembly into wires via DP in non-uniform electric fields can be collectively characterized using,[90]

$$u_{DP} = \left(\varepsilon a^2 / \pi \alpha r^2\right) f_\phi f_{CM}^2 \Omega^2 \left(1+\Omega^2\right)^{-1} V^2 \tag{6.5}$$

where f_ϕ is a correction factor accounting for interparticle spacing, chain orientation, and effective medium dielectric properties at finite colloid concentrations (f_ϕ≈10 from Ref. [90]). The chaining force is always attractive, is proportion to the square of f_{CM} and, has a weaker dependence on particle size than the direct dielectrophoretic force. The factor $\Omega^2(1+\Omega^2)^{-1}$ appearing in Eqs. (6.4) and (6.5) takes into account the reduction of the voltage in the medium due to electrode polarization. At low frequencies (Ω≈1), polarization of the double layer significantly reduces the effective voltage present in the electrolyte. At higher frequencies, the surface charge accumulated in the double layer is negligible and the applied voltage is dropped mainly across the electrolyte.

Based on Eqs (6.1)-(6.5), Fig 6.5 reports the magnitude of the dominant transport mechanisms for the AC amplitudes and frequencies investigated in Fig 6.2 with three distinct transport regimes emerging. For frequencies in the range ~1-100Hz, EP transport dominates DP and EO transport by 2 and 6 orders of magnitude in the vicinity of $\omega \approx 10$Hz and then decreases to become comparable to increasing EO transport for $\omega \approx 100$Hz. For frequencies in the range ~0.1-100kHz, EO first dominates over EP and continues to increase up to ~5kHz at which point it begins to diminish until DP eventually dominates both EP and EO for $\omega > 100$kHz.

The three dominant transport regimes that emerge in Fig 6.5 obviously correlate with the three microstructural regimes observed in Fig 6.2, which allows for direct connections to be made between assembly mechanisms and structures. For $\omega \approx$1-100 Hz, EP transport dominates EO and DP to produce oscillatory colloidal motion within the quasi-2D plane parallel to the substrate (Fig 6.2, column 1), although the colloidal localization within a centralized band is probably due to the finite role of recirculating EO flows in producing stagnation regions in between and on top of the electrodes. Small laterally organized clusters on top of the electrodes probably occur as the result of electrophoretic deposition in normal AC fields.[75] For $100\text{Hz} < \omega < 100\text{kHz}$, AC EO produces 3D periodic, recirculating flows on the parallel interdigitated electrodes within the confined microfluidic geometry,[91] which is particularly visible during assembly transients. These EO flows eject colloids from the electrode gaps and in combination with sedimentation reconcentrate colloids in stagnation regions on top of the electrodes (Fig 6.2, column 2).

As with EP transport, EO transport increases with increasing applied voltage and decreases with increasing solution ionic strength. In contrast to EP transport that operates in a quasi 2D plane parallel to the electrode gap surface at lower frequencies, the three dimensional flows due to EO transport also act in competition with gravitational transport of nanoparticles towards the electrode and gap surfaces, which results in more particles on the surface at lower applied voltages. The observed concentration of nanoparticles on top of the electrodes is probably a combination of sedimentation and EO flow stagnation points acting together, favoring the concentration of particles on the electrode surface (as a reminder, Fig 6.2 depicts only one gap in a series of parallel electrodes that can be expected to produce periodic EO flows).

The appearance of linear wire structures for ω>100 kHz (Fig 6.2, 3rd and 4th columns) occurs as a result of AC electric fields inducing dipoles in colloids, transporting colloids via DP, and assembling colloidal chains via dipolar interactions, which is consistent with Fig 6.5. Because DP transport occurs within the quasi-2D plane parallel to the substrate and orthogonal to gravity, sedimentation does not compete with dipolar chain assembly, although it does have some influence on confining heavier chains near the surface. As the applied voltage is increased, their is an increase in the number of chains, their rate of formation, and their cross sections via lateral dipolar chain attraction leading to their bundling.[86] In the region on top of the electrodes, there is no obvious evidence of dipolar chains oriented normal to the surface, but the presence of nanoparticles on the electrodes may indicate the importance of residual EP and EO mechanisms that might favor the presence of some nanoparticle near electrodes in

normal AC electric fields as well as some irreversible deposition. It does not appear that additional transport mechanisms (e.g. Joule heating) or more rigorous expressions accounting for multi-body colloidal[57] and hydrodynamic[60] interactions are necessary for semi-quantitatively understanding the microstructural assembly observed in Fig 6.2.

6.4.3 Impedance spectra of ordered colloidal configurations between interfacial microelectrodes

With an understanding of the connections between microstructure types and dominant transport mechanisms in Figs 6.2 and 6.5 we complete our understanding of the behavior and properties of nanoparticles in integrated microelectronic/microfluidic devices by measuring impedance characteristics as a function of AC field voltage and frequency. The measured impedance spectra is interpreted as a complex impedance, with the real part, $Re(Z)=|Z|\cos(\delta)$, and the imaginary part, $Im(Z)=|Z|\sin(\delta)$. It is important to point out that the function generator used to supply the bias voltage that drives colloidal assembly, delivers a load to the test fixture that needs to be calibrated out of the measurements along with the parasitic inductance and losses in the connecting leads. A schematic of the experimental set-up used to measure the impedance spectra of assembled colloidal configurations is shown in Fig. 6.6. We construct representative equivalent circuits to identify the relative contributions of various impedance components and remove these systematic experimental biases from the measurements.

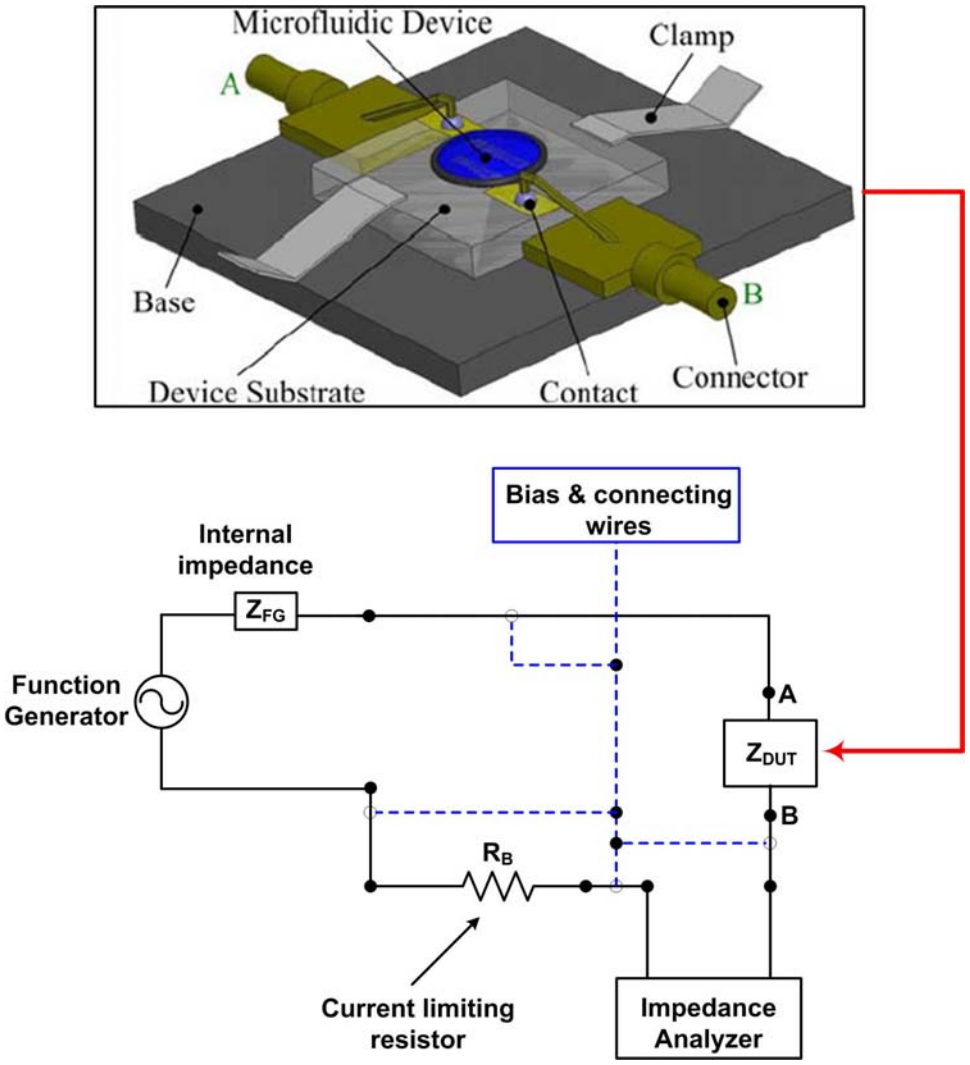

Figure 6.6. Schematic of the experimental set-up used to measure the impedance properties of the Device under Test (DUT). The DUT in this work is a microfluidic device where colloidal particle microstructures are actively manipulated to control electromagnetic properties.

Figure 6.7 shows a plot of the measured and modeled complex impedance data for the unbiased/off (random distribution of gold particles) and biased/on (formation of colloidal wires at 2.5 Vpp and 1 MHz) states of the microelectrode device. As shown in the insets of Fig 6.7, equivalent circuits fit to the measured impedance spectra account for contributions of the device components including the substrate, electrodes, electrolyte solution, and colloids (function generator and impedance analyzer included in calibration). Based on systematic control measurements, the micropatterned gold film electrodes in series with a 500Ω current limiting resistor had an equivalent bias-line resistance of R_{BL}=700Ω, the connecting wires had an inductance of L_{BL}=4.69μH, and the electrolyte media/unassembled colloids had a resistance of R_{OFF}=29kΩ. The collective capacitance of the electrodes, aqueous media, and gold colloids with and without AC fields was C_{ON}=C_{OFF}=25pF (since wires are only formed between a single set of fingers in the device, there is a negligible change in capacitance between states). Without the application of an AC electric field, the corresponding impedance spectrum in Fig 6.7 is dominated by the properties of the static gold microelectrode arrangement, glass substrate, and aqueous electrolyte media.

In the presence of an applied AC electric field (2.5V, 1MHz), the equivalent circuit components representing the device and aqueous media remain unchanged, but the assembled dipolar chains and electrolyte now produce a gap resistance of R_{ON}=1.7Ω and an inductance of L_{ON}=17fH. With ~20 parallel wires/100μm (from Fig 6.2 image) and a 5mm electrode interface, the resistance per wire is estimated to be 1.7kΩ (resistance per wire length is 1.7kΩ/30μm≈60Ω/μm). The cross sectional area per chain

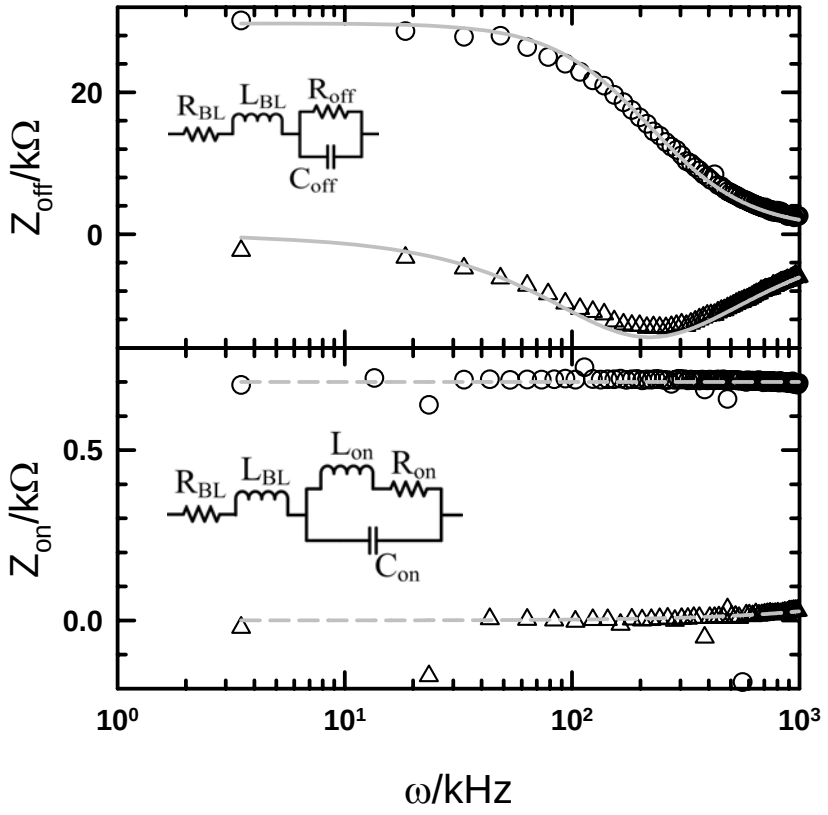

Figure 6.7. Measured real (circles) and imaginary (triangles) impedance spectra for (top) no applied field and (bottom) an applied field of 2.5V and 1MHz corresponding to the colloidal configuration shown in the upper right corner of Fig 6.2. Curve fits to the measured impedance spectra are based on equivalent circuits shown as insets in each case.

is not obvious given the "bundling" of many single chains via lateral dipolar chain attraction,[86] which limits the accuracy of resistivity estimates for comparison with other measurements of irreversible nanoparticle wires[84] or rods grown by membrane electrodeposition.[92] In addition, understanding the resistance of such dipolar chains involves modeling electronic transport through overlapping double layers on adjacent colloids,[93] which is beyond the scope of the present work. In any case, the electrostatic repulsion due to overlapping electrical double layers plays a vital role in preventing adhesive contacts while still providing a path of low resistance that allows such chains to function as "dipolar chain rheostats". This allows the device to function as an effective switch that can reversibly tune the electrical properties between the impedance spectra reported in Fig. 6.7a and b. For reference we provide analytical expressions for the real and imaginary parts of the equivalent circuit impedance (OFF and ON states) used to fit the measured impedance spectra in Fig. 6.7.

$$\begin{aligned}\mathrm{Re}\left(Z_{OFF}\right) &= \frac{R_{OFF}+R_{BL}+\omega^2 R_{BL}C_{OFF}^2R_{OFF}^2}{1+\omega^2C_{OFF}^2R_{OFF}^2}\\ \mathrm{Im}\left(Z_{OFF}\right) &= \frac{\omega\left(L_{BL}-C_{OFF}R_{OFF}^2\right)+\omega^3L_{BL}C_{OFF}^2R_{OFF}^2}{1+\omega^2C_{OFF}^2R_{OFF}^2}\end{aligned} \tag{6.6}$$

and

$$\mathrm{Re}\left(Z_{ON}\right) = \frac{\left(R_{ON}+R_{BL}\right)+\omega^2\left(R_{BL}C_{ON}^2R_{ON}^2-2R_{BL}C_{ON}L_{ON}\right)+\omega^4R_{BL}C_{ON}^2L_{ON}^2}{\left(1-\omega^2C_{ON}L_{ON}\right)^2+\omega^2C_{ON}^2R_{ON}^2} \tag{6.7}$$

$$\mathrm{Im}\left(Z_{ON}\right) = \frac{\begin{array}{c}\omega\left(L_{BL}+L_{ON}-C_{ON}R_{ON}^2\right)+\omega^5L_{BL}C_{ON}^2L_{ON}^2\\ +\omega^3\left(L_{BL}C_{ON}^2R_{ON}^2-C_{ON}L_{ON}^2-2L_{ON}L_{BL}C_{ON}\right)\end{array}}{\left(1-\omega^2C_{ON}L_{ON}\right)^2+\omega^2C_{ON}^2R_{ON}^2}$$

For the other configurations and transport mechanisms investigated in Figs 6.2 and 6.5, the impedance response was relatively trivial in the case of EO transport but significantly more complicated when EP transport dominates. In particular, when colloids were flushed from the electrode gap via EO transport, the impedance response and equivalent circuit were essentially the same as the unbiased device. For the dominant EP transport at low frequencies, concentrated bands of colloids within the electrode gap produced impedance spectra suggestive of an enhanced capacitive response consistent with a multi-plate capacitor arrangement with three parallel plates, where the middle plate is oscillating at a fixed frequency. This gives rise to very interesting transient impedance properties, but non-trivial measurement instabilities did not allow reliable steady-state impedance spectra to be obtained (probably due to the measurement hardware configuration). Although the microstructure formed via EP at low applied AC field frequencies needs to be better characterized to understand its impedance properties, its apparent increased capacitance might be exploited as a sort of microfluidic "electrophoretic varactor" in the future. Finally in Fig. 6.8 we show a schematic illustrating the multiscale nature of the measured impedance properties. The macroscopic device-level distributed impedance can be linked to nanoparticle physics and microstructure by representing individual dipolar chains using an equivalent circuit that identifies contributions by the colloidal particle and the electrical double layer to the electrical impedance. This suggests possible opportunities to improve the device response by either changing the particle geometry (nanorods) or medium properties (non-aqueous media), in effect altering the microscopic contributions to the equivalent

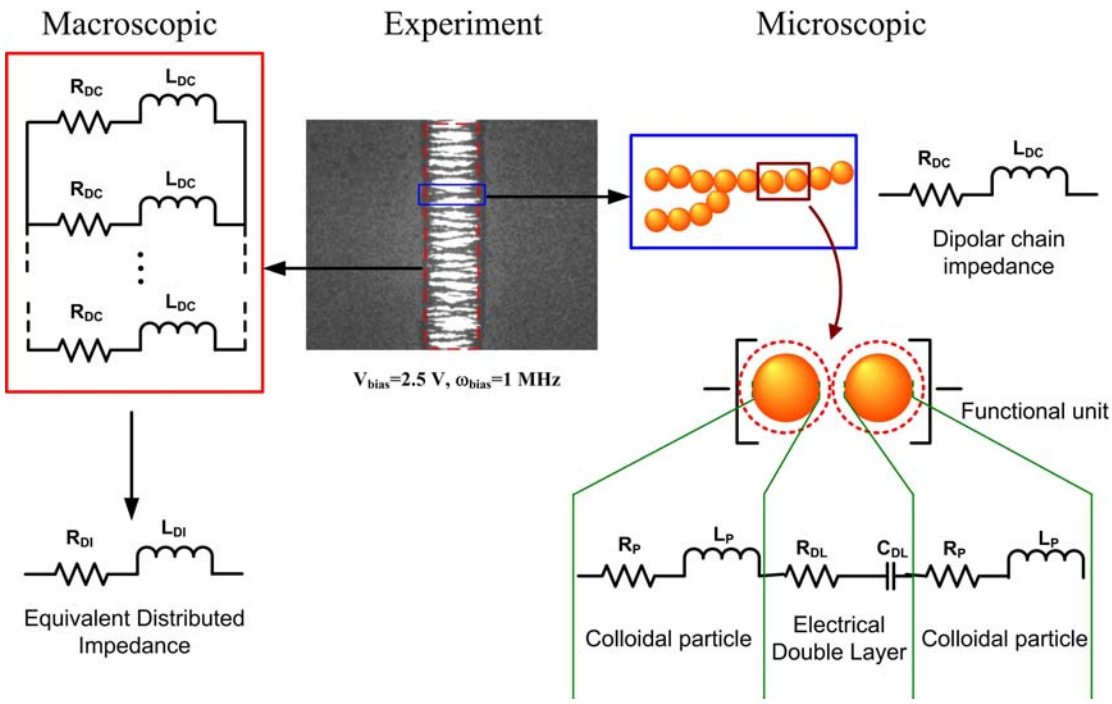

Figure 6.8. Schematic illustrating the multiscale nature of the measured impedance properties. The macroscopic device-level distributed impedance can be linked to nanoparticle physics and microstructure by representing individual dipolar chains using an equivalent circuit that identifies contributions by the colloidal particle and the electrical double layer to the electrical impedance.

device-level distributed impedance.

6.5. Conclusions

In conclusion, our results demonstrate the directed assembly of various colloidal configurations within coplanar microelectrodes via electrokinetic transport, which give rise to unique impedance properties. Predictions of dominant transport mechanisms are consistent with observed steady-state microstructures in different AC electric field frequency regimes. The success of these predictions for interpreting results in the present study provides a basis to explore new devices involving different (1) colloid shapes, sizes, and concentrations, (2) microelectrode geometries and configurations, (3) material properties including viscosity, dielectric properties, etc. The equivalent circuit models developed in this work reliably distinguish static device impedance properties from resistive, capacitive, and inductive contributions due to colloidal microstructures. The general approach developed in this work, which is to directly connect microstructure, transport, and impedance via quantitative models, should be broadly applicable to the design, control, and optimization of other integrated micro-electronic/fluidic devices.

7. SYTHESIS OF BOVINE-SERUM-ALBUMIN BASED ENCAPSULATED COLLOIDS FOR SELF-HEALING MATERIALS

7.1. Synopsis

Encapsulated colloidal particles containing a patented sealant inside a protein shell are synthesized for use in directed assembly experiments aimed at engineering self-healing materials. A fluid mechanics based correlation for the average size of Bovine Serum Albumin (BSA) protein microspheres, prepared using a water-in-oil emulsion technique, is presented. The correlation is formulated based on the theory of turbulent dispersion and a non-dimensional Weber number. Measured average diameters of the BSA microspheres prepared in olive oil at different stirring speeds are used to construct the correlation formula. The correlation gives good agreement with experimentally measured average diameters for a wide range of Weber numbers. This correlation is particularly useful to the pharmaceutical industry for predicting the size of encapsulated microspheres used in drug delivery prior to microsphere preparation. The effect of additives on microsphere size was also explored. The average diameter of the BSA microspheres was doubled by the addition of a bioadherent vitelline protein B solution. In addition, a Rosin-Rammler statistical distribution function is shown to accurately represent the microsphere size distribution obtained at different stirring speeds.

7.2. Introduction

There is considerable interest from the pharmaceutical industry about the entrapment of vaccines and drugs in biodegradable proteinaceous or polymeric micro- and nano-spheres. Microencapsulation is a promising method that: (1) increases the shelf life of a vaccine or drug when stored at room temperature; (2) offers the flexibility to control the release kinetics inside the body and the option for the drug or vaccine to be orally administered ; and (3) provides maximum protection with a minimum number of doses. In a recent review article, Kumar[94] surveyed the attractive properties, methods of preparation, and wide applications of a range of microspheres and microcapsules in controlled drug release formulations. Some commonly used microspheres in drug delivery include (a) Poly(lactide-co-glycolide) [PLG], (b) Albumin, (c) Chitosan, and (d) Alginate etc.[94]. It is important to recognize the distinction between microcapsules and microspheres. Microcapsules are essentially spherical particles containing a core substance (often the drug to be delivered). Microspheres are spherically empty particles (hollow core) [94]. Although different, these words are often used interchangeably, as in the later sections of this paper.

Albumin based microspheres, which result from polymerization of a disperse phase containing albumin (usually either human, bovine or egg albumin), are attractive macromolecular (drugs/vaccines) carriers due to their availability in pure form, biodegradability, non-toxicity, and non-immunogenicity [95]. Recent research [96,97] has also identified albumin microspheres as a potential macromolecular carrier for site-directed delivery. The preparation of albumin microspheres is straightforward and cost effective,

with much promise for large scale manufacturing. In this paper, we focus on developing Bovine Serum Albumin (BSA) based proteinaceous microspheres and, in particular, on the characterization of microsphere size. The protocol for BSA microsphere preparation used in this work was based on the standard water-in-oil emulsion technique [98-100], and is described in the next section. A wide range of different sized spheres can be obtained using this method. Here we note that the choice of the material to be encapsulated is restricted by the reactivity of the cross-linker or fixative (formaldehyde or glutaraldehyde) used. For example, it is difficult to encapsulate viable bacteria vaccines using this technique, however, a wide range of other drugs and vaccines can be encapsulated. The size of the resulting microspheres, in conjunction with their composition, influences the drug release kinetics inside the body. Also, the microsphere size plays a crucial role when targeting a particular site in the body; for example, bioadherent microspheres from 1-10 μm in size are absorbed by the Peyer's patch found in the gut of cattle, while the larger vaccine/drug loaded microspheres just pass through without having any effect. It is also desirable to make microspheres with a uniform size distribution to reduce the size-induced variability (of release kinetics) in a given population of microspheres. Despite the importance of microsphere size, we have not found any research in the microencapsulation literature that uses a mathematical framework to investigate the mechanism of Albumin based microsphere formation and microsphere size. The majority of the existing size characterization studies use a Scanning Electron Microscope (SEM) to image the microspheres, and then estimate the mean size and size distribution, using qualitative arguments to explain the variation of

size with process parameters. It is therefore useful to develop a correlation that is a function of the operating variables and provide an engineering approach to estimate the microsphere size for design and testing purposes. Inspired by previous work in fluid mechanics on droplet sizes in aqueous-oil dispersions [101-103], we develop and validate a correlation for the average diameter of BSA microspheres in this work.

Next we review the literature on turbulent aqueous-oil dispersions. Two-phase dispersions play an important role in many industrial processes in the chemical, biochemical, food processing, and pharmaceutical industries. The mechanical agitation of oil and liquid phases in a stirring vessel results in the formation of a dispersion. The dynamic equilibrium between droplet breakdown and coalescence determines the size distribution of the droplets (oil droplets in the case of oil-in-water emulsion and liquid droplets in the case of water-in-oil emulsions). Droplet size influences heat and mass transfer, and chemical reactions in chemical and biochemical processes, but it is a critical parameter in the pharmaceutical industry for erodable capsules. The importance of droplet size distribution and the dynamics of droplet breakdown have driven a number of experimental, numerical, and simulation studies on the phenomenon of droplet dispersions, starting from the work of Kolmogorov [101] and Hinze [102]. Subsequently, it has been customary to relate the mean Sauter diameter and the maximum droplet size to a non-dimensional Weber number [104], which represents the balance between inertial forces and surface tension forces on the drop. The maximum droplet size can be obtained by applying Kolmogorov's theory of isotropic turbulence as explained in [105-107] and also later in this paper. A variety of system variables ranging from physical properties of the

liquid, volume fraction of the dispersed phase, temperature, and the type of mechanical mixing used, influence the mean droplet size. A number of quantitative correlations for droplet size that incorporate system variables have been developed by various researchers from theoretical and experimental results (see Zhou and Kresta [103] for a review and tabulated list of various correlations for mean drop diameter in liquid-liquid mixing tanks). However, recent experimental and theoretical work has revealed significant limitations and shortcomings of the classical drop size correlations, especially when the turbulence is strongly intermittent [106]. For the present work with BSA we explore drop size correlations by comparisons with experimentally measured average microsphere diameters prepared in olive oil at various stirring speeds. Also, the corresponding microsphere size distributions are modeled using the empirical Rosin-Rammler statistical distribution function.

This paper is organized as follows: In the next section, we describe the materials and experimental methods used in this work. The protocol for BSA based microsphere preparation is also outlined. The theory and mechanism of microsphere formation is discussed in the following section. An expression for the maximum/average microsphere diameter based on a generalized non-dimensional Weber number is derived using Kolmogorovs' theory of isotropic turbulence. The SEM micrographs of BSA microspheres and comparison of the correlation with the experimental results is presented in the results section. We then comment on the effect of additives on microsphere size. Also, the theoretical predictions of the Rosin-Rammler distribution function are compared with the experimentally obtained microsphere size distributions.

The average diameter and size distributions of microspheres consisting of BSA and a recombinant vitelline protein B (vpB) (a known bioadhesive [108]) were compared with the size of the microspheres containing BSA alone. Finally, we present the conclusions of our research and future work.

7.3. Materials and Methods

7.3.1 Materials

The BSA (fraction V, M_r 60,000, 96 % pure), formaldehyde, buffers, and other miscellaneous items used in this research were purchased from Sigma. Vitelline protein B (vpB) was produced recombinantly from an E. coli clone developed in the Department of Medical Biochemistry and Genetics at Texas A&M University, and then isolated and purified. Commonly available Bertoli classic olive oil with a viscosity of 84 cp at 23^o C was used.

7.3.2 Preparation of microspheres

The BSA-based microspheres were prepared by a water in oil emulsion technique described next. The protocol used to make the BSA microspheres involved glutaraldehyde/ formaldehyde cross-linking, as previously described in [98], and more recently used by Giletto et al. [99] to prepare microspheres for delivering vaccines. As the latter report cannot be easily accessed, we review the protocol in detail:

1. First, 100 ml of the oil (olive oil, PAO oils) was stirred at a pre-determined stirring speed (N) for 30 minutes in a 400 ml Pyrex beaker. A Caframo

ultra high torque stirrer (Model BDC1850) with a speed range of 300-1800 rpm was used to stir the oil.

2. Then 2 ml of a 125 mg/ml protein solution containing BSA, vpB, and the drug to be encapsulated (dispersed phase) was added to the oil and stirring was continued for 30 minutes.
3. The aqueous droplets in the emulsion were polymerized by adding 50 μl of an aqueous formaldehyde solution (37% formaldehyde). The emulsion was stirred for an additional 30 minutes.
4. Finally, 50 μl of glycine (a capping agent) was added to consume the remaining cross-linker and the emulsion was stirred for an additional 15 minutes.
5. The microspheres were then collected by centrifugation at 3000 rpm for 20 minutes. The supernatant oil was then decanted, and the pelleted microspheres were washed in ether to remove the residual oil. The centrifugation and ether washes were repeated to remove any oil traces. Very high yields of free flowing microspheres ($> 90\%$) were obtained using this method.

The size of the microspheres was determined by a Jeol JSM-6400 scanning electron microscope at the Electron Microscopy Center at Texas A&M University. Samples of the microspheres were mounted onto aluminum stubs using a double sided carbon adhesive tape. A 40 nm gold-palladium coating was sputtered on the microspheres using a sputter coater in an atmosphere of argon. Coating was achieved at 10mA for 4 minutes. Scanning was performed at ambient temperature and vacuum pressure with a beam

voltage of 12 kV. The average microsphere diameter was quantitatively determined by measuring the size of around 130-450 microspheres from the SEM micrographs using the Scion Image Analysis software. The “Analyze Particles" option in the software automatically counts, labels, and measures microspheres in the SEM micrographs. The SEM images have to be saved as binary or threshold images. The image is scanned across until the boundary of a microsphere is detected. Then an inbuilt outlining tool was used to outline the microsphere boundaries. The sizes of the microspheres were measured using the measure command that uses a pre-set length scale to compute the diameter. The microspheres were then redrawn in a different gray level so they become invisible to the scanning process to avoid counting the same sphere twice. The size distribution histogram was then constructed from the raw data of measured microspheres, by organizing the data into a frequency table with equidistant size intervals.

7.4. Theory and Mechanism of Microsphere Formation

To develop a fluid mechanics based correlation for the mean diameter of BSA microspheres, it is important to understand the physical underpinnings of the water-in-oil emulsification technique used to make the spheres. In the following, we briefly review the basic principles of emulsification and droplet formation. A substantial literature of experimental, theoretical, and numerical work that discusses the stability of emulsions and the mechanisms of droplet breakdown are available (see [103,109,110] for details). It is to be expected that when an aqueous protein solution is added to oil and agitated,

dispersion is formed in which continuous break-up and coalescence of drops occur (Note that the protein solution and the oil are immiscible). The droplets are continually broken down by turbulent velocity fluctuations (inertial forces). Figure 7.1 shows a simple schematic of the stirred tank and the mechanism of droplet break-up across the impeller boundary layer. The strong shear across the boundary layer first deforms and then breaks down the droplet [111]. Most of the droplet breakdown occurs in a zone near the edge of the impeller blade. The interfacial tension between the dispersed phase and the continuous medium, and the viscous stresses inside the droplet act as restoring and damping forces respectively that tends to maintain the shape and size of the droplet. A stable droplet size is obtained when the deforming inertial forces are balanced by the surface tension forces and can no longer break down the droplets. Coalescence occurs when the agitated droplets collide with each other. A dynamic balance is eventually established between the drop break up and coalescence processes, and a distribution of different sized stable drops are obtained.

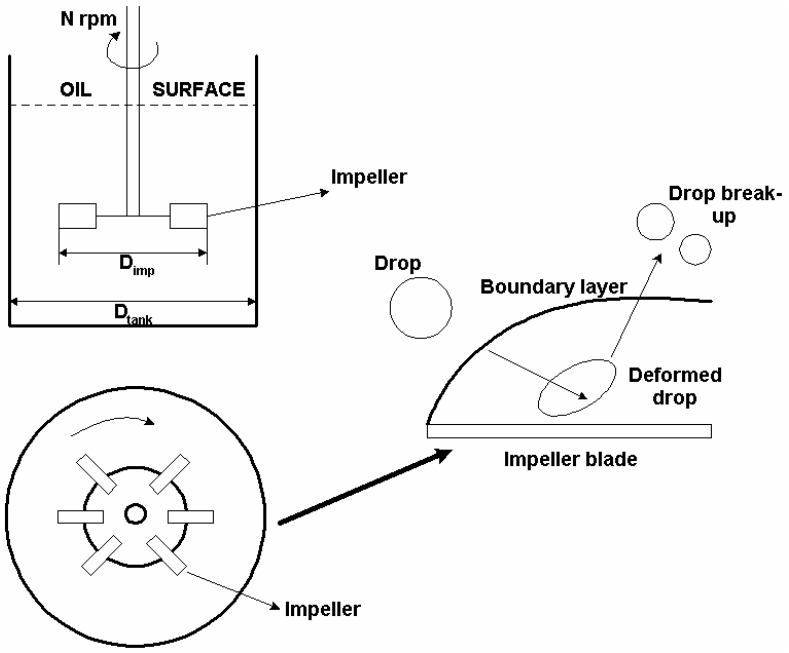

Figure 7.1. Schematic of the stirring tank and mechanism of droplet breakdown across the impeller boundary layer.

The solid BSA microspheres are obtained by polymerizing the stable aqueous protein droplets formed at the end of step 2 of the microsphere preparation protocol. We can approximate the size of the protein droplets to be proportional to the size of the solid microspheres they form after polymerization. The average drop size and the final size distribution of the microspheres depends on the operating parameters, such as mixer geometry, type of impeller used, stirring speed, temperature, physical properties of the oil and protein solution (viscosity, surface tension), and the volumetric throughputs of the dispersed phase. Based on ideas from previous work about water-in-oil emulsions [103,106,107], we derive a relation based on a non-dimensional Weber number (We) to predict the average size of BSA microspheres.

Two independent non-dimensional numbers were obtained from dimensional analysis, which can account for the force balance between inertial, surface tension, and viscous forces [102]. The first is a generalized Weber number (We) that represents a balance between inertial and surface tension forces. The second parameter is a Viscosity number (Vi), defined as the ratio of the square of the dispersed phase viscous force and the product of the inertial and surface tension forces [102]. They can be mathematically expressed as:

$$We = \frac{\tau}{\sigma/d} \tag{7.1}$$

$$Vi = \frac{\mu_d}{\sqrt{\rho_d \sigma d}} \tag{7.2}$$

where τ represents the normal stresses generated by turbulent events, d is the diameter of the droplet, σ is the interfacial tension at the protein-oil interface, and ρ_d, μ_d are the density and viscosity of the dispersed phase, respectively. Here, we consider the case of a dilute non-viscous, non-coalescing, dispersed phase, where the viscous stress within a protein drop is negligible compared with the interfacial tension at the drop-oil interface (i.e., Vi $\rightarrow 0$). Of significance here is the smallest eddy length scale (η), commonly referred to as the Kolmogorovs' length scale ($\eta = (\frac{\nu^3}{\varepsilon})^{1/4}$, where ε is the rate of turbulent energy dissipation and ν is the kinematic viscosity), and the largest eddy length scale L. For droplet breakdown in the inertial sub-range ($\eta < d < L$), the viscous stresses are negligible compared with the turbulent stresses. Also, the turbulent stresses across a

droplet of size d can be expressed as $\rho_c \overline{v^2}$, where ρ_c is the density of the continuous phase and $\overline{v^2}$ represents the root-mean-square value of the turbulent velocity fluctuations [103]. Also, when the turbulence is isotropic $\varepsilon \propto (\overline{v^2})^{3/2}/d$ [103]. Consequently, the Weber number becomes:

$$We = \frac{\rho_c \overline{v^2} d}{\sigma} = \frac{c \rho_c \varepsilon^{2/3} d_{max}^{5/3}}{\sigma} \tag{7.3}$$

Assuming $v \propto ND$ (where N is the stirring speed and D is the impeller diameter) and the turbulence in the tank to be isotropic and fully developed, the turbulence energy dissipation (ε) can be shown to be $\varepsilon \propto N^2 D^3$) [103,106]. Then

$$\frac{d_{max}}{D} = c\left(\frac{\rho_c N^2 D^3}{\sigma}\right)^{-3/5} = c We_m^{-\alpha} \tag{7.4}$$

where We_m is the Weber number of the mixing tank, and c, α are constants to be uniquely determined for different emulsions. However, the value of the exponent α has been found to be 0.6 for isotropic turbulent drop dispersions [102,103,106]. Here we point out that a We_m based on the width of impeller tip instead of the diameter of impeller would be a more appropriate parameter as the trailing vortex at the impeller tip is believed to be the major mechanism of droplet breakdown in stirred tanks. When viscous energy within a drop or coalescence becomes important, Eq. (7.4) can be corrected as [103]

$$\frac{d_{max}}{D} = f\left(\frac{\mu_d}{\mu_c}, \phi\right) c We_m^{-\alpha} \tag{7.5}$$

where μ_d and μ_c are the viscosities of the dispersed and continuous phase, respectively, and ϕ is the volume fraction of the dispersed phase. We note that in the context of this work $f(\frac{\mu_d}{\mu_c},\phi)=1$. The Sauter mean diameter (d_{32}) has generally been assumed to be proportional to the maximum sphere diameter (d_{max}).

$$d_{32}=\frac{\sum_{i=1}^{k} n_i d_i^3}{\sum_{i=1}^{k} n_i d_i^2} \propto d_{max} \tag{7.6}$$

where i denotes the size range considered, n_i is the number of microspheres in size range i, and d is the diameter of the microspheres. The generality of this assumption has been questioned in recent work by Pacek et. al. [104]. However, as the drop size distribution is universal, all scales and representative diameters are uniquely related. As a result, the average diameter of the microspheres (d_{ave}) is also proportional to d_{max}. Then, from Eq. (7.5)

$$\frac{d_{ave}}{D}=f(\frac{\mu_d}{\mu_c},\phi)c_1 We_m^{-\alpha} \tag{7.7}$$

This correlation forms the basis for our work, and one of our main objectives is to determine the values of α and c_1 for BSA microspheres.

7.5. Results and Discussion

7.5.1 Microsphere size and size distributions

The theory discussed above has been validated against experimentally measured average microsphere diameters for a wide range of stirring speeds. All BSA based

microspheres were prepared using the protocol described in the earlier section. In each case, the agitation was provided by a Caframo stirring paddle with a pitched-blade impeller (diameter of the impeller blade = 5.8 cm). The impeller was positioned in the center of the Pyrex beaker and in the middle of the oil surface and the bottom surface of the beaker. Olive oil was used as the continuous phase and BSA acts as the dispersed phase. The volume fraction of the BSA used was 2% v/v. An aluminum foil lid was used to seal the top of the beaker to avoid splatter of the oil emulsion and reduce air entrainment. The entrained air bubbles can damp the turbulence intensity [103] and affect the size of microspheres and microsphere formation. So it is necessary to make the stirring vessel as air-tight as possible. To remove any residual oil or microspheres, the mixing vessel is washed thoroughly in tap water and then rinsed in double distilled water prior to each experiment.

To study the effect of impeller speed on average microsphere size, BSA-based microspheres were prepared in olive oil at different stirring speeds (300 - 1800 rpm). The lowest stirring speed of 300 rpm corresponds to the minimum stirrer speed required to provide homogeneous mixing and completely disperse the BSA in the oil. The choice of the highest speed was restricted by the operating speed range of the mixer used. For microspheres prepared using each impeller speed, the average microsphere size is computed from the SEM micrographs using the Scion Image analysis software as described earlier. Figure 7.2 shows the SEM micrographs of BSA microspheres prepared in olive oil at (a) N =800 rpm (b) N= 1200 rpm (c) N = 1500 rpm and (d) N = 1800 rpm. The corresponding number fraction distribution histograms, plotted against the BSA

microsphere diameter, are shown in Fig. 7.3. As expected, smaller microspheres are formed as the impeller speed is increased. Microspheres ranging in size from $1-10\mu m$ can be made using the current preparation method in olive oil, as seen from Fig. 7.3. It can be observed from the SEM micrographs that some of the microspheres appear wrinkled and rough and there is an apparent problem of clustering or aggregation of spheres for speeds lower than 1200 rpm, as evident in Fig. 7.2(a). The spheres look wrinkled because of the loss of water from the core of the microspheres through the pores on the surface of the microsphere [99]. The amount of shrinkage depends on the time delay between microsphere preparation and imaging the microspheres. It has been observed in previous work [99] that sonicating the wet centrifuged particles for approximately two minutes successfully separated the clustered microspheres. It is also important to observe that more uniform shaped and sized microspheres were formed with increasing stirring speeds. A slightly higher volume of formaldehyde (cross linker) and capping agent (glycine) was required to form spheres when the stirring speed N < 800 rpm. When the volume of formaldehyde and glycine specified in the protocol was used to prepare microspheres with lower impeller speeds, the resulting microspheres were mostly misformed, as seen in Fig. 7.4. This can be attributed to the greater time required for the polymerizing (cross-linking) action at lower impeller speeds. As the time of stirring in each preparation step is maintained the same as specified in the protocol, immaterial of the stirring speed, an additional volume of formaldehyde is added to both facilitate faster cross linking and enable the formation of well defined microspheres.

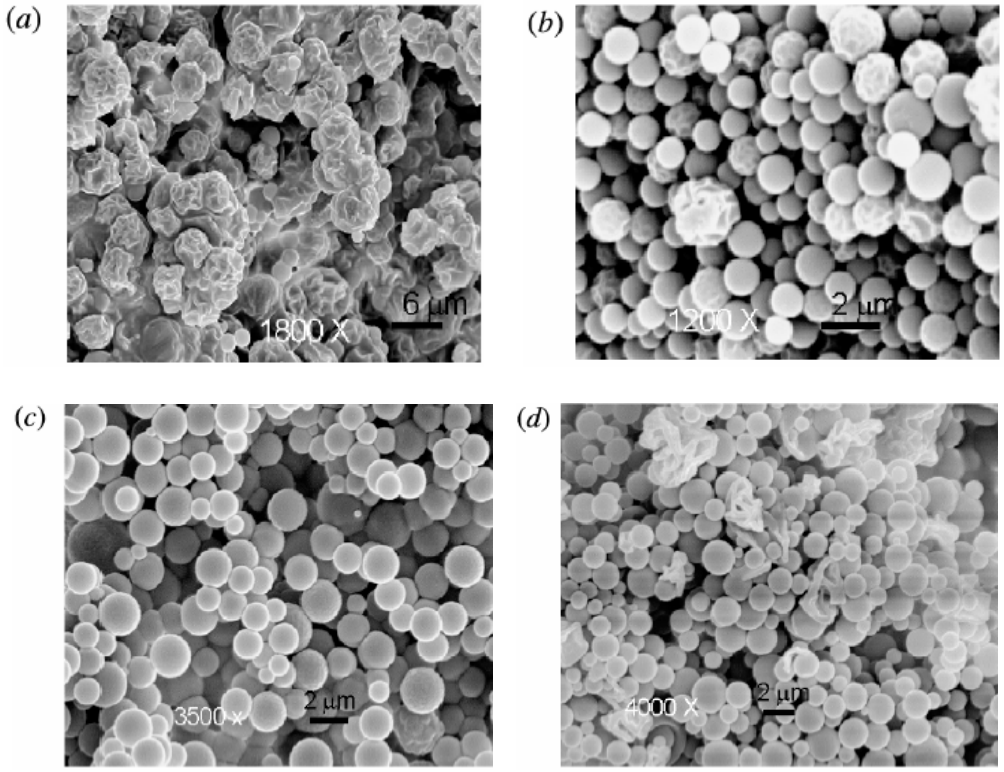

Figure 7.2. SEM micrographs of BSA microspheres prepared using the water-in-oil emulsion technique in olive oil at a) N=800 rpm, b) N=1200 rpm, c) N=1500 rpm, and d) N=1800 rpm.

7.5.2 Comparison of theoretical predictions with experimental results

The average microsphere diameter predicted by the theory outlined above was tested against experimental data for a wide range of We_m (i.e., a wide range of stirring speeds). The mixing tank Weber number is calculated from Eq. (7.4), using the density of continuous medium (olive oil), the impeller diameter, stirring speed in rpm, and the interfacial tension at the BSA-olive oil interface ($\sigma = 0.0229 N/m$). The average diameters of the BSA microspheres formed and the corresponding Weber numbers are tabulated in Table 7.1. Figure 7.4 shows the theoretical prediction of the average

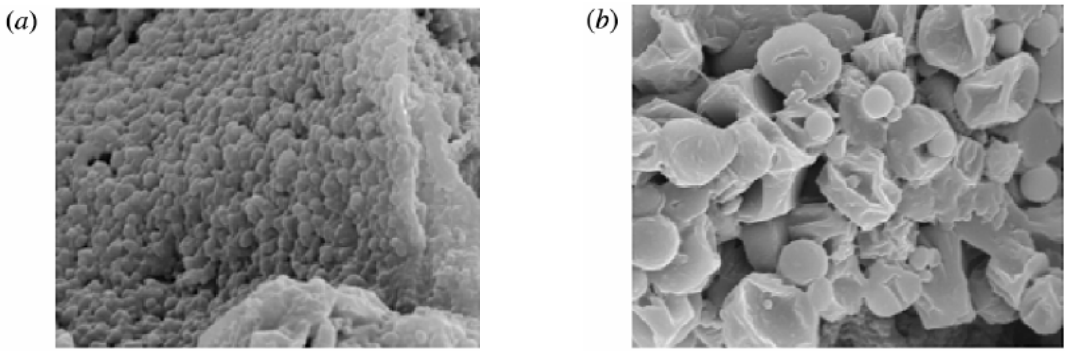

Figure 7.3. SEM micrographs of BSA microspheres prepared in olive oil at (a) N =300 rpm, and (b) N= 500 rpm when adequate cross-linker is not added. Notice that the microspheres are mostly deformed and clustering and aggregation of the still unformed microspheres is evident.

diameter given by Eq. (7.7), for three different sets of coefficients c_1 and α. It is evident from Figure 7.5 that the coefficients $c_1 = 0.0206$ and $\alpha = -0.53$, obtained from a least square fit to the experimental data, provides the best fit. The deviation of the Weber number exponent from the classical value of -0.6 is to be noted (although the fit is reasonable when $\alpha = -0.6$, a better correlated fit is obtained when $\alpha = -0.53$). However, it is important to recognize that if the microspheres were prepared in a different oil (say castor oil or PAO oils) at different stirring speeds, the average microsphere diameter can still be determined using the correlation given by Eq. (7.7).

Table 7.1. Experimentally obtained average diameters of BSA microspheres prepared in olive oil at different stirring speeds

Speed	Mixing tank Weber number (We_m)	Average microsphere diameter
(rpm)		(μm)
300	7736	10.08
500	21490	6.12
800	55014	3.85
1200	123782	2.03
1500	193409	1.82
1800	278509	1.29

7.5.3 Effect of additive on microsphere size

It is important to analyze the effect of additives on microsphere size. By additives we mean the drug to be encapsulated or any other material added to alter the drug release kinetics or other surface properties of the microspheres. The additives, along with BSA in this case, are incorporated in the dispersed phase. The small volume fractions of the dispersed phase used in this study does not affect the size of the microspheres. Also, as the ratio of the dispersed phase viscosity to the oil viscosity (μ_d/μ_c) is small, viscous effects do not influence microsphere formation. Thus, we surmise and later show that the size of microspheres can be controlled by using suitably chosen additives.

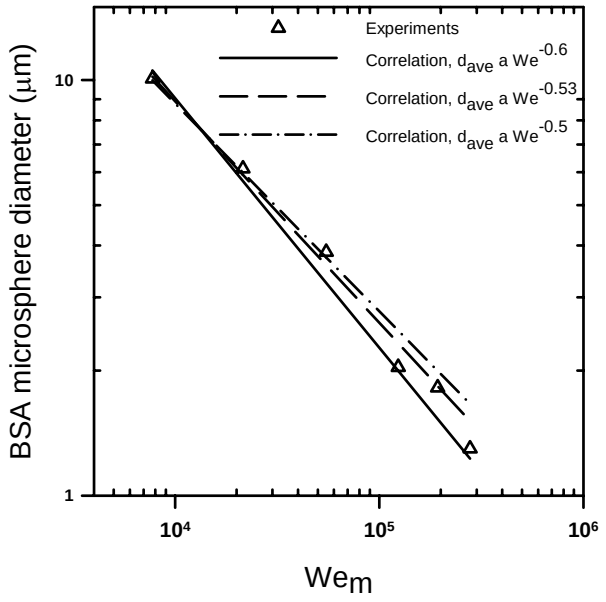

Figure 7.4. Average diameter of BSA microspheres prepared using the water-in-oil emulsion technique in olive oil as a function of We_m.

In the following we study the effect of adding vpB protein (to the dispersed phase) on microsphere size. The BSA+vpB microspheres were prepared using the same protocol described in Section 2.2, except that 2 ml of 125 mg/ml BSA + 0.015% vpB is added in step 2 to form the dispersed phase. Also, as noted by Giletto et al. (1998), it was not possible to prepare 100% vpB microspheres because of the very low solubility ($\approx 20 mg/ml$) of the protein at neutral pH.

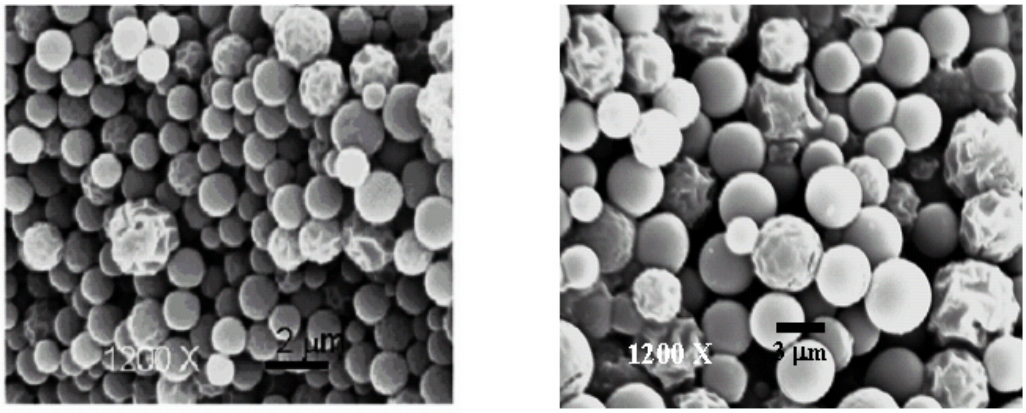

Figure 7.5. SEM micrographs of (a) BSA microspheres prepared in olive oil at N = 1200 rpm, and (b) BSA + 0.015% vpB microspheres prepared in olive oil at N =1200 rpm.

The SEM micrographs of (a) BSA microspheres prepared in olive oil at N = 1200 rpm and (b) BSA + 0.015% vpB microspheres prepared in olive oil at N = 1200 rpm are shown in figure 7.5. The addition of vpB to the dispersed phase alters the interfacial tension at the protein/oil interface but negligibly changes the viscosity of the dispersed phase. As a result the We_m for BSA + vpB microsphere is different compared with the We_m corresponding to the preparation of just BSA microspheres (ρ_c , N and D remain the same). As the average diameter scales as $We_m^{-\alpha}$, we can infer that the addition of vpB increased the interfacial tension, thus reducing We_m and increasing d_{ave}. The SEM micrographs in figures 7.5 (a), (b) indicate that the BSA+vpB microspheres, besides being larger than the BSA microspheres, appear more rigid and rounded with well defined boundaries. The vpB is known to be a mechanically tough and chemically resistant eggshell protein [108], and its presence makes the microspheres rigid. Some of the

microspheres appear wrinkled because of the water loss. Clustering and aggregation effects were less pronounced in the microspheres that contained vpB.

7.5.4 Microsphere size distribution function

In this section, we formulate a distribution function $f_N(x)$ to represent the number fraction distribution of BSA microspheres. A wide variety of mathematical and empirical distribution functions, that include normal, log-normal, exponential, Rosin-Rammler, Nukiyama-Tanasawa etc., have commonly been used to fit experimentally measured size distributions [112]. As it is difficult to construct a generalized functional form to represent all microsphere size distributions, it becomes imperative to try different distribution functions to find the best fit. We found that a normal probability plot of the experimentally measured microsphere diameters gives a poor fit to the data, as did a lognormal distribution.

In this work, we use the Rosin-Rammler empirical relationship given below to model the size distribution. The expression is straightforward [112]:

$$f_N(x) = \frac{a}{b}(\frac{x}{a})^{b-1}\exp(-(\frac{x}{a})^b) \tag{7.8}$$

where *a* and *b* are constants to be determined. The experimentally measured number fraction distributions are described in terms of the two parameters a and b. The Rosin-Rammler distribution has an analytical form for the cumulative distribution $F_N(x)$, given by.

$$F_N(x) = \int_0^x f(u)du$$

$$F_N(x) = 1 - \exp(-(\frac{x}{a})^b) \tag{7.9}$$

Table 7.2. Empirically obtained correlation coefficients for number fraction distributions. A Rosin-Rammler distribution function of the form $f_N(x) = \frac{a}{b}(\frac{x}{a})^{b-1}\exp(-(\frac{x}{a})^b)$ is used to model the cumulative fraction distributions of BSA and BSA + 0.015 % vpB microspheres

Material	Speed	Mixing tank Weber number (We_m)	a	b
	(rpm)			
BSA	800	55014	3.974	3.853
BSA	1200	123782	2.005	5.629
BSA	1500	193409	1.793	5.212
BSA	1800	278509	1.281	3.788
BSA + 0.015 % vpB	1200		3.884	4.744

Data for the microsphere size is generally presented as a number fraction or a cumulative fraction in the literature. The coefficients *a* and *b* in Eq. (7.8) are obtained from a least square fit to the experimental number fraction data. Table 7.2 contains the Rosin-Rammler distribution constants corresponding to size distribution of BSA and

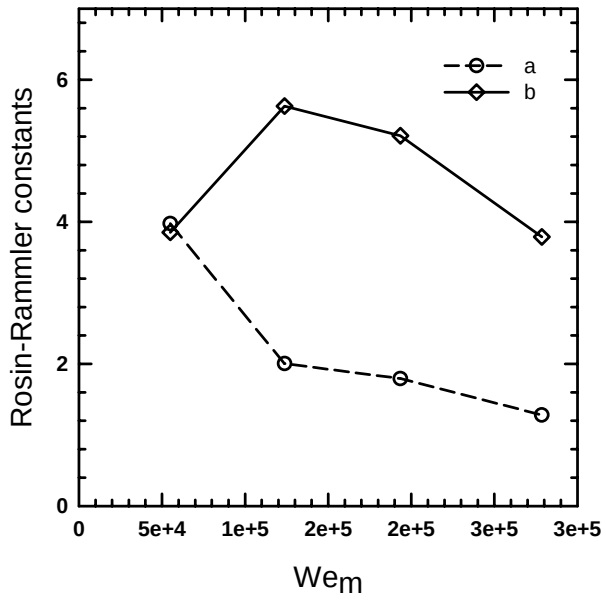

Figure 7.6. Variation of the Rosin-Rammler constants *a* and *b* with We_m.

BSA+vpB microspheres prepared at different stirring speeds. The mixing tank Weber number (We_m) is also included in the table for reference. The variation of the constants a and b with We_m is also shown in figure 7.6. While the value of *a* reduces with increasing We_m, *b* appears to increase till it reaches a maximum and then reduces for $We_m > 150000$. Figure 7.7 shows the number fraction distribution of BSA microspheres prepared in olive oil at different speeds. The number fraction predicted by the theoretical Rosin-Rammler distribution (Eq. (7.8)) is found to be in good agreement with the experimental values. To quantify the uniformity and spread of the BSA

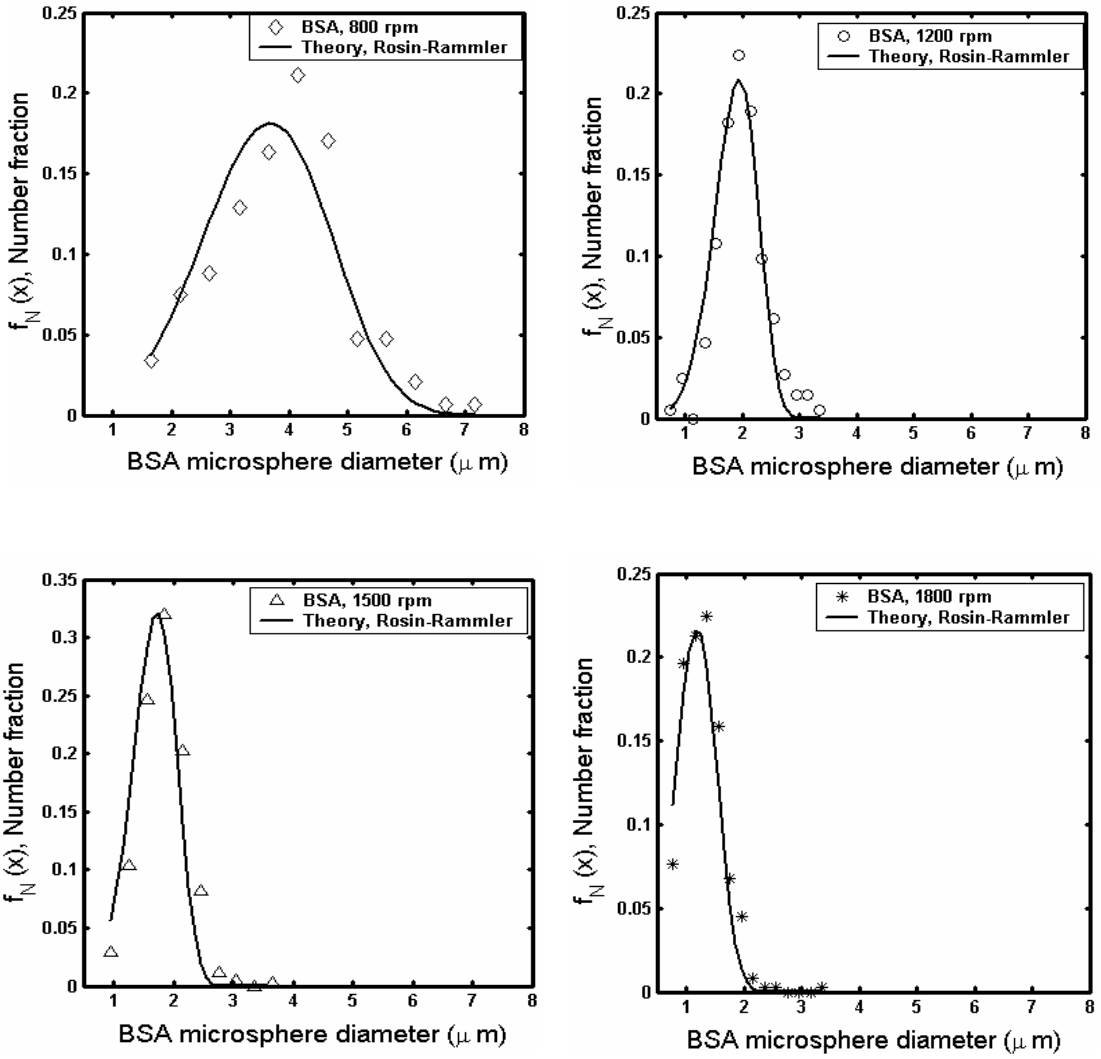

Figure 7.7. Normalized number fraction distributions of BSA microspheres prepared in olive oil at N = 800, 1200, 1500, and 1800 rpm. A Rosin-Rammler distribution function is used to fit the experimental data.

microsphere size distributions, we introduce the *distribution mid-span* (δ_{mid}). This parameter represents the width of the size distribution at half the maximum value of the number fraction. The δ_{mid} of BSA microspheres obtained from the corresponding Rosin-Rammler size distribution function is plotted as a function of We_m in figure 7.8. The value reduces with increasing We_m, indicating a more uniform size distribution at higher stirring speeds. Figure 7.8 shows that there is no significant difference in the relative magnitude of δ_{mid} for BSA microspheres prepared at 1200, 1500, and 1800 rpm. However, a much wider distribution is obtained in the case of BSA microspheres prepared at 800 rpm. The larger turbulent kinetic energy available in the system at higher speeds results in the rapid breakdown of the protein droplets to their stable diameters. For the case of impeller speeds lower than 800 rpm, a longer stirring time is required to obtain a distribution of stable protein drops. As the time of stirring is kept constant in the protocol, irrespective of stirring speed, the size distribution is wider when $N \leq 800 rpm$.

The cumulative number fraction computed using Eq. (7.9) is a good fit to the experimental data, as seen in figure 7.9. It is useful to plot a universal cumulative distribution curve, as shown in figure 7.10, to provide an insight into the size distribution characteristics prior to microsphere preparation. A new scaling parameter $(d/a)^b$ is defined to collapse the experimentally obtained cumulative number fraction distributions onto a single distribution curve.

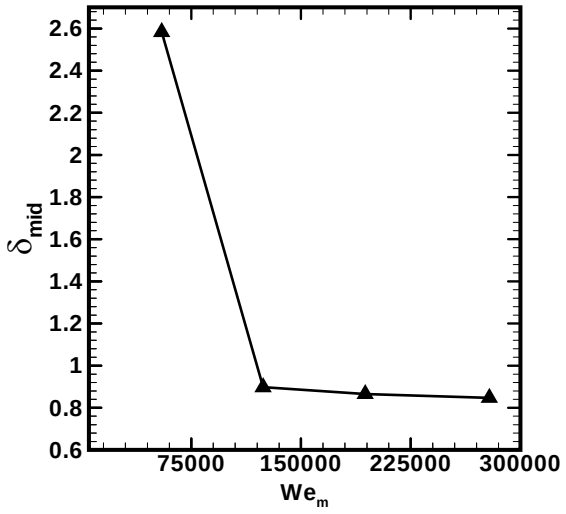

Figure 7.8. The distribution mid-span (δ_{mid}) for BSA microspheres obtained from the corresponding Rosin-Rammler distribution as a function of We_m

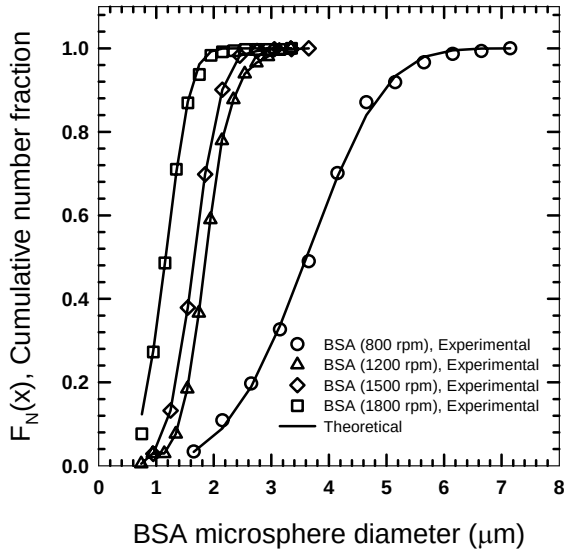

Figure 7.9. Cumulative number fraction distributions of BSA microspheres prepared in olive oil at N = 800, 1200, 1500, and 1800 rpm. A Rosin-Rammler distribution function is used to fit the experimental data.

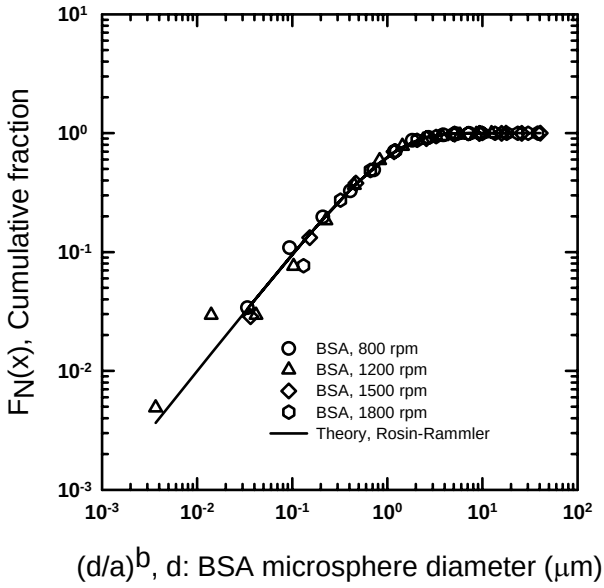

Figure 7.10. Universal cumulative number fraction distribution of BSA microspheres prepared in olive oil. The cumulative size distributions of BSA microspheres prepared at N = 800, 1200, 1500, and 1800 rpm are collapsed onto a single distribution curve.

Figures 7.11 and 7.12 compare the number and cumulative fractions of a) BSA microspheres prepared in olive oil at 1200 rpm, and b) BSA + 0.015% vpB microspheres prepared in olive oil at 1200 rpm, respectively. The Rosin-Rammler distribution also accurately models the size distribution of the BSA+vpB microspheres. However, the addition of the vpB almost doubles the average microsphere diameter and significantly alters the spread of the distribution as seen in figures 7.11 and 7.12, as discussed in the previous section. The BSA+vpB microspheres can be seen to have a much higher

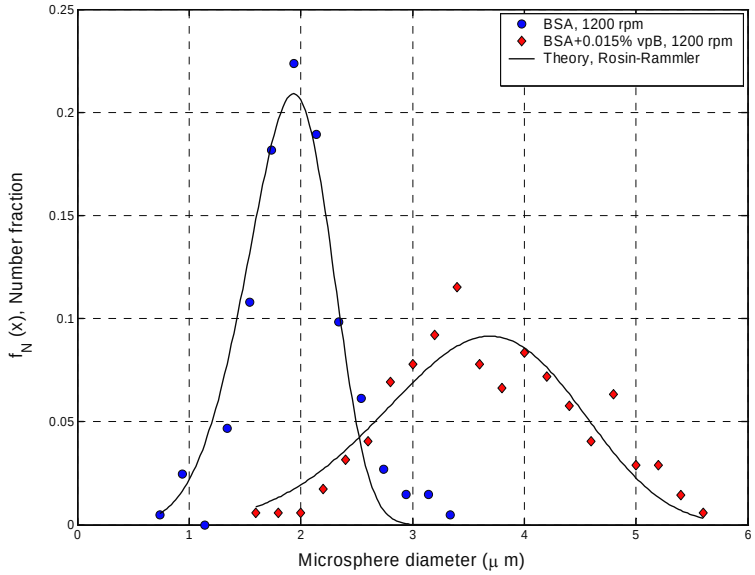

Figure 7.11. Normalized number fraction distributions of (a) BSA microspheres prepared in olive oil at N = 1200 rpm, and (b) BSA + 0.015% vpB microspheres prepared in olive oil at N = 1200 rpm. A Rosin-Rammler distribution function is used to fit the experimental data.

distribution mid-span when compared with the BSA microspheres prepared at the same stirring speed.

7.5.5. Self-healing materials using functional colloids and AC electric fields

With the increased interest in human missions into space and to inter-stellar planets, development of new advanced materials for spacecraft construction has assumed high priority. Smart materials along with other technologies are necessary to build a spacecraft capable of traveling millions of miles from Earth into hostile environments, where repairs will be impossible. The focus has therefore been on developing new

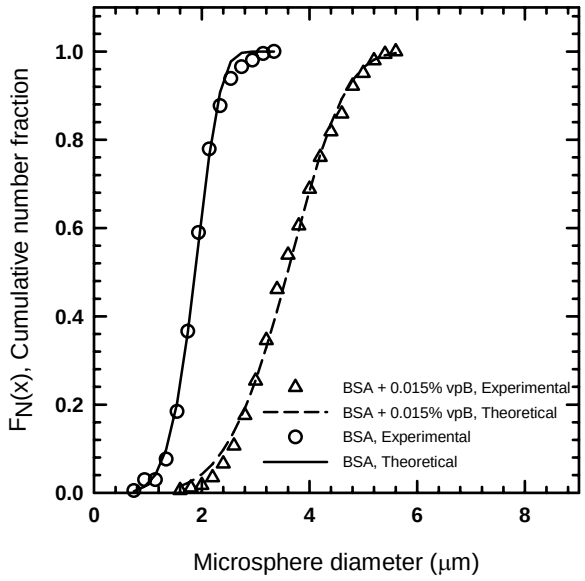

Figure 7.12. Cumulative number fraction distributions of (a) BSA microspheres prepared in olive oil at N = 1200 rpm, and (b) BSA + 0.015% vpB microspheres prepared in olive oil at N = 1200 rpm. A Rosin-Rammler distribution function is used to fit the experimental data.

composite materials that provides self-healing qualities to the spacecraft (in some sense, the composite material mimics the response of the human body to a wound inflicted on the skin). In currently available self-healing technologies, a microencapsulated healing-agent is embedded in a composite matrix containing a catalyst capable of polymerizing the healing agent [113]. A crack is formed in the material matrix wherever damage occurs. The crack ruptures the encapsulated microcapsules along the fracture plane, thereby releasing the healing agent into the crack plane through capillary action. When the healing agent contacts the catalyst, polymerization is initiated and the crack faces are thus bonded together.

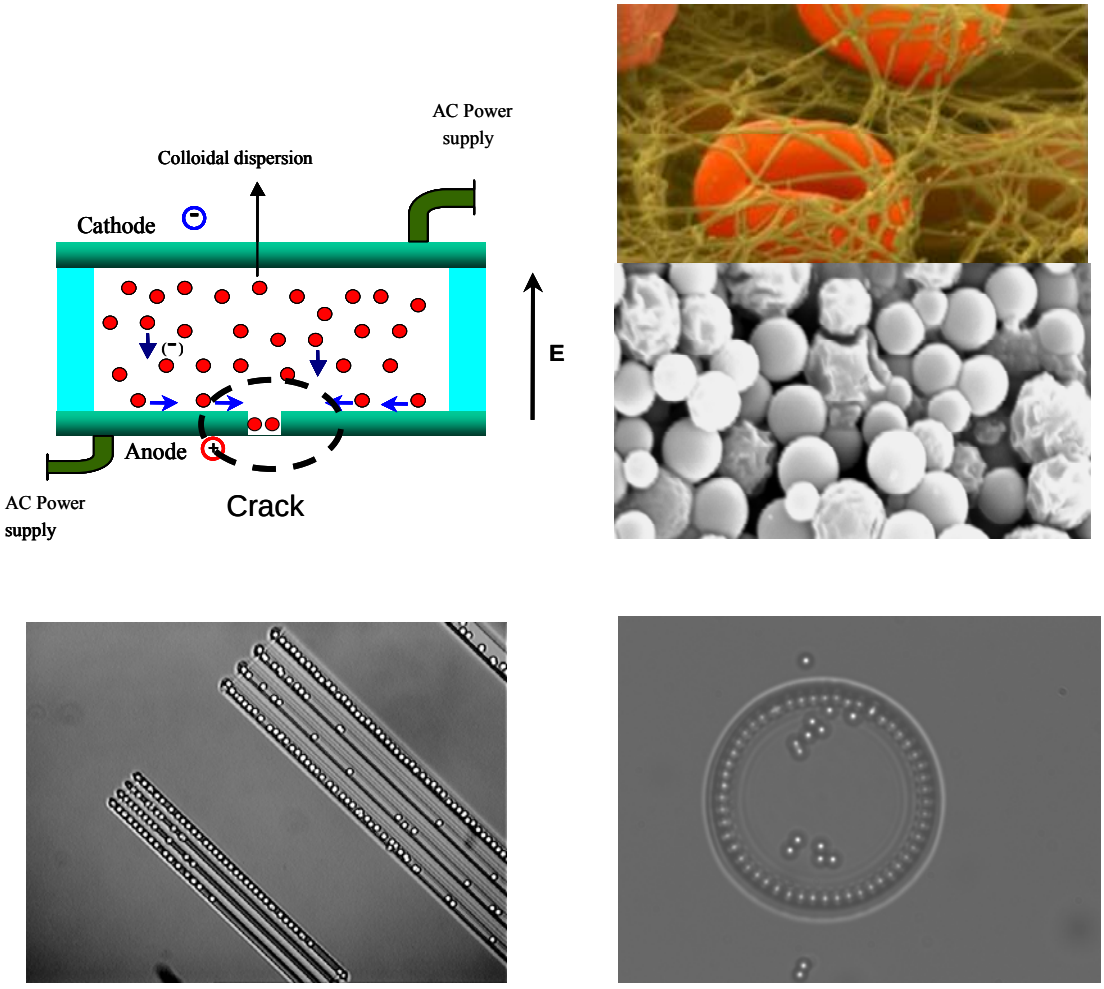

Figure 7.13. (a) Schematic of experimental set-up showing electrophoretic deposition of colloidal particles on scratched ITO electrodes (b) Functional encapsulated colloidal particles synthesized in Chapter 7 (bottom) can be used to mimic blood clotting action (top) at the site of the crack, (c,d) 4 μm colloidal particles assemble in 1 μm deep grooves patterned on photo-resist/ITO surfaces to mimic material cracks on application of applied electric fields.

This approach has several advantages: a) The technology for embedding microcapsules in polymers and making encapsulated microspheres (as described in this section) already exist and are widely used, b) The introduction of microspheres into the material matrix is not known to significantly alter the material properties. However, if there are no microspheres in the region of failure the crack continues to propagate into larger fissures. The challenge therefore is to homogeneously distribute the microspheres in the material matrix and engineer a mechanism that will enable the encapsulated microspheres to be transported to the site of the propagating crack. Also, the self healing efficiency depends on the concentration of the catalyst. It is also important for the microspheres to be weak enough to be ruptured by the growing crack.

Motivated by their potential importance, we would like to engineer self-healing materials that utilize the preferential nucleation of functional colloidal particles (embedded in the material matrix) near the region of a crack when an AC electric field is applied. The propagating crack will rupture the colloidal particles and release the encapsulated sealant (vitelline protein B) at the site of the crack and heal it. An experimental set-up similar to the design used by Trau et al.[12] shown in Fig. 7.13 (a) can be used to demonstrate the self-healing principle described above.

We would like to understand the mechanism of particle aggregation in the region of a crack, and use this understanding to quantify and improve self healing techniques based on this idea. As described earlier [12], the crack introduces a region of high current density and the colloidal particles tend to migrate towards regions of higher current density. We plan to experimentally investigate this effect by using patterned scratches

on electrode surfaces to mimic cracks in materials (Figs 7.13c and d). The scratch makes the electrode surface inhomogeneous. The colloidal particles are expected to preferentially aggregate in the inhomogeneous regions when an electric field is applied. In order to observe the deposition process and track the lateral migration of colloidal particles, we use optically transparent Indium tin oxide (ITO) electrodes coupled to an optical microscope. Conventional photolithography techniques were used to pattern rectangular and circular grooves on the ITO surface (Figs 7.13c and d). A PDMS spacer was used to separate the two ITO electrodes. Then, a colloidal suspension of 4 μm silica colloids was placed between the two parallel plate electrodes. The two electrodes are then connected to a function generator and an AC electric field was applied normal to the electrode surface. These preliminary experiments demonstrated the lateral transport of randomly distributed Brownian colloids towards and into the patterned grooves when 2.5 Vpp, 30 Hz electric field was applied.

We plan to conduct carefully planned experiments using the encapsulated colloidal particles synthesized in this section with the inhomogeneous ITO electrodes (Figs. 7.13c and d). The functional colloidal particles will contain a patented protein sealant/glue (vitelline protein B) encapsulated within BSA protein microspheres of different sizes. We will also monitor the particle trajectories when the electric field is applied to compute the characteristic transport rates (electrokinetic mobility). The experimental results of particle velocities will provide a better understanding of the flow physics as the particle approaches the scratch. The particle velocities are expected to

increase as it approaches the scratch because of increased current densities in the region of the crack.

Another potential use of this technique could be to direct colloidal paint droplets towards a scratch on painted micro-surfaces. Also, fluorescent colloidal particles can be directed towards the region of defect to highlight regions of scratch or failure in materials. In summary, this proposed future work aims to:

- **engineer self-healing materials using encapsulated colloids** that can be transported to the site of a propagating crack when an external AC electric field is applied

7.6. Conclusions

A water-in-oil emulsion technique was used to prepare BSA based microspheres with a wide range of sizes (1-10 μm). A correlation, given by Eq. (7.7) with $c_1 = 0.0206$ and $\alpha = -0.53$, was developed based on the theory of turbulent dispersions, and validated by comparisons with experimental results for a wide range of We_m. The exponent α deviated from the classical value of α=-0.6. The correlation is valid for non-coalescing dispersions with a dilute dispersed phase alone. The uniformity of the BSA microsphere size distributions was found to increase with stirring speed. However, increasing the stirring speed beyond N=1200 rpm did not considerably reduce the spread of the size distribution.

The average size of the BSA microspheres was doubled with the addition of a 0.015% v/v aqueous solution of Vitelline protein B (vpB) to the dispersed phase. The addition of vpB also significantly altered the size distribution of the BSA microspheres, resulting in microspheres with a wider distribution when compared with the microspheres without vpB.

A Rosin-Rammler distribution function was found to accurately represent the BSA microsphere distribution data. With a better understanding of the physics of microsphere formation and with the present correlation, it is now possible to provide a good estimate of the average sphere size of colloidal particles synthesized using emulsion-polymerization prior to microsphere preparation. This knowledge is necessary to produce microspheres of a specified average diameter and size distribution, key for controlled drug release kinetics. Development of novel engineering applications for these encapsulated microspheres, besides its application in the pharmaceutical industry for drug delivery, is planned for future work. In particular, these functional colloidal particles encapsulated with vPB can be actively manipulated using external electric fields to engineer self-healing materials that mimic blood clotting.

8. CONCLUSIONS

8.1. Summary of Conclusions

A prerequisite to assembling nano- and micro- scale particles into ordered structures and controllable devices is the ability to sensitively measure and manipulate colloidal interactions on the order of thermal energy, kT. The work in this dissertation explores two basic paradigms for manipulating colloidal particles: self- and directed-assembly. Self-assembly of colloidal particles was achieved by patterning synthetic energy landscapes on substrates while directed assembly was realized using external electric fields. The ultimate goal of this research is to provide robust engineering solutions for manipulating particle structure in materials and device applications. With this goal in mind, this dissertation addressed the following issues 1) develop fundamental measurements and models for equilibrium self-assembly on energy landscapes that directly connect interfacial colloidal interactions, dynamics and structure to energy landscape features, 2) constructively combine electric fields with energy landscapes to manipulate colloidal configurations and anneal/ orient colloidal structures, 3) identify connections between colloidal microstructure, electrokinetic transport mechanisms, and electrical impedance properties to design and control nanoparticle based integrated micro- fluidic and electronic devices, and 4) synthesize functional colloidal particles that can be manipulated using external fields to engineer multi-functional materials. The significant conclusions from this work are summarized below:

- A conceptually new approach to sensitively image energy landscapes on physically and chemically patterned surfaces was demonstrated. This new imaging paradigm exploits Brownian probes to naturally interrogate interactions on the order of the thermal energy kT and thus overcomes inherent mechanical limitations in scanning probe methods [49,50]. Because we monitor particle excursions in concentrated colloidal fluids, images of potential energy landscapes were obtained via an inverse Monte Carlo analysis that interpret equilibrium colloidal distributions as three dimensional position dependent potentials due to conservative forces and rigorously connects particle-pattern, particle-particle, and particle-field interactions to interfacial structures. For comparison, inversion of measured distributions with Boltzmann's equation provided the particle-surface interaction in the presence of many-body packing effects to produce free energy landscapes. These images quantitatively capture colloidal interactions, dynamics, and structure on patterned surfaces, which provides essential information to design, control, and optimize template directed colloidal self-assembly processes. The experiments in Section 4 have imaged height contours on lithographically patterned glass surfaces that display quantitative agreement with Atomic Force Microscopy surface images. Colloidal probe concentration was also varied to investigate image resolution and acquisition times associated with this technique. These findings should benefit a broad interdisciplinary audience based on applications of Brownian probes to imaging multiscale and multidimensional surfaces in synthetic and biomolecular systems.

- A consistent analysis of self-diffusion in inhomogeneous fluids of concentrated diffusing colloidal probes on energy landscapes was developed. This is important to the temporal imaging process and to self-assembly kinetics. A simple expression for self-diffusion of DCP on landscape features was derived in Section 4 that captures the combined effects of multi-body hydrodynamic interactions, particle escape rates from free energy wells, and cooperative rearrangements associated with particles moving through their coordination shell. This expression accurately predicts the long-time self-diffusion coefficient from the measured short-time diffusion coefficient and free-energy well for different average colloidal particle concentrations. In addition, the expression for D_S^L is also accurate for limiting cases including infinite dilution on patterned surfaces and all sub-monolayer fluid concentrations on homogeneous surfaces. To further demonstrate a consistent analysis of how energy landscapes modulate DCP dynamics, measured density fluctuations were compared with 2D GCMC simulated fluctuations, and an excellent agreement was obtained. The ability to describe inhomogeneous colloidal fluid microstructural dynamics on energy landscapes using the new theoretical framework described in Section 4 builds on previous studies investigating colloidal dynamics in equilibrium transitions[114,115], in non-equilibrium transitions[27,116], and in sub-3D confinement[117].

- In Section 5, we have demonstrated the use of normal external electric fields to tune the interactions between colloidal particles and control assembly into ordered structures on homogeneous and patterned electrodes. The nature of the colloidal

interactions was found to be sensitive to the strength, frequency of the AC field and the electrolyte used. Cycling the AC field frequencies was found to be an effective way to anneal equilibrium colloidal configurations. We also observed the preferential assembly of colloidal particles in energy landscape features made on the electrode surface when an AC field was applied. The results from this work suggest a general strategy to integrate self- and directed- assembly methods as a means to control nano- and micro- particle structure formation and orientation.

- In Section 6, we have demonstrated the ability to tune the directed assembly of different nanoparticle configurations within the gap of coplanar micro-electrode/fluidic devices via several electrokinetic transport mechanisms. Quantitative predictions of dominant transport mechanisms as a function of AC electric field amplitude and frequency were consistent with steady-state microstructures of nanoparticles within electrode gaps observed using video microscopy. The electrical impedance spectra associated with each nanoparticle configuration was measured and modeled using representative equivalent circuits that accounted for the entire measurement system (including parasitics, the function generator, etc.) and isolated the contribution of the assembled structures from the system impedance. In particular, a functional electrical switch using colloidal particles was realized by reversibly forming and breaking colloidal wires between electrode gaps. The resistance of the switch in the OFF and ON states was 29 kΩ and 2 Ω respectively, which translates to three orders of magnitude change in an electrical property achieved via colloidal assembly. These models and more

importantly, this methodology, can then be applied directly to the design of multi-functional and reconfigurable devices that use colloidal materials to tune electrical properties.

- In Section 7, a water-in-oil emulsion technique was used to prepare BSA based encapsulated colloids with a wide range of sizes (1-10 μm). A fluid-mechanics based correlation inspired by the theory of turbulent dispersions was developed to predict the average particle size obtained as a function of stirring speed. The uniformity of the BSA microsphere size distributions was found to increase with stirring speed. The average size of the BSA microspheres was doubled with the addition of a 0.015% v/v aqueous solution of a patented adhesive/sealant Vitelline protein B (vpB) to the dispersed phase. A Rosin-Rammler empirical distribution function was found to accurately represent the BSA microsphere distribution data. With a better understanding of the physics of microsphere formation and with the present correlation, it is now possible to accurately predict the average size of colloidal particles synthesized using emulsion-polymerization. These functional colloidal particles encapsulated with vPB can be manipulated using external electric fields to engineer self-healing materials as described in Section 7.

9. FUTURE RESEARCH

9.1. Synopsis

This section briefly summarizes current and future work not presented as part of this dissertation. The ideas discussed below are closely related to Sections 4-7 and are in tune with the central research theme of intelligently combining energy landscapes, external electric fields and different particle-particle interaction potentials to engineer defect free patterned colloidal crystals and multifunctional materials.

9.2. Imaging Chemical Patterns Using Diffusing Colloidal Probes

Results presented in Section 4 of this dissertation included experimental measurements and theoretical models to understand the quantitative connections between colloidal interactions and microstructure in quasi-2D inhomogeneous colloidal fluids. Understanding equilibrium structure of colloidal fluids adjacent to homogeneous and patterned surfaces provides a basis to intelligently tune colloidal and external potentials to reversibly control interfacial colloidal crystallization from fluids near surfaces. Having successfully demonstrated the use of DCP to image physically patterned surfaces, an obvious extension of this work would be to use diffusing colloids as probes of energy landscapes associated with chemical templates.

Chemically patterned substrates can also be used to modulate colloidal assembly, quite like the physical patterns used in Section 4. Thermodynamically, the pattern introduces the colloidal dispersion to a free energy landscape, which creates density

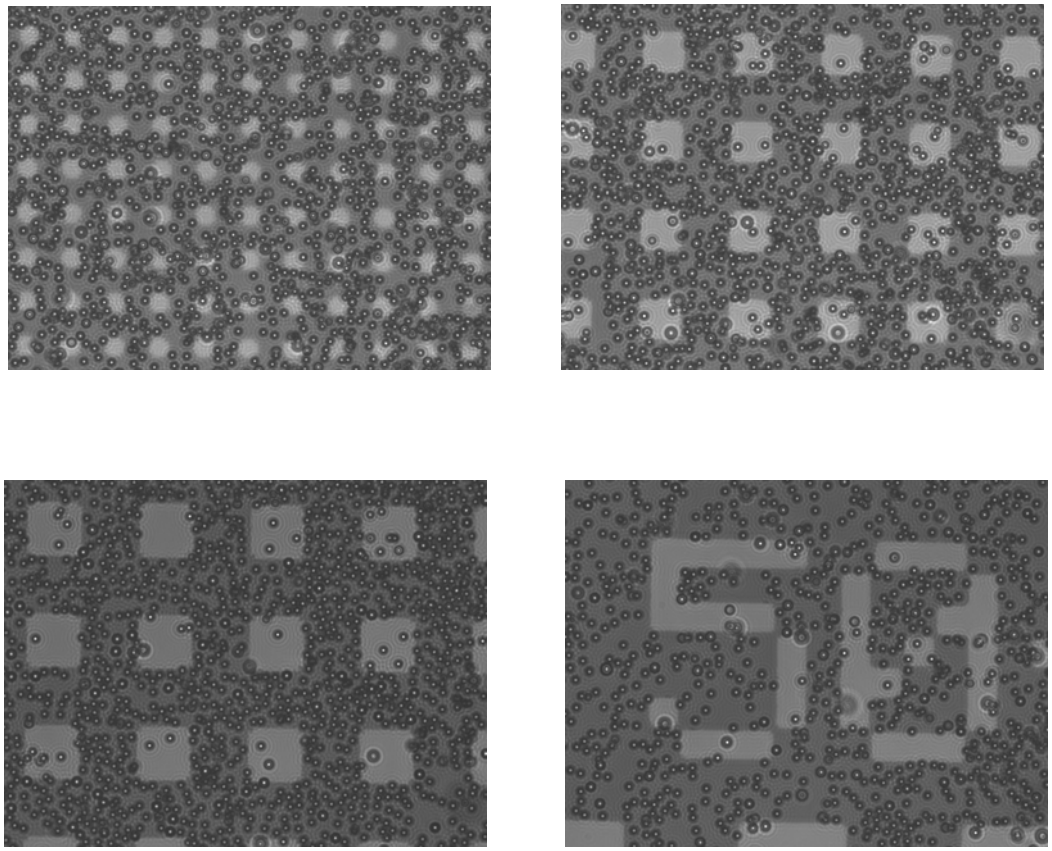

Figure 9.1. Lateral density variations in interfacial colloidal fluid of 4 μm PS particles on chemically patterned substrates. The lighter regions correspond to glass and the darker regions correspond to a 10 nm Au film vapor deposited on the glass substrate through a photomask.

gradients in the lateral direction. Preliminary results have been obtained for chemical potential energy landscapes produced by patterning 10nm Au films on SiO_2 surfaces (Fig. 9.1) to produce van der Waals energy wells mimicking the physical landscapes used in this dissertation. The glass slide and gold surfaces were rendered hydrophobic with octadecyltrimethylchlorsilane[118] and thiol respectively, followed by subsequent adsorption of PEO-PPO-PEO brushes onto the substrate and a colloidal dispersion containing 4 μm PS colloids to sterically stabilize the system. The colloidal particles were suspended in a 0.4 M NaCl ionic solution so that the electrostatic interactions are essentially screened. The only appreciable interactions to consider in this work are the van der Waals interactions between the colloidal particles and the underlying substrate and the hard-wall introduced by the interpenetration and compression of the macromolecular layers.

The equilibrium partitioning of colloids seen in Fig. 9.1 is dictated by the higher PS-Au van der Waals interaction compared to PS-glass, and to the first approximation can be determined using Boltzmann's equation. Following the general methodology presented in Section 4 to analyze inhomogeneous colloidal fluids, we will monitor the Brownian trajectories of the DCP over the chemically patterned substrate to construct a two-dimensional equilibrium density distribution function. In contrast to the experimental results presented in Section 4, the potential energy landscape *u(x,y)* in this case does not correspond to a spatially varying surface topography. Instead, *u(x,y)* corresponds to a position dependent van der Waals attractive energy wells associated

with the gold and the glass substrate. The inverse Monte Carlo algorithm developed in Section 4 needs to be modified to iteratively tune the van der Waals interaction potential at every spatial position until the simulated density distribution matches the measured equilibrium distribution function. We also plan to investigate how particle-particle and varying particle-wall interaction affects the lateral self-diffusion of the inhomogeneous colloidal fluid. In particular, we would like to test the expression for self-diffusion of DCP on physical landscape features developed in this dissertation to analyze the dynamics of colloidal particles diffusing above the chemically patterned substrate in Fig. 9.1. This expression accounts for the combined effects of multi-body hydrodynamic interactions and the particle escape rates from the free-energy wells associated with the chemical pattern. The successful completion of this work in the future will conclusively demonstrate the use of statistical mechanical analyses to quantitatively explain equilibrium density variations and self-diffusion in quasi 2D colloidal fluids on physicochemical patterned surfaces. In summary, this proposed future work aims to:

- **use chemically patterned substrates to modulate quasi 2D local density** via free energy landscapes leading to crystallization in interfacial colloidal fluids
- **quantitatively image chemical patterns on surfaces and explain self-diffusion** using the general statistical mechanics framework described in Section 4 to analyze inhomogeneous colloidal fluids

9.3. Thermodynamic Control of 2D Colloidal Crystallization

It is important to understand how particle-particle interactions, homogeneous surfaces, and gravity are connected to 2D interfacial colloidal fluid and crystal microstructures and dynamic transitions between them. In the following, experimental tasks are described that use optical microscopy techniques to investigate in-situ the 2D fluid-crystal coexistence and crystallization dynamics over homogeneous substrates. The thermodynamics and kinetics of 2D crystallization on surfaces will be investigated with the intention of using a large 2D ordered domain as a template for inhomogeneous 3D interfacial crystallization.

Experiments will use hydrophobically modified silica or PS colloids with adsorbed copolymer and unadsorbed polymers, micelles, or nanoparticles to tune both van der Waals and depletion attraction and 2D crystallization (see Fig 9.2). This experimental system in effect integrates two model potentials extensively characterized in the literature in terms of pair interactions and phase behavior (see Fig 9.2 and refs[119-122]). We plan to use micron sized fluorescent silica colloids (fluorescent core-shell and core-fluorescent shell, Fig 9.3)[123,124], which can be used in both 2D video microscopy and 3D confocal microscopy. Silica colloid and glass slide surfaces will be rendered hydrophobic with octadecanol[125] and octadecyltrimethylchlorsilane[118] followed by subsequent adsorption of PEO-PPO-PEO brushes that can be tuned to modulate the short range van der Waals potential. However, because such short range van der Waals potentials are known to often produce dynamic arrest,[126] the proposed work aims to superimpose an additional, longer range depletion potential, which is well documented

in the literature and our preliminary work (Figs 9.2, 9.3) to produce crystals with less kinetic arrest problems.[127,128] Preliminary results demonstrate our ability to form crystals in quasi-2D systems next to homogeneous surfaces (Figs 9.2, 9.3) using 2.2 and 1.4 μm silica colloids with sodium dodecyl sulfate (SDS) micellar depletants. Previous studies have investigated depletion crystallization of bulk colloidal fluids on wall surfaces[127,128] and anomalous interactions in confined gaps,[129] but none have investigated homogenous quasi 2D crystallization near a single wall (and with superimposed short range van der Waals potential). A significant portion of the future work will focus on identifying interfacial crystallization conditions (Fig 9.2), measuring particle and surface interactions, and quantifying dynamics associated with structural transitions and freezing/melting.

One additional aspect to be explored in greater detail as part of this objective is to understand how the particle-wall potential affects 2D crystallization. This aspect of the work has not been systematically addressed in the literature thus far. Part of this effort will focus on decoupling particle-wall and particle-particle van der Waals attraction via adsorption of thicker layers on the wall[130]. (In contrast, the role of naturally greater colloid-surface depletion attraction[45] on 2D crystallization will simply be documented.) This objective will explore a potentially useful preliminary result where increased colloid-surface van der Waals attraction modulated by interfacial gold films has been observed to affect 2D depletion crystals of 1.4 μm colloids: hexagonal domains form on bare glass and gold films < ~20nm and square domains form on gold films > ~20nm (Fig. 9.3). We believe that the particle-surface van der Waals interactions influence the

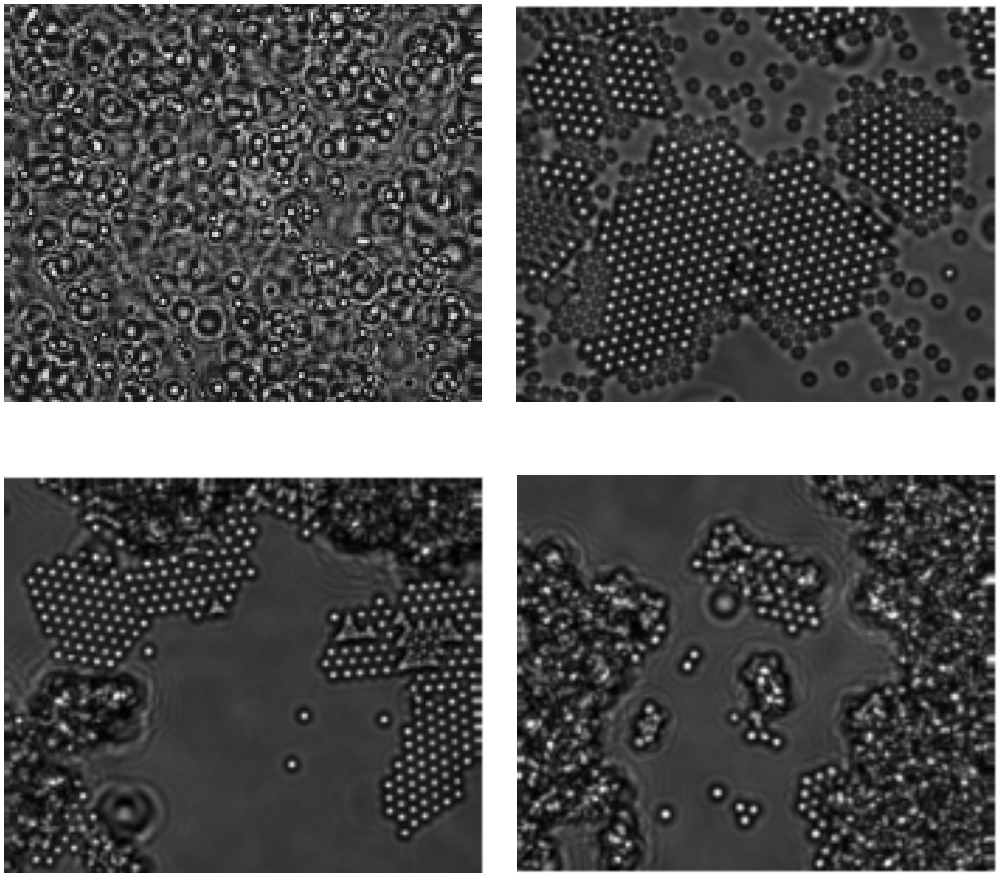

Figure 9.2. (Top-bottom, left-right) Transmitted light CCD images of levitated quasi 2D phase behavior of 1 micron PS colloids stabilized with F108 interacting via micellar (SDS micelles at room temperature) mediated depletion potentials with fluid, fluid-solid, solid-gel, and gel microstructures.

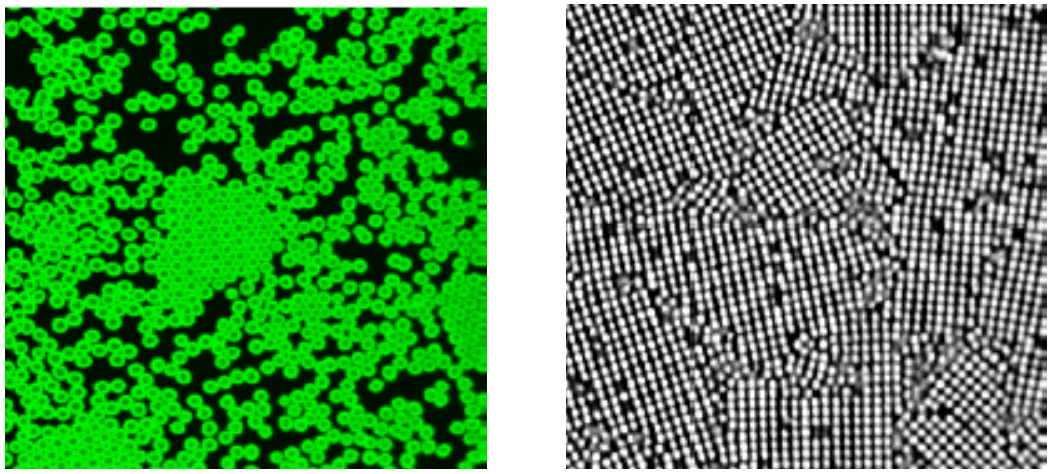

Figure 9.3. (a) Fluorescent shell-core colloids (1.4 μm) interacting via SDS mediated depletion forces for quasi 2D video microscopy and 3D confocal microscopy and, (b) square domain crystals on >20nm gold films due to formation of higher energy FCC face on attractive substrate.

interfacial energies associated with how different crystal planes wet the surface. This is a potentially powerful method to produce stacking fault free FCC crystals grown from 100 faces due to interfacial wetting effects[131,132] instead of microfabricated templates[1,4,133]. In summary, this proposed future work aims to:

- **understand the equilibrium 2D crystallization on $Si0_2$ and Au surfaces** due to van der Waals and micellar mediated depletion interactions
- **control reversible 2D crystallization via tunable** van der Waals and depletion potentials to thermodynamically anneal and quench square and hexagonal crystals

9.4. Kinetic Control of 2D Attractive Colloidal Crystals Using AC Fields

In this dissertation, directed colloidal assembly using external AC fields (Section 5 and 6) has been discussed in the context of electrostatically stabilized systems where the inter-particle interaction potential is purely repulsive. As part of our future work, we plan to couple AC electric fields and attractive particle-particle interactions due to depletion forces to effectively orient and anneal 2D colloidal crystals. This will allow us to overcome 1) melting away of ordered colloidal domains formed in Section 5 when the external electric field is turned off and, 3) formation of polycrystalline domains and defects in colloidal crystals formed with depletion interactions (Fig 9.2). As the depletion studies described earlier are carried out at high ionic strengths, the electrophoretic transport/manipulation of colloidal particles is challenging due to sufficiently reduced mobilities as a consequence of charge screening. However, active manipulation of colloidal particles at high ionic strengths (high solution conductivity) is possible with dielectrophoresis, which is based on the polarization of colloidal particles in a non-uniform electric field as described in Section 6, and will be adapted to this study. The scaling analysis developed in Section 6 will be used to identify regions in the voltage-frequency phase space where dielectrophoresis is the dominant mode of transport.

To constructively contribute to 2D crystallization rather than melting existing crystals, it will be necessary to investigate a range of AC field amplitudes and frequencies that produce different characteristic particle displacements and transport rates and possibly cycle between these states. Although the correspondence between 2D

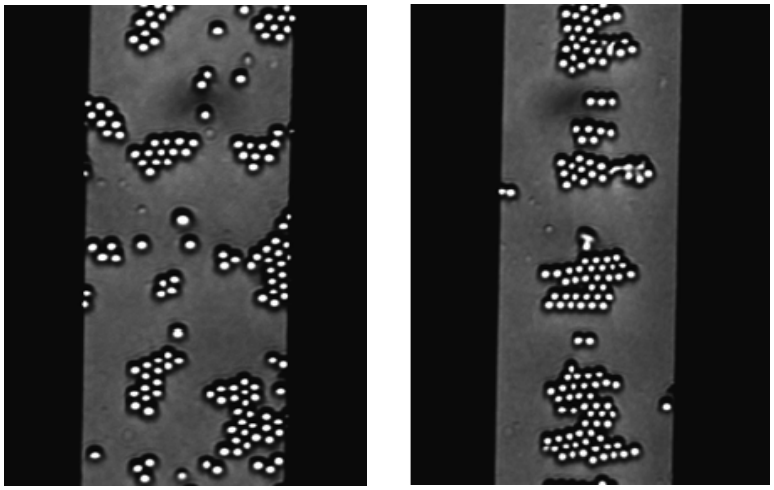

Figure 9.4. Depletion crystals of 2.2 μm SiO2 colloids between gold film electrodes with (top) no applied field, and (bottom) 2.5V-1MHz AC field resulting in crystal alignment with field via dielectrophoretic forces.

crystals formed via depletion interactions in Figs 9.2, 9.3 and via AC electric fields in Section 5 suggest obvious conditions where enhanced 2D crystallization might be observed, their optimal constructive interplay will be analyzed in terms of a Peclet number characterized by the relative field driven transport rate and Brownian rate (including hydrodynamic interactions[60,134]) within fluid and crystal phases. Attempts to anneal pre-existing depletion/van der Waals crystals will use AC electric fields that modulate effective particle and surface potentials from repulsive to attractive depending on frequency and electrolyte.[72]

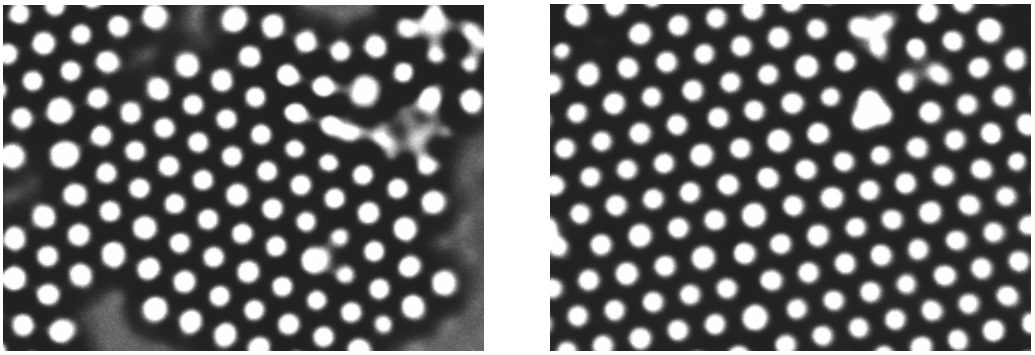

Figure 9.5. Depletion crystals of 2.2 μm SiO2 colloids between gold film electrodes with (top) no applied field, and (bottom) 2.5V-1MHz AC field resulting in an annealed hcp colloidal crystal.

Lateral AC electric fields produced via thin gold films on either side of a bare glass surface region[135] will also be investigated primarily for the purpose of annealing crystals but also with the aim of orienting 2D crystals. In preliminary results (Figs 9.4, 9.5), 2.2 μm SiO2 particles levitated above glass between gold electrode films have been shown to display various modes of transport due to electrophoretic, AC electro-osmotic, and dielectrophoretic forces, which produce a variety of structures and dynamic responses. Lateral fields will be investigated to use oscillatory electrophoretic motion to anneal polycrystalline structures (Fig 9.5a) and to use dielectrophoretic forces to form linear precursors to oriented, single domain crystals or square lattice structures (Figs 9.4, 9.5b). Improvement in ordering of the colloidal crystal with electric field assisted annealing will be monitored by tracking the bond order correlation function, which is sensitive to local defects and polycrystallinity. This is the most exploratory task in this future work with the aim of understanding how various field configurations and

transport mechanisms might be used to enhance formation of attractive 2D crystals. In summary this proposed objective aims to:

- **employ AC electrophoretic assembly of metastable crystals** on Au electrodes to manipulate pre-crystallization and depletion pathways in depletion crystals
- **investigate AC electrophoretic and dielectrophoretic forces** normal/parallel to surface for mechanical annealing and orientational control of 2D crystallites

9.5. Attraction Driven Colloidal Crystallization on Patterned Substrates

The final objective of the proposed future research is to use depletion mediated attractive colloidal interactions and potential energy landscape due to the underlying patterned substrates to induce the formation of robust, defect free patterned colloidal crystals. By carefully tuning the particle-particle and particle-wall interactions (in effect modifying the free-energy landscape), we plan to pattern colloidal crystals on physical templates with arbitrary geometry, and on attractive patches on chemically modified substrates. The ability to engineer patterned colloidal crystals has immediate applications in nanophotonics as optical waveguides.

We performed preliminary experiments over physically and chemically patterned substrates using 1.4 μm SiO_2 colloids at SDS depletant concentrations lower than the value required for crystallization over homogeneous substrates (Fig 9.6). We observe a crystalline phase within a pattern and a fluid-phase in the region outside the pattern. This was also observed in MC simulations performed with measured depletion inter-

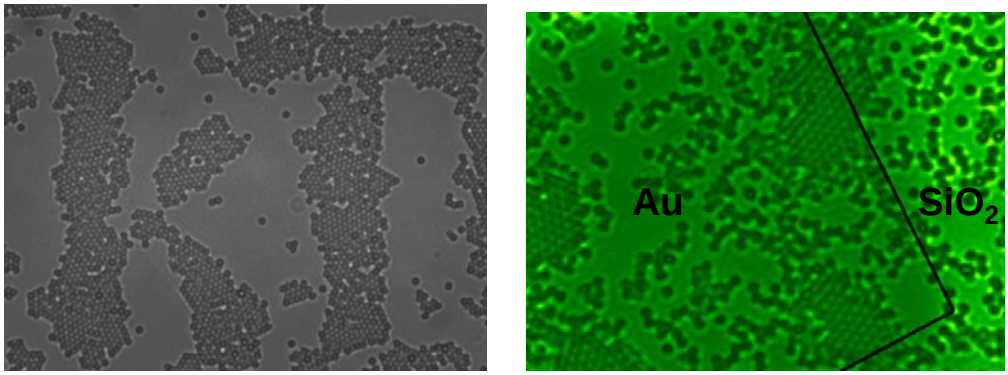

Figure 9.6. Colloidal crystals formed on physical patterns (a) and chemical patterns (b) using depletion driven attractive particle interactions.

particle potentials. This encouraging preliminary results calls for a more systematic analysis where the particle-particle and particle-wall interactions are carefully varied to identify conditions where a crystal phase within the pattern co-exists with a fluid phase outside it.

Physical patterns on glass substrates comprising of a periodic array of harmonic wells were fabricated as described in Section 3. Au films (chemical patterns) in Figure 9.6 were patterned on glass microscope slides by metal evaporation using TEM grids as masks. The thickness of gold will be varied to obtain the particle-wall van der Waals interaction required. In summary, we plan to

- **extend the depletion attraction driven interfacial crystallization studies to patterned substrates** by studying interfacial phase behavior driven by a combination of short-range particle-particle and particle-substrate attractions and potential energy landscapes provided by the underlying template.

- **use MC simulations of 2D attractive colloidal fluids over patterned substrates** to guide further experiments aimed at growing patterned attractive colloidal crystals.

REFERENCES

[1] A. van Blaaderen, R. Ruel, and P. Wiltzius, Nature **385** (23), 321 (1997).

[2] G. M. Whitesides and B. Grzybowski, Science **295**, 2418 (2002).

[3] J. Aizenberg, P. V. Braun, and P. Wiltzius, Physical Review Letters **84** (13), 2997 (2000).

[4] W. Lee, A. Chan, M. A. Bevan, J. A. Lewis, and P. V. Braun, Langmuir **20** (12), 5262 (2004).

[5] Y. A. Vlasov, X.-Z. Bo, J. C. Sturm, and D. J. Norris, Nature **414**, 289 (2001).

[6] P. Jiang, J. F. Bertone, K. S. Hwang, and V. L. Colvin, Chemistry of Materials **11** (8), 2132 (1999).

[7] A. P. Gast and W. B. Russel, Phys. Today **51** (12), 24 (1998).

[8] K.-H. Lin, J. C. Crocker, V. Prasad, A. Schofield, D. A. Weitz, T. C. Lubensky, and A. G. Yodh, Phys. Rev. Lett. **85** (8), 1770 (2000).

[9] X. M. Zhao, Y. N. Xia, and G. M. Whitesides, Journal of Materials Chemistry **7** (7), 1069 (1997).

[10] Y. Sun and G. C. Walker, J. Phys. Chem. B **106**, 2217 (2002).

[11] Z. Cheng, W. B. Russel, and P. M. Chaikin, Nature **401**, 893 (1999).

[12] M. Trau, S. Sankaran, D. A. Saville, and I. A. Aksay, Nature **374** (6521), 437 (1995).

[13] T. Gong and D. W. M. Marr, Langmuir **17** (8), 2301 (2001).

[14] S. Yamamuro, D. F. Farrell, and S. A. Majetich, Physcial Review B **65**, 224431 (2002).

[15] C. Mio and D. W. M. Marr, Advanced Materials **12** (12), 917 (2000).

[16] P. Korda, G. C. Spalding, E. R. Dufresne, and D. G. Grier, Rev. Sci. Instr. **73**, 1956 (2002).

[17] M. M. Burns, J.-M. Fournier, and J. A. Golovchenko, Science **249**, 749 (1990).

[18] S. H. Park and Y. Xia, Langmuir **15**, 266 (1999).

[19] B. J. Ackerson and N. A. Clark, Phys. Rev. A **30** (2), 906 (1984).

[20] W. B. Russel, D. A. Saville, and W. R. Schowalter, *Colloidal Dispersions*. (Cambridge University Press, New York, 1989).

[21] D. C. Prieve, Adv. Colloid Interface Sci. **82**, 93 (1999).

[22] J. C. Crocker and D. G. Grier, J. Colloid. Interface Sci. **179**, 298 (1996).

[23] D. Frenkel and B. Smit, *Understanding Molecular Simulation: From Algorithms to Applications*, 2nd ed. (Academic Press, San Diego, CA, 2002).

[24] M. P. Allen and D. J. Tildesley, *Computer Simulation of Liquids*. (Oxford Science, New York, 1987).

[25] P. N. Pusey, *Liquids, Freezing, and Glass Transitions*. (Elsevier, Amsterdam, 1991).

[26] J. C. Crocker and D. G. Grier, Phys. Rev. Lett. **73** (2), 352 (1994).

[27] E. R. Weeks, J. C. Crocker, A. C. Levitt, A. Schofield, and D. A. Weitz, Science **287**, 627 (2000).

[28] J. A. Lewis, J. Am. Ceram. Soc **83** (10), 2341 (2000).

[29] B. Balzer, M. K. M. Hruschka, and L. J. Gauckler, J. Colloid. Interfac. Sci. **216**, 379 (1999).

[30] M. Cloitre, R. Borrega, F. Monti, and L. Leibler, Phys. Rev. Lett. **90** (6), 068303 (2003).

[31] A. F. Routh and W. B. Russel, Langmuir **15**, 7762 (1999).

[32] B. J. Ash, L. S. Schadler, and R. W. Siegel, Materials Letters **55**, 83 (2002).

[33] C. F. Zukoski, Chemical Engineering Science **50** (24), 4073 (1995).

[34] A. M. Kulkarni and C. F. Zukoski, Langmuir **18** (8), 3090 (2002).

[35] J. H. Holtz and S. A. Asher, Nature **389**, 829 (1997).

[36] G. S. Pan, R. Kesavamoorthy, and S. A. Asher, Phys. Rev. Lett. **78** (20), 3860 (1997).

[37] E. Yablonovitch, Physical Review Letters **58**, 2059 (1987).

[38] E. M. Lifshitz, J. Exp. Theor. Phys. USSR **29**, 94 (1955).

[39] I. E. Dzaloshinskii, E. M. Lifshitz, and L. P. Pitaerskii, Adv. Phys. **10**, 165 (1961).

[40] M. A. Bevan and D. C. Prieve, Langmuir **15** (23), 7925 (1999).

[41] V. A. Parsegian and G. H. Weiss, J. Colloid Interface Sci. **81**, 285 (1981).

[42] B. A. Pailthorpe and W. B. Russel, J. Colloid Interface Sci. **89** (2), 563 (1982).

[43] S. Asakura and F. Oosawa, J. Chem. Phys. **22**, 1255 (1954).

[44] A. Vrij, Pure and Appl. Chem. **48**, 471 (1976).

[45] D. L. Sober and J. Y. Walz, Langmuir **11** (7), 2352 (1995).

[46] H. J. Wu and M. A. Bevan, Langmuir **21** (4), 1244 (2005).

[47] D. C. Prieve, F. Luo, and F. Lanni, Faraday Disc. **83**, 297 (1987).

[48] H. Chew, D. S. Wang, and M. Kerker, Applied Optics **18**, 2679 (1979).

[49] G. Binnig, C. F. Quate, and C. Gerber, Phys. Rev. Lett. **56** (9), 930 (1986).

[50] W. A. Ducker, T. J. Senden, and R. M. Pashley, Nature **353** (6341), 239 (1991).

[51] J. K. H. Horber and M. J. Miles, Science **302**, 1002 (2003).

[52] C. D. Frisbie, L. F. Rozsnyai, A. Noy, M. S. Wrighton, D. V. Vezenov, and C. M. Lieber, Science **265** (5181), 2071 (1994).

[53] E. Kokkoli and C. F. Zukoski, Langmuir **17**, 369 (2001).

[54] K.-B. Lee, S.-J. Park, C. A. Mirkin, J. C. Smith, and M. Mrksich, Science **295**, 1702 (2002).

[55] L. T. Mazzola, C. W. Frank, S. P. A. Fodor, C. Mosher, R. Lartius, and E. Henderson, Biophysical Journal **76**, 2922 (1999).

[56] M. Patra and P. Linse, Nano Lett. **6** (1), 133 (2006).

[57] H.-J. Wu, T. O. Pangburn, R. E. Beckham, and M. A. Bevan, Langmuir **21** (22), 9879 (2005).

[58] J. Baumgartl and C. Bechinger, Europhys. Lett. **71**, 487 (2005).

[59] T. O. Pangburn and M. A. Bevan, J. Chem. Phys. **123**, 174904 (2005).

[60] S. Anekal and M. A. Bevan, J. Chem. Phys. **125**, 034906 (2006).

[61] J. F. Brady, J. Fluid Mech. **272**, 109 (1994).

[62] H. Eyring, J. Chem. Phys. **4**, 283 (1936).

[63] M. Baus and J. L. Colot, Phys. Rev. A **36** (8), 3912 (1987).

[64] F. L. Roman, J. A. White, and S. Velasco, Europhys. Lett. **42** (4), 371 (1998).

[65] P. Richetti, J. Prost, and P. Barois, Journal De Physique Lettres **45** (23), 1137 (1984).

[66] M. Bohmer, Langmuir **12** (24), 5747 (1996).

[67] M. Trau, D. A. Saville, and I. A. Aksay, Langmuir **13** (24) (1997).

[68] F. Nadal, B. Pouligny, C. Ybert, A. Ajdari, and F. Argoul, Abstracts of Papers of the American Chemical Society **224**, U432 (2002).

[69] W. D. Ristenpart, I. A. Aksay, and D. A. Saville, Physical Review E **69** (2) (2004).

[70] Y. Solomentsev, M. Bohmer, and J. L. Anderson, Langmuir **13** (23), 6058 (1997).

[71] S. A. Guelcher, M. A. Bevan, Y. Solomentsev, and J. L. Anderson, Langmuir **16** (24), 9208 (2000).

[72] J. A. Fagan, P. J. Sides, and D. C. Prieve, Langmuir **21** (5), 1784 (2005).

[73] J. A. Fagan, P. J. Sides, and D. C. Prieve, Langmuir **22** (24), 9846 (2006).

[74] T. M. Squires, J. Fluid Mech. **443**, 403 (2001).

[75] P. J. Sides, Langmuir **17** (19), 5791 (2001).

[76] M. Schmidt, M. Dijkstra, and J.-P. Hansen, J. Phys.: Condens. Matter **16**, S4185–S4194 (2004).

[77] R. S. Saksena and L. V. Woodcock, J. Chem. Phys. **122**, 164501 (2005).

[78] R. W. O'Brien, D. W. Cannon, and W. N. Rowlands, J. Colloid Interface Sci. **173**, 406 (1995).

[79] T. C. Halsey, Science **258** (5083), 761 (1992).

[80] H. Morgan, M. P. Hughes, and N. G. Green, Biophys. J. **77**, 516 (1999).

[81] R. Krupke, F. Hennrich, H. v. Löhneysen, and M. M. Kappes, Science **301** (5631), 344 (2003).

[82] B. Comiskey, J. D. Albert, H. Yoshizawa, and J. Jacobson, Nature **394**, 253 (1998).

[83] A. Yethiraj and A. v. Blaaderen, Nature **421**, 513 (2003).

[84] K. Hermanson, S. Lumsdon, J. Williams, E. Kaler, and O. Velev, Science **294**, 1082 (2001).

[85] H.-J. Wu, W. N. Everett, S. G. Anekal, and M. A. Bevan, Langmuir **22**, 6826 (2006).

[86] E. M. Furst and A. P. Gast, Phys. Rev. E **62** (5), 6916 (2000).

[87] A. Castellanos, A. Ramos, A. Gonzalez, N. G. Green, and H. Morgan, J. Phys. D: Appl. Phys. **36**, 2584–2597 (2003).

[88] R. J. Hunter, *Zeta Potential in Colloid Science: Principles and Applications*. (Academic Press, New York, 1981).

[89] R. W. Obrien, Journal of Fluid Mechanics **190**, 71 (1988).

[90] T. B. Jones, *Electromechanics of Particles*. (Cambridge University Press, Cambridge, 1995).

[91] J. Wu, Y. Ben, D. Battigelli, and H.-C. Chang, Ind. Eng. Chem. Res. **44**, 2815 (2005).

[92] P. A. Smith, C. D. Nordquist, T. N. Jackson, T. S. Mayer, B. R. Martin, J. Mbindyo, and T. E. Mallouk, Appl. Phys. Lett. **77** (9), 1399 (2000).

[93] F. Carrique, F. J. Arroyo, M. L. Jimenez, and A. V. Delgado, J. Chem. Phys. **118**, 1945 (2003).

[94] M. N. V. R. Kumar, Journal of Pharmacy and Pharmaceutical Sciences **3** (2), 234 (2000).

[95] F. Kratz, I. Fichtner, U. Beyer, P. Schumacher, T. Roth, H. H. Fiebig, and C. Unger, European Journal of Cancer **33**, 784 (1997).

[96] Y. Matsumura and H. Maeda, Cancer Research **46** (12), 6387 (1986).

[97] Y. Takakura, T. Fujita, M. Hashida, and H. Sezaki, Pharmaceutical Research **7** (4), 339 (1990).

[98] A. F. Yapel, Methods in Enzymology **112**, 3 (1985).

[99] A. Giletto, Technical Report, Lynntech Inc., College Station, TX, 1998.

[100] D. Katti and N. Krishnamurti, Journal of Microencapsulation **16** (2), 231 (1999).

[101] A. N. Kolmogorov, DOKLADY AKADEMII NAUK SSSR **66** (5), 825 (1949).

[102] J. O. Hinze, Aiche Journal **1** (3), 289 (1955).

[103] G. W. Zhou and S. M. Kresta, Chemical Engineering Science **53** (11), 2063 (1998).

[104] A. W. Pacek, C. C. Man, and A. W. Nienow, Chemical Engineering Science **53** (11), 2005 (1998).

[105] M. Nishikawa, Mori, F., and Fujieda, S., Journal of Chemical Engineering of Japan **20**, 82–88 (1987).

[106] J. Baldyga, J. R. Bourne, A. W. Pacek, A. Amanullah, and A. W. Nienow, Chemical Engineering Science **56** (11), 3377 (2001).

[107] A. W. Pacek, P. Ding, and A. W. Nienow, Chemical Engineering Science **56** (10), 3247 (2001).

[108] J. H. Waite and A. C. Riceficht, Biochemistry **26** (24), 7819 (1987).

[109] F. Groeneweg, F. Vandieren, and W. G. M. Agterof, Colloids and Surfaces a-Physicochemical and Engineering Aspects **91**, 207 (1994).

[110] W. J. Tjaberinga, A. Boon, and A. K. Chesters, Chemical Engineering Science **48** (2), 285 (1993).

[111] K. Shimizu, K. Minekawa, T. Hirose, and Y. Kawase, Chemical Engineering Journal **72** (2), 117 (1999).

[112] A. H. Lefebvre, *Atomization and Sprays* (Hemisphere Publishing Corporation, Washington D. C., 1989).

[113] S. R. White, N. R. Sottos, P. H. Geubelle, J. S. Moore, M. R. Kessler, S. R. Sriram, E. N. Brown, and S. Viswanathan, Nature **409** (6822), 794 (2001).

[114] U. Gasser, E. R. Weeks, A. Schofield, P. N. Pusey, and D. A. Weitz, Science **292**, 258 (2001).

[115] A. M. Alsayed, M. F. Islam, J. Zhang, P. J. Collings, and A. G. Yodh, Science **309**, 1207 (2005).

[116] W. K. Kegel and A. v. Blaaderen, Science **287**, 290 (2000).

[117] Q.-H. Wei, C. Bechinger, and P. Leiderer, Science **287**, 625 (2000).

[118] A. Ulman, Chem. Rev. **96**, 1553 (1996).

[119] M. A. Bevan and P. J. Scales, Langmuir **18** (5), 1474 (2002).

[120] M. A. Bevan, S. N. Petris, and D. Y. C. Chan, Langmuir **18** (21), 7845 (2002).

[121] G. Fernandes and M. A. Bevan, submitted (2005).

[122] K. Hwang, H.-J. Wu, and M. A. Bevan, Langmuir **20** (26), 11393 (2004).

[123] A. van Blaaderen and A. Vrij, Langmuir **8**, 2921 (1992).

[124] L. M. Rossi, L. Shi, F. H. Quina, and Z. Rosenzweig, Langmuir **21**, 4277 (2005).

[125] A. K. van Helden, J. W. Jansen, and A. Vrij, J. Colloid Interface Sci. **81** (2), 354 (1981).

[126] K. A. Dawson, Curr. Opin. Colloid In. **7**, 218 (2002).

[127] J. R. Savage, D. W. Blair, A. J. Levine, R. A. Guyer, and A. D. Dinsmore, Science **314** (5800), 795 (2006).

[128] A. D. Dinsmore, A. G. Yodh, and D. J. Pine, Physical Review E **52** (4), 4045 (1995).

[129] B. Cui, B. Lin, D. Frydel, and S. A. Rice, Phys. Rev. E **72**, 021402 (2005).

[130] M. Bevan, PhD Dissertation, Carnegie Mellon University, 1999.

[131] D. W. Marr and A. P. Gast, J. Chem. Phys. **99** (3), 2024 (1993).

[132] D. W. M. Marr and A. P. Gast, Phys. Rev. E **53** (4), 4058 (1995).

[133] K. H. Lin, J. C. Crocker, V. Prasad, A. Schofield, D. A. Weitz, T. C. Lubensky, and A. G. Yodh, Physical Review Letters **85** (8), 1770 (2000).

[134] S. Anekal, P. Bahukudumbi, and M. A. Bevan, Phys. Rev. E **73**, 020403 (2006).

[135] P. Bahukudumbi, W. N. Everett, G. Huff, Z. Ouenies, D. Lagoudas, A. Beskok, and M. A. Bevan, in preparation (2007).

VITA

Pradipkumar Bahukudumbi graduated with a Bachelor's degree in Mechanical Engineering degree from the University of Madras, India in May 2000. He was ranked first in a graduating class of 80 students. In August 2000, he joined the mechanical engineering department at Texas A&M University for his graduate studies and received his Master of Science degree in Mechanical Engineering in December 2002. His master's thesis was focused on developing phenomenological models for rarefied gas flows in thin film slider bearings. He enrolled in the doctoral program in mechanical engineering at Texas A&M University in January 2003 and graduated in May 2007. His current research interests are in the field of assembly and dynamics of interfacial colloidal fluids.

He can be reached at pradippb@gmail.com or by contacting Dr. Michael Bevan, Department of Chemical Engineering, Texas A&M University, College Station, TX 77843-3122.